Archim Wolfberger

Photoreactive Materials for Applications in Organic Electronics

PhD Thesis

Dissertation

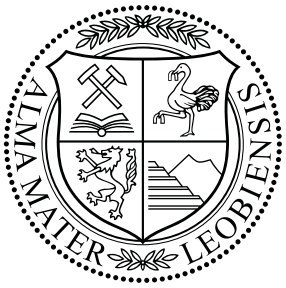

Montanuniversität Leoben,
Chair of Chemistry of Polymeric Materials

Leoben, September 2014

Supervisor:
Ass. Prof. Dipl.-Ing. Dr. techn. Thomas Griesser
Doctoral Comittee:
Univ.-Prof. Mag. rer. nat. Dr. techn. Wolfgang Kern
Ao. Univ.-Prof. Dipl.-Ing. Dr. techn. Ferdinand Hofer

KUNSTSTOFF TECHNIK LEOBEN
CHEMIE DER KUNSTSTOFFE

"The true delight is in the finding out rather than in the knowing."

– Isaac Asimov

I hereby declare in lieu of oath, that I wrote this thesis and performed the associated research myself, using only the support indicated in the acknowledgements and literature cited in this volume.

Leoben, September 2014 *Dipl.-Ing. Archim Wolfberger*

Acknowledgements

I want to express my gratitude to my family for supporting me during the entire time of my studies and I want to thank my girlfriend Gloria for her support in every situation, without which this work would not have been possible. I also want to thank all of my friends for a very enjoyable time in Leoben.

I would like to thank my supervisor Thomas Grießer for his support and suggestions during my work and Wolfgang Kern for providing the opportunity to be involved in this and other interesting projects at the Chair of Chemistry of Polymeric Materials.

Many thanks to all the employees of our Chair and the Christian Doppler Laboratory for Functional and Polymer Based Inkjet Inks for their support, especially to Paul Hofer for parts of the work on polynorbornenes, Herbert Weitensfelder for parts of the AFM measurements and Jakob Herka for parts of the work on cellulose. Furthermore, I want to thank Gisbert Riess for additional funding in the final period of this work.

I would also like to express my gratitude to my colleagues at Joanneum Research - MATERIALS in Weiz for the excellent cooperation during the past years. I want to thank Andreas Petritz, Alexander Fian, Barbara Stadlober, Volker Schmidt and all other employees who supported me during this work. I would also like to thank Stefan Spirk and Sascha Winter from Graz University of Technology and Rupert Kargl from the University of Maribor for the cooperation on the cellulose topic.

Furthermore, I would like to thank Irena Drevenšek Olenik for the opportunity to visit and conduct experiments at the Jožef Stefan Institute in Ljubljana, Bernhard Sartory from the Materials Center Leoben for the SEM measurements and Zaoli Zhang from the Erich Schmid Institute of Materials Science for the TEM measurements.

Financial support by the Austrian Science Fund (FWF) (Project TRP 181-N19), by the Christian Doppler research association and the Austrian Ministry of Economics, Family and Youth (BMWFJ) is gratefully acknowledged.

Abstract

The presented work focuses on the development of novel photoreactive materials for applications in organic electronics.

Photopatternable dielectrics are realized by utilizing crosslinking reactions of polynorbornene derivatives with bisazide compounds, as well as by side reactions of the photo-Fries rearrangement. Furthermore, a versatile approach that provides an easy patterning method for cellulose thin films by means of photolithography, is presented. The main concept of this approach is to exploit the acid-induced desilylation reaction of trimethylsilyl cellulose (TMSC) by the use of photoacid generators (PAGs). This method provides the possibility to realize either positive- or negative type structures, depending on the development conditions, with resolutions down to the sub-micrometre range. This biopolymer-based material can therefore be considered as a dual-tone photoresist. The potential application of these dielectric materials in organic electronics is demonstrated by assembling organic thin film transistors (OTFTs) with photopatterned gate dielectrics, exhibiting good performance compared to established materials and processes. These photopatternable dielectric materials enable the realization of electrical interconnects, as required for the fabrication of demanding organic electronic circuits.

For the realization of photopatternable electrodes, which are compatible with processes in organic electronics, the photo-induced crosslinking of stabilized gold nanoparticles with a bisazide compound is further explored. Photolithographic patterning of this material leads to nanoparticle patterns with resolutions in the single-digit micrometre range, allowing the fabrication of electrically conductive gold structures by a subsequent sintering step at temperatures below 250 °C. The suitability of these photopatternable electrodes is shown by assembling OTFTs, using such photopatterned gold nanoparticle films as source/drain electrodes.

Kurzfassung

Die vorliegende Arbeit beschäftigt sich mit der Entwicklung neuartiger photoreaktiver Materialien für Anwendungen im Bereich der organischen Elektronik.

Photostrukturierbare Dielektrika können sowohl durch eine Vernetzung von Polynorbornenderivaten mit Bisaziden, als auch durch Nebenreaktionen bei der Photo-Fries Umlagerung, realisiert werden. Weiters wird ein Verfahren zur Strukturierung von Cellulose-Dünnschichten anhand photolithographischer Methoden vorgestellt. Das Konzept dieser Strukturierungsmethode basiert auf einer säurekatalysierten Desilylierung von Trimethylsilylcellulose anhand von Photosäuregeneratoren (PAGs). Die hier beschriebene Methode erlaubt, je nach Entwicklungsmethode, die Herstellung von Positiv- oder Negativstrukturen mit einer Auflösung bis in den Submikrometerbereich. Dieses auf Biopolymeren basierte System kann daher als Zweitonphotolack (engl. dual-tone photoresist) betrachtet werden. Das Potential der untersuchten Materialien für Anwendungen in der organischen Elektronik wurde anhand von OTFTs mit photostrukturierten Dielektrika gezeigt. Diese photostrukturierbaren Materialien ermöglichen die einfache Herstellung von elektrischen Verbindungen, welche für komplexe organische Schaltkreise benötigt werden.

Für die Realisierung von photostrukturierbaren Elektroden, kompatibel mit Prozessen in der organischen Elektronik, wurde die lichtinduzierte Vernetzung von stabilisierten Gold-Nanopartikeln mit Bisaziden untersucht. Eine photolithographische Strukturierung dieses Materials führt zu vernetzten Gold-Nanopartikelfilmen mit Auflösungen im Bereich weniger Mikrometer, welche in einem darauffolgenden Sinterschritt unter 250 °C zu leitfähigen Strukturen umgewandelt werden können. Die Eignung dieses Materials für die organische Elektronik wird anhand von OTFTs mit photostrukturierten Source/Drain Elektroden gezeigt.

Contents

1 General Introduction

1.1 Organic Electronics

Since the development of molecularly doped polyacetylene, a conductive conjugated polymer, by Heeger, MacDiarmid and Shirakawa in 1977, a rapid growth of the field of organic semiconducting materials was encouraged.[1] The invention of the first organic light emitting diodes (OLEDs) with small molecules by Tang and Van Slyke in 1987, followed by the first conjugated polymer OLEDs by Burroughes et al. in 1990, enabled the development of large-area electronic devices with significantly decreased cost per area compared to conventional (inorganic) light emitting devices.[2,3] The main research on organic thin film transistors (OTFTs), one of the basic elements for any organic logic circuit, also emerged in the late 1980s, focusing on both polymers[4,5] and small molecules[6]. Despite the comparably low performance of these initial devices, much effort was devoted in research to improve their performance, considering the potential of organic electronics.

The main advantage of this technology is the possibility of solution processing, enabling a simplified large-area device fabrication with a reduced number of vacuum steps. This also facilitates up-scaling of the manufacturing process "from lab to fab". Processing can typically be performed at temperatures below 200 °C, thus also enabling the use of inexpensive polymer substrates for the realization of lightweight and flexible electronics.[7] The capability to deposit organic materials from solution further allows to pattern functional materials, using printing methods such as inkjet-, gravure- or screen printing, leading to the concept of printed electronics.[8] Moreover, when using organic materials, the comprehensive toolbox of organic chemistry is available for tailoring electrical, optical, rheological or chemical properties, leading to highly customizable functional materials.[9]

These favourable properties open the way for an economical fabrication of a multitude of electronic devices, including OLEDs, OTFTs, organic photovoltaic devices (OPV), sensors, batteries, microelectromechanical systems (MEMs) or radio-frequency identification (RFID) tags. Furthermore, novel highly innovative products

such as rollable displays, disposable diagnostic devices, printed flexible batteries, "lab-on-a-chip" devices or "smart textiles" can be realized, to name just a few.[10]

However, the main drawbacks of organic electronics, particularly when utilizing organic semiconductors, are a comparably low device performance and a high sensitivity to environmental influences such as oxygen, moisture or UV-radiation with organic compounds being generally susceptible to ageing. Nonetheless, the wide range of applications and possible uses for organic electronics are of substantial interest for research and industrial appliances and currently gain progressively increasing market attractiveness.[10–12]

1.1.1 Organic Thin Film Transistors (OTFTs)

The basic principle of the field effect transistor (FET) was first proposed in 1930 by Lilienfeld.[13] In these devices, the density of charge carriers in the channel between two electrodes is modulated by a bias applied to a third electrode. FETs can serve as switching- and amplifying components in electronic circuits and even though the field effect in organic semiconductors was first reported in 1970 by several authors[14,15], organic field effect transistors (OFETs) have only been identified as potential components in electronic devices in 1987.[5]

The charge carrier mobility μ, besides other parameters, is often cited to compare the performance of different OTFT materials and fabrication techniques. Organic FETs with a thin film transistor architecture were used extensively from the early 1990s when the mobility in devices with small molecule materials, particularly pentacene, exceeded $0.1\,\mathrm{cm^2/V\,s}$ and began to approach values obtained in hydrogenated amorphous silicon (a-Si:H), lying in the range of $0.5–1\,\mathrm{cm^2/V\,s}$. Since then, the mobility of these OTFTs has continued to improve, with the highest values now in excess of $10\,\mathrm{cm^2/V\,s}$.[16,17]

Different OTFT structures can be realized by arranging a dielectric layer, a semiconducting layer and the three respective electrodes in several specific configurations as shown in Figure 1.1, depending on the used materials and targeted processing methods. Each of the possible OTFT configurations possesses its advantages and drawbacks, influencing device properties as well as the possibilities for fabrication. However, due to the sensitivity of most organic semiconductors, a deposition of the semiconductor on top of the layer stack is advantageous and, therefore, the large majority of current OTFTs are built according to the bottom-gate architecture (see Figure 1.1a-b). The layer setup also influences the feasibility for different patterning

techniques of the electrodes (e. g. photolithography or shadow mask evaporation). The achievable resolution of these patterning techniques further determines the device performance.[11]

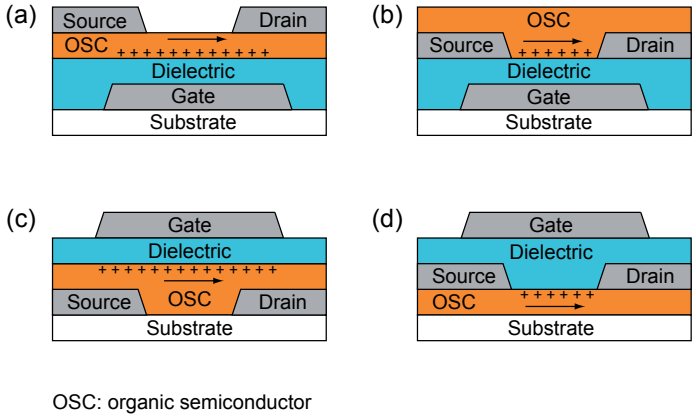

Figure 1.1: Possible configurations of thin film transistors: bottom-gate, staggered (a), bottom-gate, coplanar (b), top-gate, staggered (c) and top-gate, coplanar architecture (d)

1.1.2 Properties of Organic Semiconductors

Two main classes of organic semiconductors can be distinguished: 1) low molecular weight materials, which are often referred to as small molecules and 2) polymers. Both material classes exhibit a conjugated π-electron system being formed by the p_z-orbitals of sp^2-hybridized carbon atoms (see Figure 1.2), which is responsible for the ability of the material to transport charges.

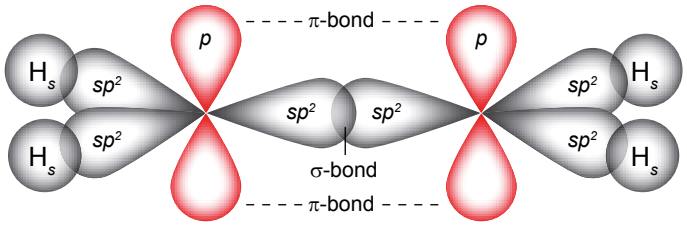

Figure 1.2: σ- and π-orbitals between sp^2-hybridized carbon atoms. Figure adapted from[18]

These π-bonds result from an overlap of two p_z-atomic orbitals, leading to bonding- and antibonding molecular orbitals, as shown in Figure 1.3. In this case, two electrons occupy the bonding π-orbital, lying at a lower energy level than the two

non-interacting p_z-atomic orbitals. In conjugated systems, the electrons in the π-orbitals are delocalized within the molecule or along the conjugated polymer backbone, enabling the flow of charge carriers in the material. In solids, these filled bonding π-orbitals form the highest occupied molecular orbital (HOMO) and the empty antibonding π^*-orbitals form the lowest unoccupied molecular orbital (LUMO). These energy levels can be thought of as corresponding to the valence- and conduction bands in conventional inorganic semiconductors and are used in the same way to represent the band offsets between the different components of a specific device structure.[17]

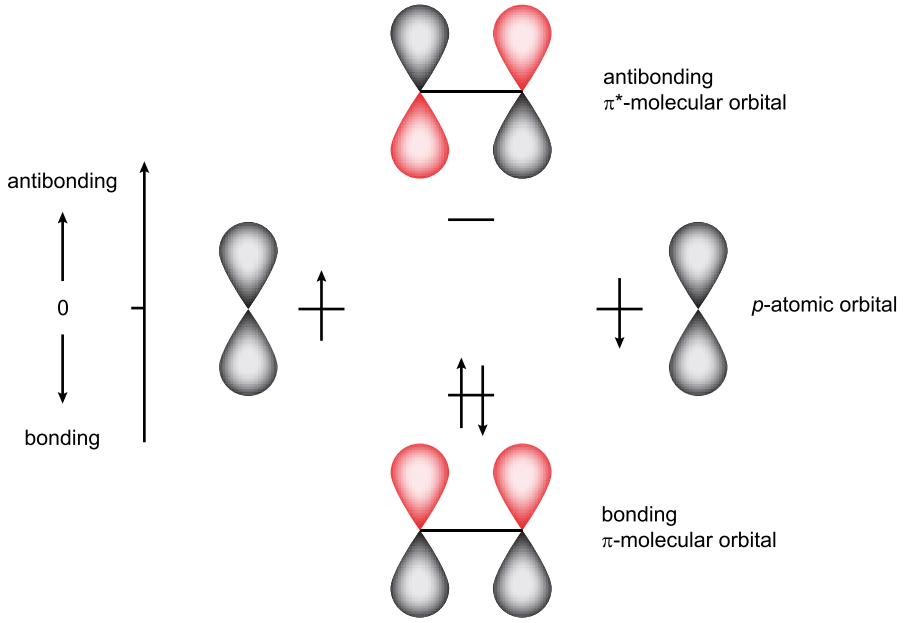

Figure 1.3: Occupation of the bonding π-orbital from electrons of the non-interacting p_z-orbitals. Figure adapted from[18]

Due to the fact that π-bonds are significantly weaker than σ-bonds, the lowest electronic excitation of conjugated molecules is the π-π^*-transition (HOMO-LUMO), as shown in Figure 1.4, with an energy gap typically lying between 1.5 and 3 eV. This energy gap leads to the absorption or emission of light in the visible spectral range and can be controlled by the degree of conjugation in a molecule, offering a wide range of possibilities to tune the optoelectronic properties of organic semiconducting materials.[19]

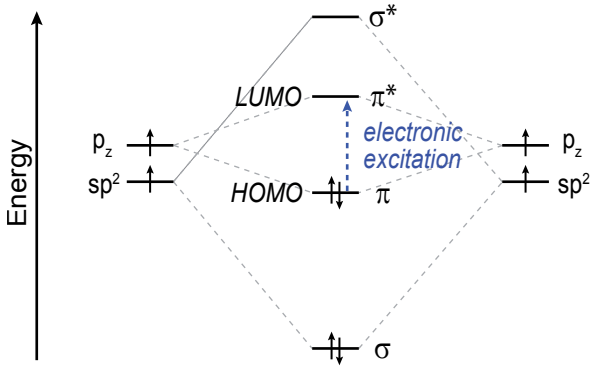

Figure 1.4: Energy levels of π-conjugated molecules at the example of ethene

Some representative and widely used organic semiconducting materials with a conjugated structure are shown in Figure 1.5. From the class of polymers, polyfluorene- and poly(3-alkylthiophene) derivatives are often used in OTFTs, with highly regioregular poly(3-hexylthiophene) reaching mobility values up to $0.1\,\mathrm{cm^2/V\,s}$. For the fabrication of p-type OTFTs based on small molecules, pentacene and oligothiophenes are the most important materials with mobilities up to $6\,\mathrm{cm^2/V\,s}$ and $1\,\mathrm{cm^2/V\,s}$, respectively. A further high electron-mobility material, often used in n-type OTFTs is buckminsterfullerene (C_{60}), exhibiting a charge carrier mobility up to $0.5\,\mathrm{cm^2/V\,s}$.[11]

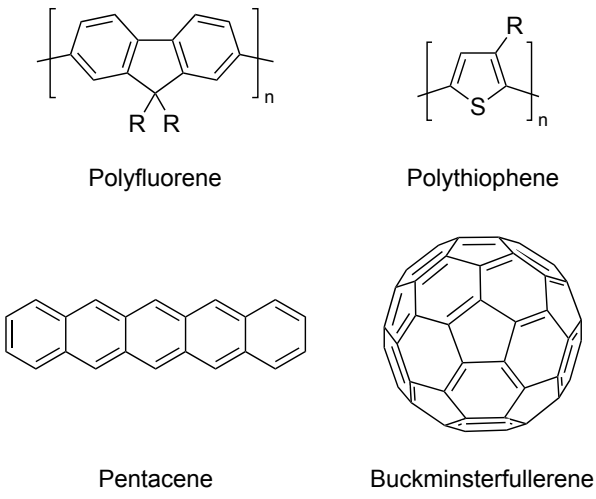

Figure 1.5: Chemical structure of selected organic semiconducting materials

1.1.3 OTFT Gate Dielectrics

Besides the organic semiconductor, the dielectric material is similarly important for realizing an appropriate electrical device performance in gate-insulated OTFTs.

General requirements for dielectric materials are a good interface between the dielectric and organic semiconductor with a smooth surface, low leakage currents, low pinhole densities and a high breakdown field of the dielectric, in excess of several MV/cm. Other desirable OTFT attributes include a low voltage operation and the possibility for solution processing.[17]

Over the past decade, a wide range of dielectric materials has been successfully employed as gate dielectrics in OTFTs. These materials can basically be classified into four groups, distinguished by their chemical composition or their assembly as a dielectric layer. A distinction between inorganic dielectrics, organic dielectrics, self-assembled monolayer (SAM) dielectrics, and multilayer or multi-component dielectrics can be made. Furthermore, a fifth group can be defined as multifunctional dielectrics, comprising all materials described above by extending the classification beyond their insulating properties.[11]

From the mentioned material classes, organic dielectrics are especially versatile with respect to tuning their physical and chemical surface properties, in order to improve the OTFT performance. In the bottom-gate configuration of OTFTs, the insulator is capable of affecting the morphology of the semiconductor layer, with its surface energy strongly influencing the nucleation and growth mechanism of vapour deposited organic semiconductor films. According to standard nucleation and growth models, an increasing surface energy leads to an increase of the nucleation rate and therefore to a decrease of the grain size of the organic semiconductor.[20] The effect of the grain size of the organic semiconductor on the performance of OTFTs is currently still a matter of research and not fully understood. However, based on conventional theories on charge transport in polycrystalline semiconductors it can be expected that the mobility increases with bigger grain size.[21] This can be explained by a decrease of the number of grain boundaries, leading to improved charge transport. Besides morphological effects, the type of insulator may also have chemical and electrical consequences with the use of either high dielectric constant (high-κ) or low dielectric constant (low-κ) gate insulators. In general, low-κ dielectrics influence the OTFT performance by reducing parasitic capacitance, enabling faster switching speeds and a lower power consumption. The interest in high-κ organic dielectrics arises from the gate voltage dependence of the mobility. High capacitance leads to high charge-carrier concentrations at low gate voltages, hence mobility is expected to be higher. The respective advantages of low-κ and high-κ dielectrics thus seem contrary and are still a matter of research.[11,17]

1.1.4 OTFT Electrodes

For the fabrication of organic electronic devices, inexpensive, non-oxidizing electrodes present a challenge. Source/drain and gate electrodes based on noble metal thin films, including Au, Pd, Pt are widely used in OTFTs and also other metals such as Al, Cr, Cu, and Ni have been investigated comprehensively.[22] Many metal layers also enable a surface modification e. g. with self-assembled monolayers, to tune the layer- and device properties.[23] For OTFT fabrication, evaporation or sputtering techniques are often used for the deposition of the gate metal electrodes, with additional lithography steps to define them. For top-gate structures with a polymer gate dielectric, this may be less practical due to an incompatibility of commonly used dielectrics with the lithographic process. Therefore, solution processing is a viable option for top-gate OTFTs, also allowing a fabrication without the need for time-consuming and cost-intensive vacuum steps.[10,17]

Widely used solution-derived conductive layers include conducting polymers, such as doped polyaniline and poly(3,4-ethylenedioxythiophene) doped with polystyrene sulfonate (PEDOT:PSS), as well as dispersions of inorganic metallic nanoparticles. The chemical structure of these representative polymeric materials is depicted in Figure 1.6.

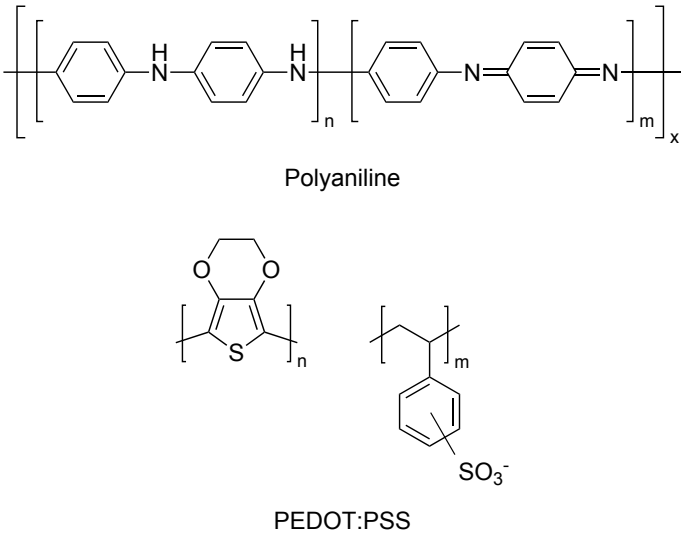

Figure 1.6: Chemical structure of selected conductive polymers

In some cases, however, conducting polymers contain dopants to increase their conductivity, which may migrate during device operation and can affect the operational stability of devices. Furthermore, particle-based systems often require low

molecular weight stabilizers to maintain solubility, which either lead to an increased resistance or must be removed to sinter these particle-based layers. Such polymeric and particle-based systems present an additional challenge when fabricating devices on polymeric substrates, in which the solvent must be removed or where particles must be sintered at temperatures exceeding 150 °C. Therefore, polymer substrates with a high thermal and chemical stability are required.[22]

Nonetheless, these solution-based materials are well suited for large area fabrication techniques including roll-to-roll processing. Additionally, the high transparency of some organic conductors (e. g. PEDOT:PSS) renders these materials an appropriate alternative for electrodes based on indium tin oxide (ITO), in some applications.[10,17]

1.2 Photochemistry

Photochemistry plays an important role in modern semiconductor electronics and is concerned with reactions which are initiated by electronically excited molecules due to an absorption of light, preferably in the visible and near ultraviolet region of the electromagnetic spectrum. One of the fundamental principles relating to photochemistry is the Grotthuss-Draper law, which states that only light which is absorbed by a chemical entity can cause photochemical change. Another important principle in this regard is the Stark-Einstein law, stating that the primary act of light absorption by a molecule is a one-quantum process, where for each photon absorbed only one molecule is excited. However, when very intense light sources such as lasers are used for irradiation, concurrent or sequential absorption of two or more photons may also occur.[24]

In order to trigger photochemical reactions, molecules must exhibit an electronic configuration where the absorption of one photon promotes an electron from the HOMO to the LUMO. These reactions are only possible, if the incident light contains photons having exactly the energy corresponding to a specific HOMO-LUMO transition. The absorbed energy E hereby equates to the product of the Planck constant h and the frequency of the absorbed photon ν, which is a function of the speed of light in vacuum c and its wavelength λ, as shown in Equation 1.1.

$$\Delta E = h * \nu = h * \frac{c}{\lambda} \tag{1.1}$$

With an excitation of a molecule from its singlet ground state (S_0) to an excited singlet state (S_n*), one electron is promoted into the next higher orbital under spin

conservation (see Figure 1.7). From this excited state, the molecule can revert back to its ground state in different ways through either radiative- or non-radiative primary and secondary processes. A schematic representation of the absorption process of a photon and the possible emission processes of a molecule from its excited state are illustrated in a Jablonski diagram in Figure 1.8.

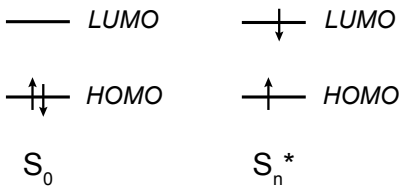

Figure 1.7: Schematic representation of a singlet ground S_0 state and an excited singlet state S_n*

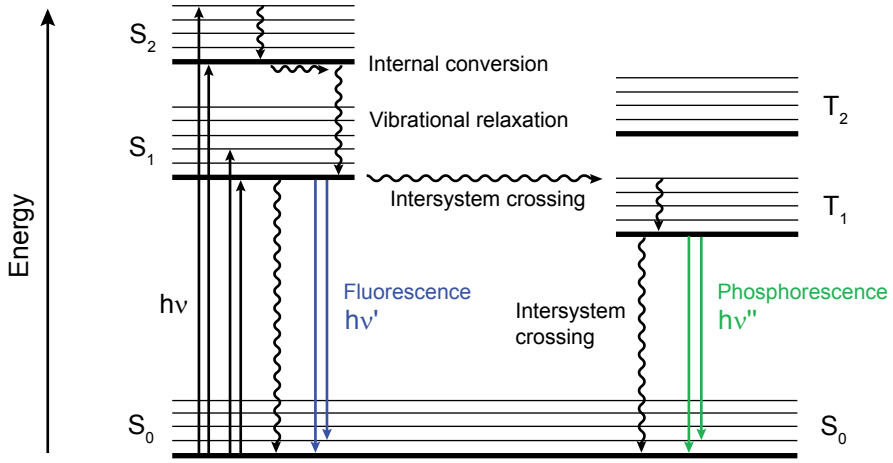

Figure 1.8: Jablonski diagram of the electronic states of a molecule and its transitions. Figure adapted from[25]

A molecule in an excited singlet state S_n* rapidly decays to the lowest excited singlet state S_1* by non-radiative processes (internal conversion and vibrational relaxation), allowing further chemical reactions. An electronically excited molecule in the S_1* state can then revert back to its ground state S_0 by vibrational relaxation or by emission of a photon (fluorescence). However, the energy gap between the excited state and the ground state can be smaller than that of the original excitation. Therefore, a shift of the wavelength of the emitted light to higher wavelengths is observed. Another possibility for a molecule in an excited singlet state to revert back to the ground state is by intersystem crossing (ISC), which is thermodynamically favoured, although in principle forbidden by quantum mechanics. Hereby, the

electron in the HOMO changes its spin, leading to the energetically more feasible excited triplet state T_1*. A molecule in the T_1* state with a lifetime in the order of $t \geq 10^{-4}$ s can return back to the ground state either by a release of heat, by emission of a photon (phosphorescence) or by undergoing chemical reactions. In the case of phosphorescence, the energy gap between the excited triplet state T_1* and the ground state S_0 is smaller than the gap between S_1 and S_0. Therefore, light emitted by phosphorescence has a higher wavelength than both the initial incident light and the fluorescence emission.[24–26]

1.2.1 Photo-Induced Crosslinking of Polymers

Intermolecular crosslinking, caused by the formation of covalent bonds between polymer chains, results in an increase of the average molar mass and eventually leads to the formation of a three-dimensional insoluble network. Crosslinking of macromolecules can be achieved in various ways, including reactions of electronically excited side groups on the polymer chains or reactions of photo-generated reactive species in polymeric systems. Typical examples for the former reaction type are [2+2] cycloadditions that occur at C=C bonds of unsaturated polymers e. g. in the case of poly(vinyl cinnamate). An important example for the latter type are reactions of nitrenes generated in polymeric systems, containing azide groups.[27]

Crosslinking reactions with photo-generated species have found widespread application in photolithography and resist technology, with organic azides being a suitable and widely studied functional group.[28] These azide groups can either be chemically attached to polymer chains or, alternatively, low molecular mass bisazide compounds containing two azide moieties can be added to a polymer to achieve photo-induced crosslinking of a variety of linear polymers. Upon absorption of a photon, a decomposition of the azide group takes place, leading to an electrically neutral and very reactive nitrene intermediate. This intermediate is in an electronically excited singlet state and can decay to the ground state, the triplet nitrene state (see Figure 1.9).

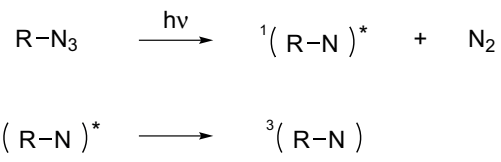

Figure 1.9: Photo-induced decomposition of azide groups, leading to singlet- and triplet nitrene groups

Both singlet and triplet nitrene are highly reactive species and can be used for crosslinking of polymers. Singlet nitrene can insert into C-H bonds of a polymer and, in the case of unsaturated polymers, can also add to C=C bonds and form aziridine groups, both in single step processes (see Figure 1.10).

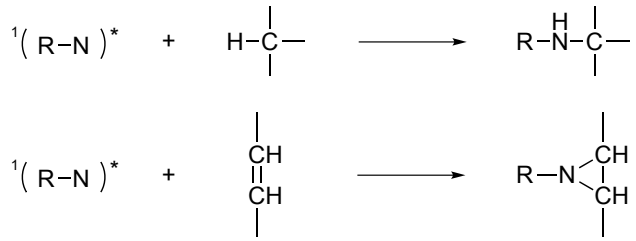

Figure 1.10: Possible reactions of singlet nitrene with saturated and unsaturated polymers

Triplet nitrene can abstract hydrogen atoms, thus forming an amino radical and a carbon (macro)radical as shown in Figure 1.11a. These two radicals can either couple or the amino radical can form a primary amine by hydrogen abstraction from a different molecule (see Figure 1.11b and c). Moreover, crosslinking can either occur by coupling reactions of macro-radicals (see Figure 1.11d), or after a reaction of both azide groups in the case of bisazides as shown in Figure 1.11e. The rearrangement of aryl nitrenes by the photolysis of aryl azides can further lead to the formation of azepine derivatives as side-products.[27,29]

Other important reactions for a photo-induced crosslinking are free radical mechanisms of benzophenone or acetophenone derivatives, which either directly abstract hydrogen from a polymer chain, or decompose into free radicals capable of abstracting hydrogen as shown in Figure 1.12, leading to crosslinking by a recombination of macro-radicals. In this regard, also organic peroxides are widely used as efficient thermal and photo-reactive crosslinking agents.[27]

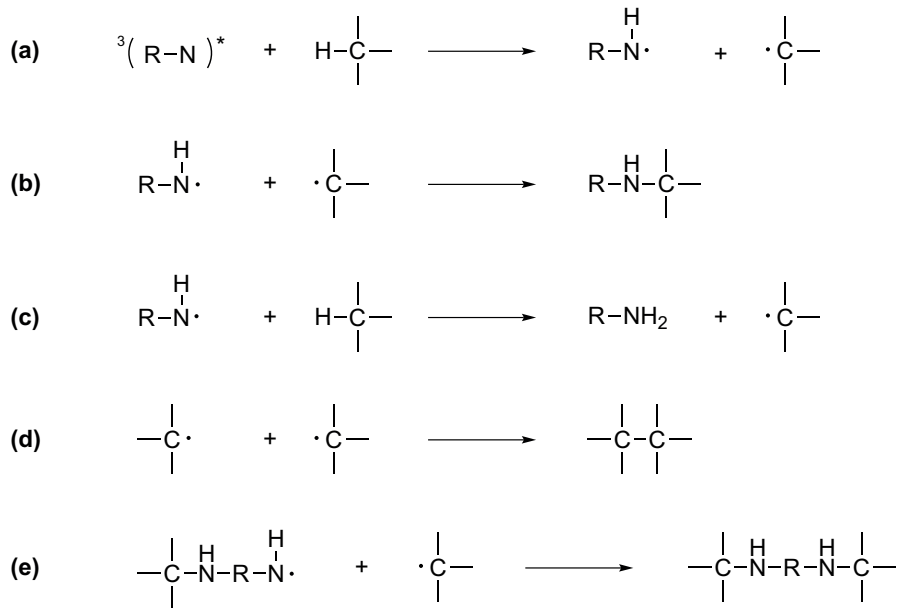

Figure 1.11: Possible reactions of triplet nitrene

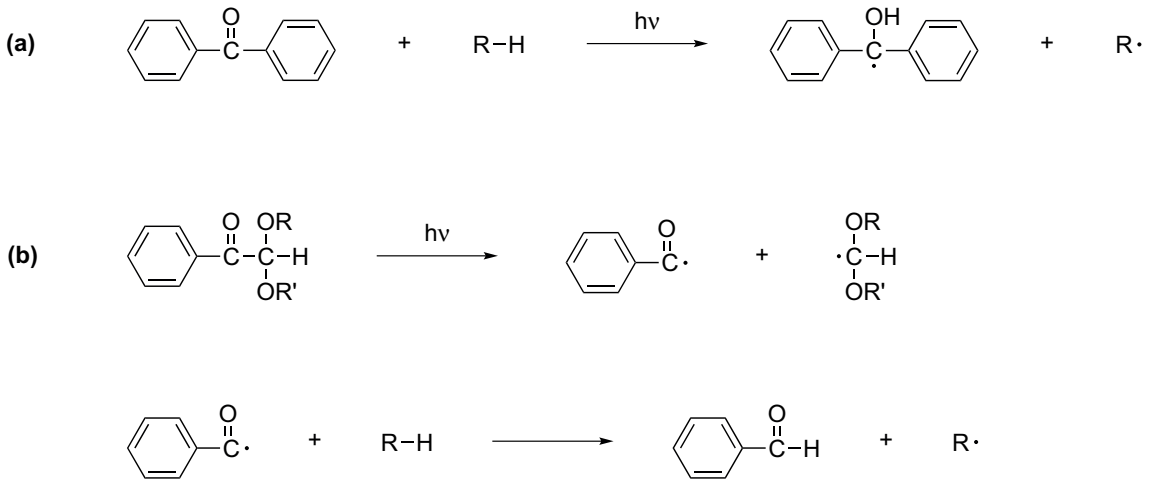

Figure 1.12: Generation of (macro)radicals from electronically excited benzophenone (a) and acetophenone derivatives (b)

1.2.2 Photo-Fries Rearrangement

The Fries reaction, discovered by Fries and Finck in 1908, describes the rearrangement of phenolic esters to the corresponding hydroxy aryl ketones under catalysis of a Lewis acid.[30] The light-induced Fries reaction, which is referred to as photo-Fries reaction, was first described by Anderson and Reese in 1960, showing that aryl esters rearrange to hydroxyketones under UV-illumination.[31] The widely accepted radical mechanism of the photo-Fries rearrangement was postulated by Kobsa, Finnegan and Mattice and is shown in Figure 1.13.[32,33]

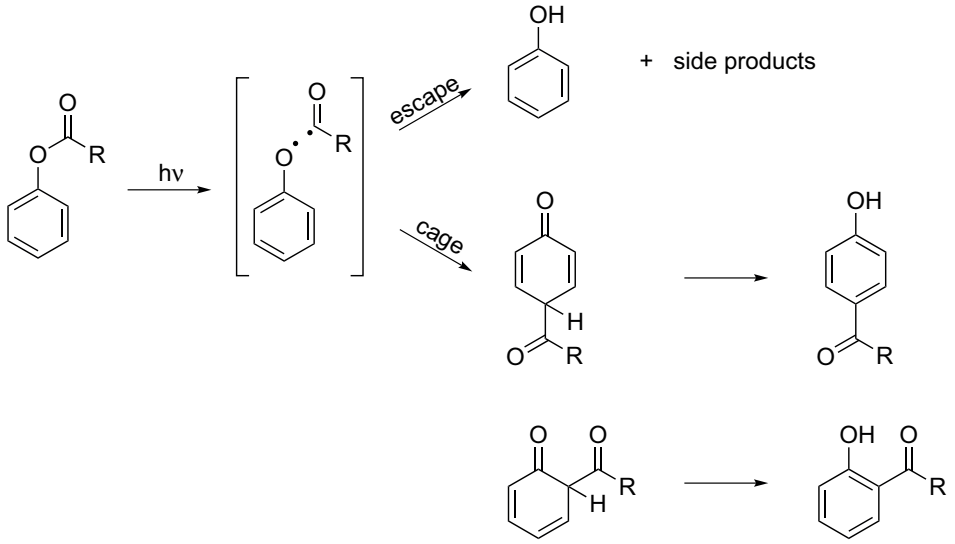

Figure 1.13: Photo-Fries reaction of aromatic esters

In this reaction, the absorption of photons leads to the electronic excitation of aromatic esters to their excited singlet state S_1*. A homolytic cleavage of the C-O bond then leads to the corresponding acyl- and phenoxy radicals. These radicals can either react in the solvent cage and form the original compound or recombine to ortho- and para-cyclohexadienone derivatives. Tautomerism results in the corresponding ortho- and para-hydroxyketones. When phenoxy radicals escape from the solvent cage, phenol is generated under H-abstraction, but also other side products such as carboxylic acids and hydrocarbons, are generated.[32,34] In addition to the photo-Fries rearrangement of phenolic esters, this reaction is also observed in other aromatic compounds, such as aromatic amides or urethanes. Polymers, containing these photoreactive side groups can also be used as photoresists, by exploiting either changes in polarity under UV-illumination[35], or crosslinking due to coupling reactions of the photo-generated radicals[36,37]. Both approaches allow

a selective removal of the exposed or non-exposed areas by using an appropriate solvent.[38,39]

1.3 Photolithographic Techniques

The principle of photolithography is based on the interaction of electromagnetic or particle radiation with thin layers of a radiation-sensitive material, which is usually referred to as photoresist. In general, the ideal photoresist replicates the exact shape of the designed or intended pattern in the plane of the substrate, with vertical walls through the thickness of the resist. Thus, the final resist pattern should be binary with parts of the substrate completely covered with resist and parts, which are completely uncovered. This binary resist behaviour is needed for pattern transfer, since the parts of the substrate covered with resist will be protected from etching or other pattern transfer mechanisms. Photoresists are categorized as positive or negative, whereby the exposure to light either causes the exposed patterns to be removed or to remain after a development step.[27,40] The general sequence of a subtractive patterning process is depicted in Figure 1.14 and involves the deposition of a uniform film of a resist material on a substrate, lithography to create a positive- or negative image of the desired pattern, as well as etching and stripping processes to transfer the pattern onto the substrate.

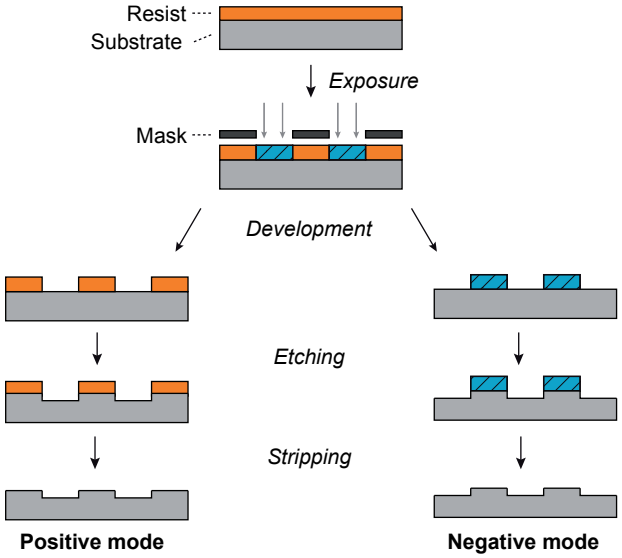

Figure 1.14: Schematic representation of the lithographic process

The basic methods of exposing a photoresist through a photo-mask (e. g. on a mask-aligner) are contact- and proximity lithography, offering reasonably high resolutions down to approximately the wavelength of the radiation. However, practical problems, such as mask damage and a significantly increased resolution limit in proximity lithography due to diffraction effects, led to the development of a variety of alternative exposure methods.[40] For the last two decades, the most common exposure method in the semiconductor industry has been projection lithography, where an image of the mask is projected onto the wafer with a demagnification ratio up to 4×. Regarding a periodic structure consisting of lines and spaces, the minimum achievable feature size or critical dimension (CD) of this technique, can be estimated with the aid of Equation 1.2.

$$CD = \frac{k_1 \lambda}{NA} \tag{1.2}$$

In this equation, λ is the wavelength of the exposure light and k_1 is a system parameter, depending on various factors such as resist response, pattern geometry, etc. The numerical aperture NA is defined by Equation 1.3 as a function of the refractive index n and the acceptance angle of the lens θ.[27,40]

$$NA = n \sin \theta \tag{1.3}$$

1.3.1 Two-Photon Absorption (TPA) Lithography

The existence of two-photon absorption (TPA) was predicted theoretically in 1931 by Göppert-Mayer and experimentally demonstrated in 1961 by Kaiser and Garrett.[41,42] TPA describes the excitation of a molecule to an energy level $h\nu_1 = 2h\nu_2$ by the simultaneous absorption of two photons via a virtual intermediate state with a lifetime of several femtoseconds. This process is only possible when both photons are spatially and temporary coincident and occurs with a probability proportional to the square of the light intensity. A schematic representation of the TPA process is illustrated in Figure 1.15.

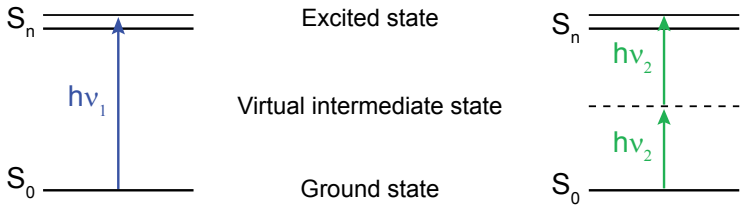

Figure 1.15: Schematic representation of the two-photon absorption process

Two-photon absorption can be induced when focussing a pulsed femtosecond (fs) laser using an objective lens with a high numerical aperture and allows the initiation of photoreactions at a laser power of a few milliwatts. Due to the fact that the TPA rate is proportional to the square of the laser intensity, two-photon abortion only occurs in a confined area near the focal point, where the laser intensity exceeds a certain threshold value (see Figure 1.16a). This allows for a selective initiation of photochemical reactions inside a photoresist layer, which is transparent for the laser wavelength, typically lying in the range of $\lambda = 800\,\text{nm}$. When scanning the focus spot of the laser inside the photoresist material, three-dimensional patterns with sub-micrometre resolution can therefore be fabricated as schematically illustrated in Figure 1.16b.[43]

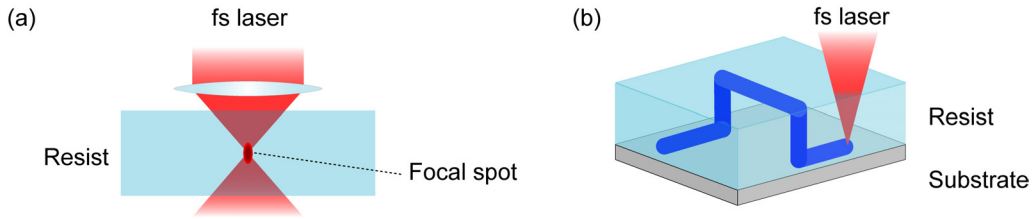

Figure 1.16: Illustration of the TPA excitation inside a resist layer (a) and 3D microfabrication by means of TPA lithography (b)

1.3.2 Interferometric Lithography

The interferometric exposure of photoresists with two or more coherent light beams provides a facile technique for a large-area fabrication of periodic patterns with resolutions down to the nanometre-scale.[44] Typically, a coherent laser source is split into two beams, which are incident on a thin photoresist layer at an angle of $+\theta$ and $-\theta$. For two-beam interference, the pitch of the interference pattern Λ is defined as shown in Equation 1.4, with a minimum achievable pitch of $\lambda/2$.

$$\Lambda = \frac{\lambda}{2\sin\theta} \tag{1.4}$$

While any suitable laser source can be used for interferometry, the most widely used lasers are argon-ion lasers and Nd:YAG lasers, operated at wavelengths that closely match the required wavelengths of the used photoresist. Typical configurations of interference lithography are either a split-beam setup, where the split coherent beam is overlapped, or a Llyod mirror setup, in which the top half of the beam is

reflected onto the sample by a mirror. Both interferometric set-ups are illustrated in Figure 1.17.[44,45]

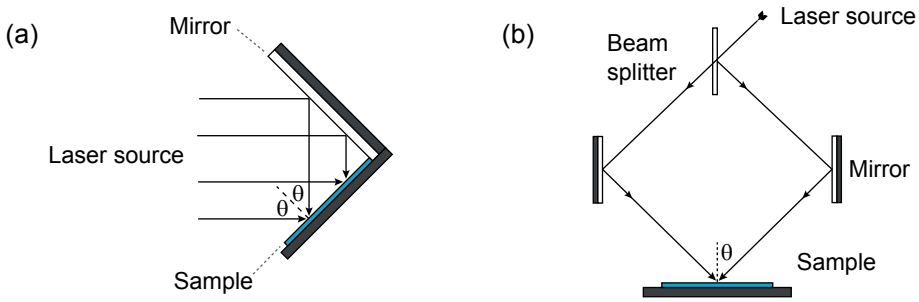

Figure 1.17: Interferometric setup consisting of a Lloyd mirror (a) and split-beam setup (b)

2 Photo-Induced Crosslinking of Polynorbornenes

Parts of the work in this chapter have been published previously in *Organic Electronics*.[46] AFM measurements, device fabrication and electrical characterization were performed at the Institute for Surface Technologies and Photonics at the Joanneum Research Forschungsgesellschaft mbH in cooperation with Andreas Petritz.

2.1 Introduction

To enable the fabrication of cheap and adequately performing organic circuits and devices, some important prerequisites have to be fulfilled. One of the major motivations of organic electronics is the cost-efficient manufacture of devices on flexible substrates including polymers, textiles or paper with the used materials ideally being solution-processable and manufacturing techniques compatible with these substrates. With regard to gate dielectrics, which are critical components for high-quality organic thin film transistors (OTFTs), it is important to implement suitable insulator materials, which meet the requirements for the fabrication of efficient devices. A significant reduction of the OTFT operation voltage is of particular importance in order to lower the power consumption so that the organic electronic circuits, depending on the intended application, can also be powered e. g. by household batteries. The charge separation and, accordingly, the charge carrier density in the source-drain channel of an OTFT are induced by the vertical electric field, which is established between the gate-electrode and the semiconducting layer and drops over the gate dielectric. High charge carrier densities at low gate voltages can only be achieved for high capacitive (high-κ) dielectrics with low leakage currents.[47]

To achieve such high-κ gate dielectrics, different approaches have been reported previously. One of these approaches is the use of ultra-thin close packed organic layers of a thickness of only a few nanometres, which were achieved by self-assembled monolayers (SAMs)[48] or polyelectrolytes[49]. Other approaches utilize inorganic high-κ dielectrics fabricated by atomic layer deposition[50], as well as oxide/polymer bilayers and nano-composites[51].

The use of intrinsically photopatternable gate dielectrics is especially desired to establish electrical interconnections in electronic circuits, which simplifies the design of circuits. Since none of the aforementioned approaches allows a photopatterning of the gate dielectric layer, photoresists (e. g. SU-8) were also considered as an alternative.[52] However, polymeric dielectric materials, which contain photo-polymerizable units such as epoxide groups, require photoinitiators for a UV-induced curing. These photosensitive molecules lead to the formation of either reactive radicals or acidic groups, initiating the polymerization or crosslinking upon UV-irradiation. In particular, residual ionic photoinitiators such as Crivello salts and their cleavage products present in the gate dielectric layer may also cause hysteresis effects. It is well known, that mobile ionic impurities can be responsible for the hysteresis in OTFTs and also decrease the long term stability of such devices.[53] Very often also the immediate deterioration of the OTFT characteristics under UV-illumination was observed in polymer dielectrics, containing photoinitiators.[54] Other UV-patternable dielectrics involve complex multi-step crosslinking and curing processes of polymer blends to achieve thin and electrically dense gate dielectrics.[55]

Therefore, single-step crosslinking mechanisms of different polynorbornene derivatives are investigated in order to achieve thin and electrically dense, photopatternable dielectrics for the application in low voltage pentacene-based OTFTs. Furthermore, the direct photopatterning capability of polynorbornenes, containing suitable photoreactive functional side groups, is explored. This allows for a direct photopatterning of the dielectrics without the need for additional photoinitiators or crosslinking components.[46]

2.2 Results and Discussion

2.2.1 Synthesis

The synthesis of the investigated polynorbornene derivatives was performed by means of ring-opening metathesis polymerization (ROMP), utilizing Grubbs-type catalysts of the first and of the third generation, as shown in Figure 2.1. The third generation Grubbs-type catalyst, also known as fast-initiating catalyst, was prepared by adding pyridine to a solution of the commercially available Grubbs catalyst of the second generation in THF under stirring. [56]

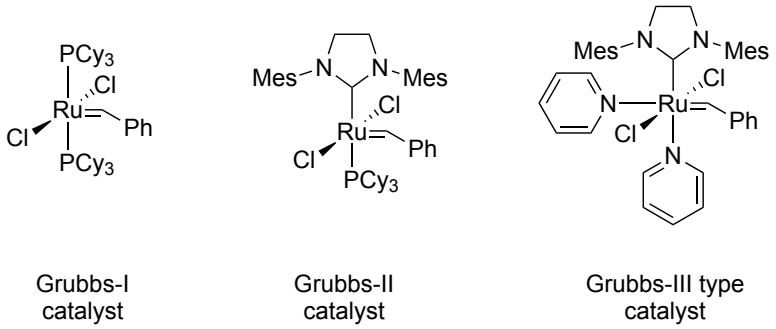

Grubbs-I catalyst | Grubbs-II catalyst | Grubbs-III type catalyst

Figure 2.1: Chemical structure of the used catalysts

The polymerization of (±)*endo,exo*-bicyclo[2.2.1]hept-5-ene-2,3-dicarboxylic acid dimethyl ester (Poly-NDME), (±)*endo,exo*-bicyclo[2.2.1]hept-5-ene-2,3-dicarboxylic acid diphenyl ester (Poly-NDPE) and bicyclo[2.2.1]hept-2-ene (Poly-NB) was done with a molar ratio of monomer to catalyst of 1:500. The polymerization reaction, which is depicted in Figure 2.2, was performed at room temperature in a glove box, in order to exclude ambient oxygen and water. The reaction was stopped with ethyl vinyl ether after a complete conversion. After precipitation in methanol, the products were dried *in vacuo*, providing yields in the range of 81 to 94%. GPC measurements revealed well defined molecular distributions with uniform dispersity Đ, with values in the range of 1.07–1.17. The molar mass dispersity of polymers is defined as the ratio of mass average- and number average molar mass ($Đ_M = M_w/M_n$) with $Đ_M = 1$ representing highly defined polymer chains, which are desired for applications involving crosslinking.

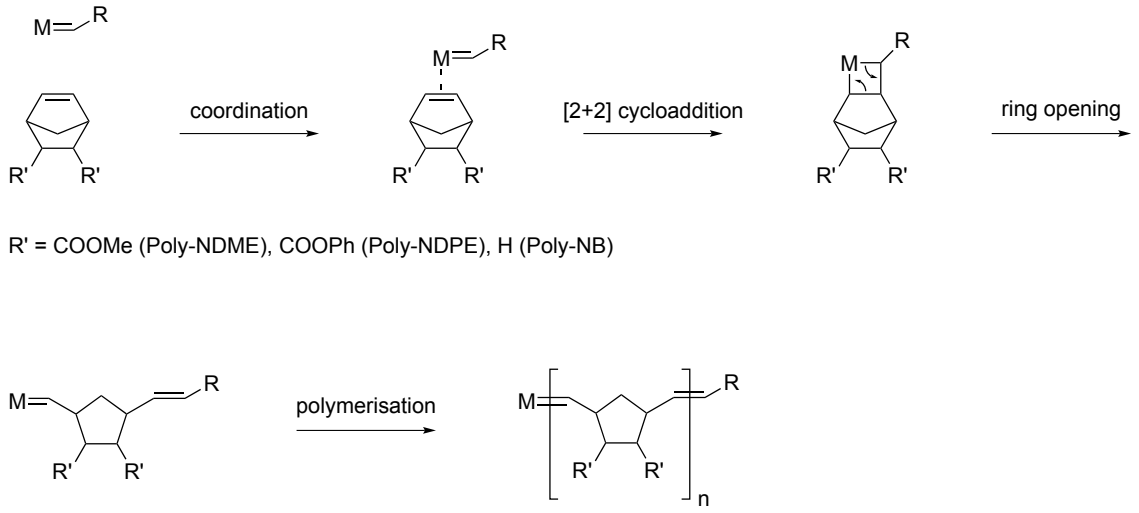

Figure 2.2: Ring-opening metathesis polymerization of norbornene derivatives

2.2.2 Crosslinking of Polynorbornenes

In order to achieve thin, photopatternable polymer films for applications as a dielectric layer, the UV-induced crosslinking of Poly-NB, Poly-NDME and Poly-NDPE with a bisazide compound was investigated. Crosslinking of macromolecules generally leads to changes in solubility and is therefore widely employed for applications including photoresists and photopatternable dielectric layers.[28]

Bisazide Crosslinking

Photo-induced crosslinking of Poly-NDME was already achieved previously by utilizing the thiol-ene reaction of multifunctional thiols with polyenes, for the fabrication of well defined 2D- and 3D microstructures.[57,58] This method has proven to be a suitable tool for crosslinking of unsaturated polymers. To demonstrate, that also other chemical reactions can be utilized for a UV-induced photopatternig of polynorbornenes, 2,6-bis(4-azidobenzylidene)-4-methylcyclohexanone (BAC-M) was used as a versatile, comercially available crosslinking component. The chemical structure, as well as its absorbance spectrum of this bisazide in the UV- and visible spectrum of light is shown in Figure 2.3.

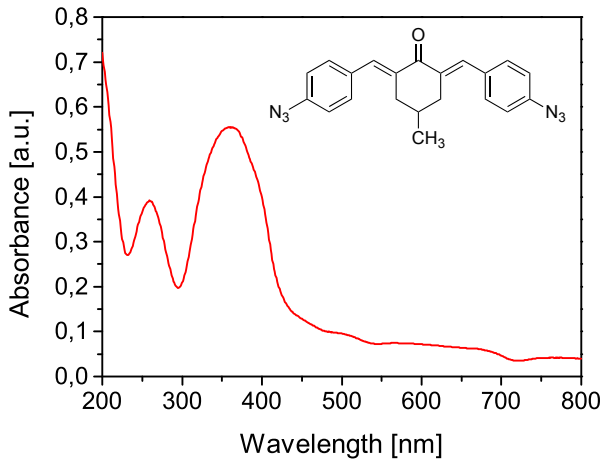

Figure 2.3: Chemical structure and UV/Vis spectrum of 2,6-bis(4-azidobenzylidene)-4-methylcyclohexanone (BAC-M)

Irradiation of BAC-M with UV-light with a wavelength of $\lambda = 365\,\text{nm}$ leads to the generation of nitrene groups (see Figure 2.4), which can interact with the polymer chains in various ways. These photo-generated radicals can react with unsaturated polymers by an addition to C=C double bonds with a generation of aziridine moieties or with saturated polymer chains by either inserting into C–H bonds or, alternatively, by abstracting hydrogen atoms from CH_2 groups and leaving free radicals, which terminate by coupling reactions.[28]

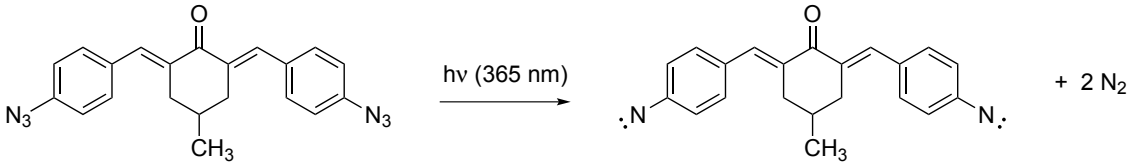

Figure 2.4: Generation of nitrene radicals under UV-illumination of BAC-M

The behaviour of BAC-M in thin Poly-NDME films under UV-illumination was investigated by means of FTIR spectroscopy. Poly-NDME with a number averaged molecular weight (M_n) of 58590 g/mol and a dispersity of $Đ = 1.17$ was used and 10 wt% of BAC-M were added to solutions of Poly-NDME in $CHCl_2$ prior to spin coating ($c = 20\,\text{mg/ml}$, $v = 1000\,\text{rpm}$, $a = 1000\,\text{rpm/s}$). To investigate the progress of the photoreaction, such films were prepared on KBr plates and FTIR spectra were recorded during the stepwise illumination with polychromatic UV-light. The resulting spectra before and after UV-illumination are plotted in Figure 2.5. The FTIR spectrum after illumination shows a strong decrease of the characteristic signal

at 2116 cm^{-1}, which can be assigned to the antisymmetric stretching vibration of the azido group. Furthermore, after UV-illumination a small emerging signal at 3380 cm^{-1} is observed, which may be attributed to the N–H stretching vibration caused by the formation of aziridine groups or by primary amino groups. However, the origin of this signal and a possible generation of aziridine moieties was not further investigated in this work.

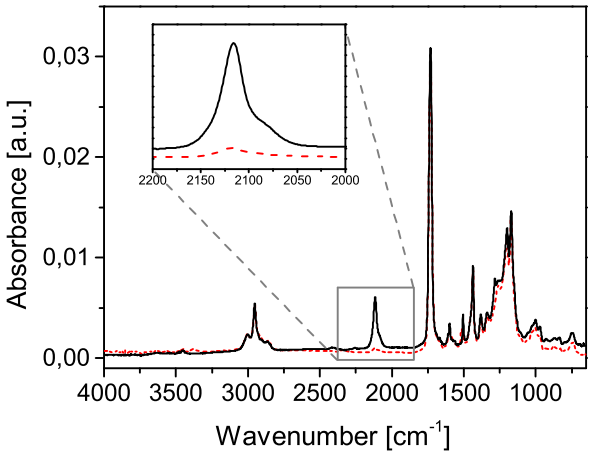

Figure 2.5: FTIR spectrum of a Poly-NDME film, containing 10 wt% BAC-M before (black line) and after (red dashed line) UV-illumination ($E = 16.3\,mJ/cm^2$)

In Figure 2.6 the remaining peak height of the signal of the azido group at 2116 cm^{-1} is plotted as a function of the illumination dose, showing an exponential decrease of the signal with no significant further changes after illumination with a dose of 16.3 mJ/cm^2.

A sol-gel analysis was furthermore employed to determine the crosslinking behaviour of Poly-NDME films, by comparing the height of the signal for C=O stretching vibrations of the ester group at 1731 cm^{-1}. For these experiments 1 to 15 wt% of BAC-M were added prior to spin coating onto CaF_2 plates. These layers were illuminated with increasing irradiation doses and the insoluble fraction (gel fraction) of the films was determined according to Equation 2.1, whereby h_{peak,s_1} represents the height of the ester peak at 1731 cm^{-1} before development and h_{peak,s_0} represents the peak height after development in chloroform for 10 minutes.[59]

$$\text{Gel fraction} = \frac{h_{peak,s_1}}{h_{peak,s_0}} \cdot 100 \tag{2.1}$$

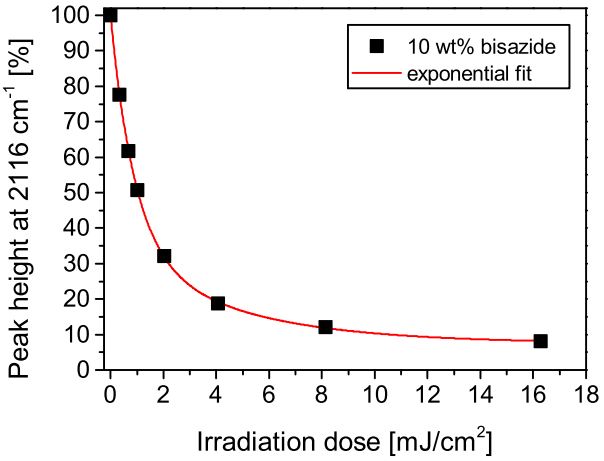

Figure 2.6: Decrease of the N_3 stretching vibration at 2116 cm^{-1} during UV-illumination of a Poly-NDME film, containing 10 wt% BAC-M

Figure 2.7 shows the insoluble fraction of these films as a function of the irradiation dose, representing the photoresist behaviour of these layers. It can be seen, that an increasing BAC-M content generally leads to an increase of the achievable gel fraction, reaching values up to 99%. Furthermore, an earlier onset of the insoluble fraction is observed with increasing bisazide content. Poly-NDME films, containing 1 wt% of BAC-M did not exhibit crosslinking and were removed completely during development. When adding 3 wt% of BAC-M, a gel fraction of 35% at 4.1 mJ/cm^2 is observed, decreasing to 20% after an illumination with 8.1 mJ/cm^2.

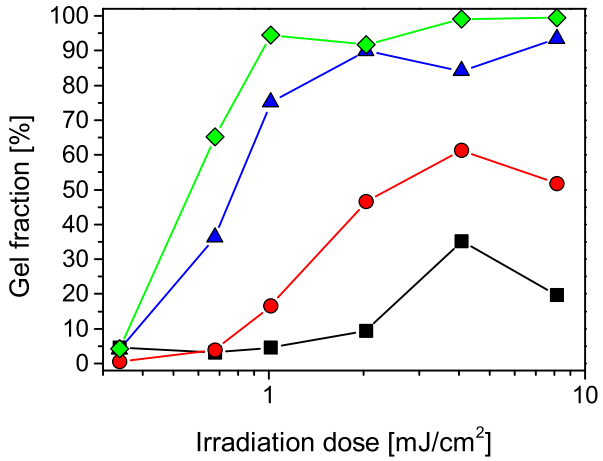

Figure 2.7: Sol-gel analysis of Poly-NDME, containing 3 wt% (black squares), 5 wt% (red circles), 10 wt% (blue triangles) and 15 wt% (green diamonds) of BAC-M. The plotted lines serve as a guide to the eye

This behaviour can be explained by a chain scission under UV-illumination, where an equilibrium state between crosslinking and chain scission occurs only at higher illumination doses.[59] Films containing 5 wt% of BAC-M result in insoluble contents of 61% at 4.1 mJ/cm^2 with a reduction to 51% after illumination with 8.1 mJ/cm^2, showing a similar behaviour as previously described. 10 wt% of BAC-M in Poly-NDME films leads to significantly higher gel fractions, reaching values of 93% at 8.1 mJ/cm^2. A BAC-M content of 15 wt% consequently lead to an insoluble fraction of 99% after illumination with 4.1 mJ/cm^2, providing sufficient crosslinking properties with a high sensitivity.

The crosslinking behaviour of Poly-NB, Poly-NDME and Poly-NDPE with a constant ratio of N_3 groups to C=C double bonds of χ_{N_3} = 1:5 was furthermore compared to determine the influence of steric effects of the side groups on the crosslinking reaction. In Figure 2.8, the resulting sol-gel curves are plotted, revealing a similar crosslinking behaviour for the investigated polynorbornene derivatives. Poly-NB and Poly-NDME exhibit a comparable progress of the curves with achievable gel fractions of 99–100% after UV-irradiation with 8.1 mJ/cm^2. Poly-NDPE shows slightly different properties with a later onset of the crosslinking curve, nonetheless lying within an acceptable range with an achievable gel fraction of 98% after illumination with UV-light with a dose of 8.1 mJ/cm^2.

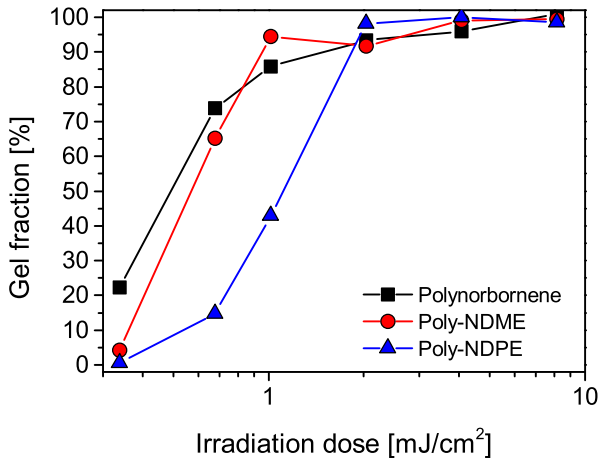

Figure 2.8: Sol-gel analysis of Poly-NB (black squares), Poly-NDME (red circles) and Poly-NDPE (blue triangles) with with a constant χ_{N_3} ratio of 1:5. The plotted lines serve as a guide to the eye

In addition to the photo-induced crosslinking, polynorbornene films with two different χ_{N_3} ratios were thermally crosslinked and the gel fraction of the individual films was measured after storing the samples *in vacuo* for 24 h at 140 °C. Table 2.1 states the measured gel fractions, showing complete crosslinking for Poly-NB films, independent of the χ_{N_3} ratio and lower crosslinking densities for Poly-NDME, lying at 91% for a ratio of χ_{N_3} = 1:5 and 75% for a ratio of χ_{N_3} = 1:11. The achievable crosslinking density of Poly-NDPE lies in a similar range as Poly-NDME at 95% for a ratio of χ_{N_3} = 1:5 and 75% for χ_{N_3} = 1:11.

Table 2.1: Thermal crosslinking of polynorbornene films, containing different amounts of BAC-M

Material	χ_{N_3}	**Gel fraction [%]**
Poly-NB	1:5	100
	1:11	100
Poly-NDME	1:5	91
	1:11	75
Poly-NDPE	1:5	95
	1:11	75

Crosslinking as a Side Reaction of the Photo-Fries Rearrangement

Poly-NDPE, an inherently photosensitive polymer bearing aromatic ester groups, is capable of undergoing the photo-Fries rearrangement upon irradiation with UV-light with a wavelength of λ = 254 nm, leading to crosslinking as a side reaction.[60,61] For the investigation of the photo-induced crosslinking reaction, Poly-NDPE with a number averaged molecular weight (M_n) of 10230 g/mol, was used. This polymer exhibits a very low dispersity of Đ = 1.07 and possesses excellent film forming properties, when spin coated from chloroform solutions. For the preparation of electronic devices also non-halogenated solvents were assessed, with anisole being a suitable solvent, which is preferred over chloroform due to its low toxicity.

Upon irradiation of Poly-NDPE with UV light with λ = 254 nm, photolysis leads to the cleavage of the aromatic ester in the polymer side chain, resulting in the formation of polymeric acyl radicals and phenoxy radicals (see Figure 2.9). Recombination of these radicals then leads to the corresponding photo-Fries product, i. e. ortho-hydroxyketone. As a side reaction, radical coupling of two polymeric acyl radicals can occur, resulting in crosslinking.[37] Alternatively, the photo-generated radicals may abstract hydrogen atoms from the polymer chain, also leading to macro-radicals,

which can subsequently recombine. Consequently, the polymer becomes insoluble in organic solvents upon UV-irradiation.

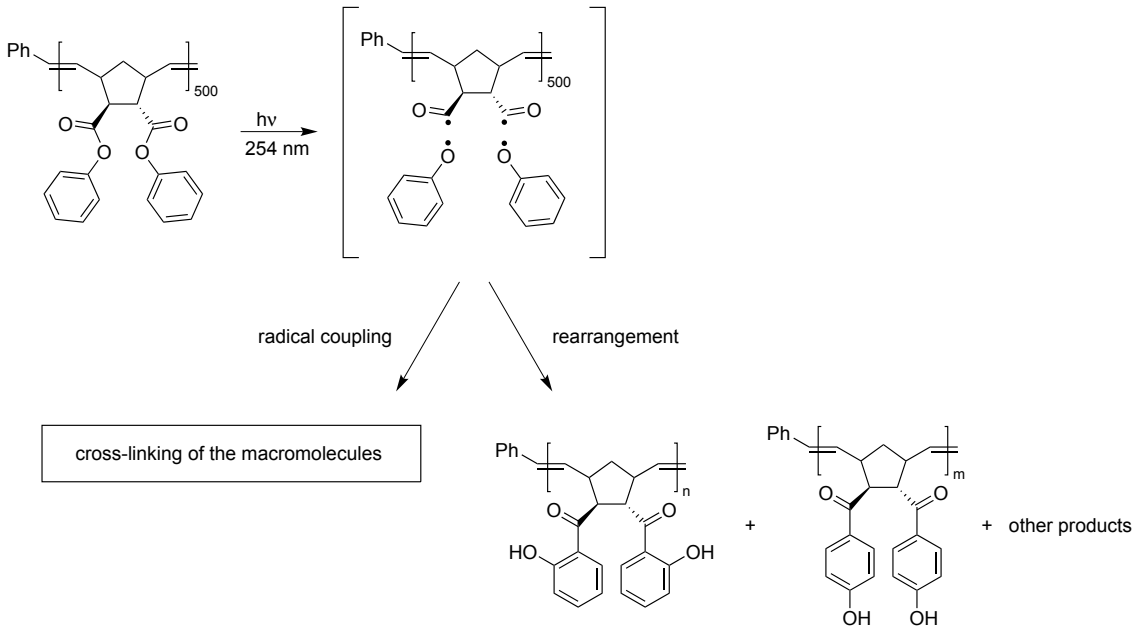

Figure 2.9: Schematic mechanism of the photo-Fries rearrangement upon UV irradiation of Poly-NPDE

The photo-induced conversion of the aromatic ester moieties was investigated by FTIR spectroscopy. Figure 2.10 shows the decrease of the C=O stretching vibration of the ester groups at 1745 cm^{-1}, which is observed during the illumination of thin Poly-NDPE films with UV-light ($\lambda = 254\,nm$, $P = 176\,\mu W/cm^2$). The decrease of the ester groups correlates with the formation of the corresponding acyl- and phenoxy radicals. The degree of recombination, leading to the formation of the described hydroxyketones, as depicted in Figure 2.9, was previously determined to be 20–25% referred to a quantitative conversion of the ester groups.[60] Residual radicals can either recombine to the starting aryl ester or undergo side reactions such as decarboxylation reactions or hydrogen abstraction, leading to a crosslinking of the polymer chains.

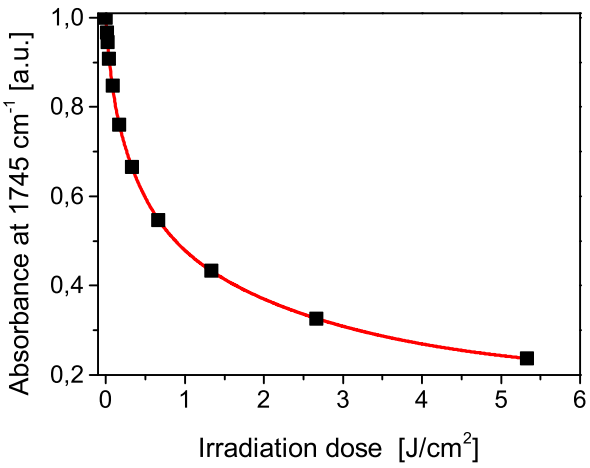

Figure 2.10: Kinetics of the photo-Fries reaction in Poly-NDPE

In order to investigate this crosslinking reaction and its influence on the solubility, a sol-gel analysis was performed. For that purpose, thin films of Poly-NDPE were illuminated for different periods of time and the insoluble fraction (gel fraction) was determined using FTIR spectroscopy by comparing the heights of the ester peak at 1745 cm^{-1} prior to- and after development in anisole. After exposure with an irradiation dose of 1.4 J/cm^2, an insoluble fraction of approximately 92% could be observed (see Figure 2.11). Prolonged illumination results in a further increase of the gel fraction towards 100%.

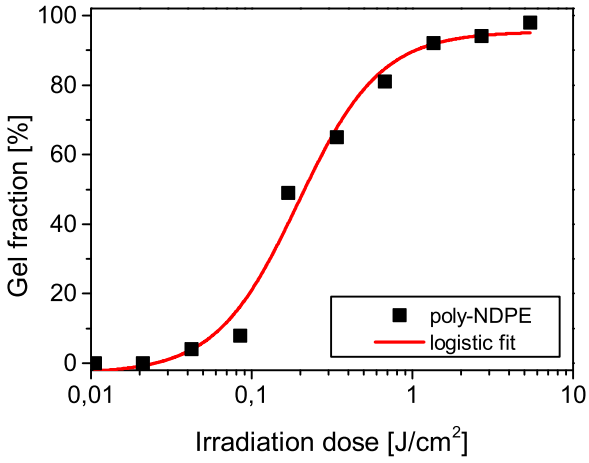

Figure 2.11: Sol-gel analysis Poly-NDPE films during UV-illumination

Calculations based on the Charlesby-Pinner equation (see Equation 2.2), reveal that an irradiation dose of 83 mJ/cm^2 is needed for the initial formation of a

three-dimensional polymeric network. This irradiation dose is also referred to as gel-point dose and provides a measure for the UV-sensitivity of photo-crosslinkable materials. [59]

$$s + s^{1/2} = \frac{p_0}{q_0} + \frac{2}{q_0 \cdot u_{w,0} \cdot D} \tag{2.2}$$

In Equation 2.2, s is the soluble fraction (determined from sol-gel analysis), p_0 is the degradation density, q_0 the crosslinking density, $u_{w,0}$ is the weight-average degree of polymerization before irradiation and D is the irradiation dose. The gel-point of thin Poly-NDPE films was determined via a plot of $s + s^{1/2}$ against the reciprocal irradiation dose, which shows a linear relationship (see Figure 2.12). The gel-point dose was calculated by solving the linear fit for $s + s^{1/2} = 2$.

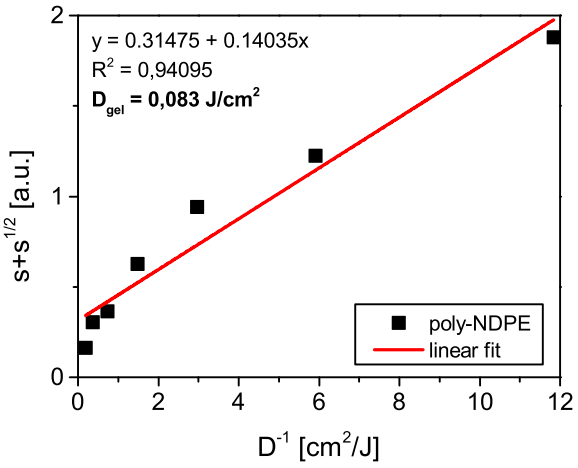

Figure 2.12: Charlesby-Pinner plot of Poly-NDPE films during UV-illumination

In order to exclude changes in solubility due to a photo-induced conversion of the aromatic ester groups to the corresponding polar hydroxyketones, an additional sol-gel analysis was performed using dimethylformamide (DMF), which is an excellent solvent for polar compounds and polymeric materials. In this experiment a similar crosslinking behaviour, leading to comparable values of the insoluble fraction, was observed. This fact excludes changes in solubility due to the formation of polar products in the polymer side chain.

To demonstrate the versatility of this crosslinking reaction for a light-induced patterning of thin Poly-NDPE layers, such films were photopatterned, using a mask-aligner system equipped with a suitable quartz chromium mask. A subsequent development in anisole led to the dissolution of the non-crosslinked areas. This

approach provides a good pattern reproducibility with resolutions in the micrometre-range (see Figure 2.13), offering the advantage that no additional photoinitiator is required and crosslinking can be carried out with short irradiation times under ambient conditions with non-halogenated solvents.

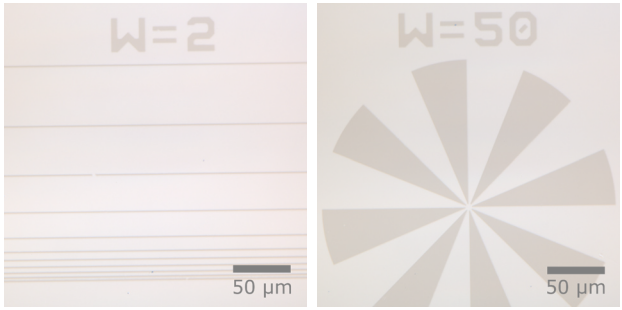

Figure 2.13: Optical micrographs of Poly-NDPE layers after patterned illumination with a mask-aligner, followed by a development step

2.2.3 Application of Poly-NDPE as a Gate Dielectric

Ultra-thin Poly-NDPE films ($d < 100\,\text{nm}$) were further implemented as a directly photopatternable dielectric material for low voltage pentacene-based OTFTs with the device architecture shown in Figure 2.14. The influence of the photopatterning process under ambient and inert conditions on the dielectric- and surface properties, as well as on the device characteristics was investigated in detail.

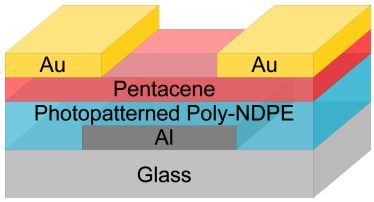

Figure 2.14: Device architecture of the pentacene based OTFTs with a photopatterned Poly-NDPE dielectric

An illumination with polychromatic UV-light under inert atmosphere led to a slight increase in polarity (ratio of the polar component γ_p of the surface energy to the total surface energy γ) from $4.3 \pm 0.4\%$ to a maximum of $6.0 \pm 0.4\%$ after illumination with a dose of $2.3\,\text{J/cm}^2$. This increase can be attributed to the photo-Fries rearrangement, resulting in the generation of hydroxyl moieties. Moreover, it was observed that after development in anisole, the polarity decreased to approximately

4.4%, independent on the UV-exposure dose. This observation may be explained by a removal of low-molecular cleavage or decomposition products, leading to a change of the chemical composition and polarity. Poly-NDPE layers illuminated under ambient conditions exhibited a polarity in the range of 12.5%, resulting in a higher total surface energy, most likely due to additional photo-oxidation products. However, after development, no significant differences of the polarity compared to illumination under inert atmosphere were observed, also suggesting a removal of these by-products.

The root-mean-squared-roughness (rms-roughness, R_q) of these layers was analysed by means of atomic force microscopy, revealing very smooth surfaces with values of $R_q = 0.24 \pm 0.02\,\text{nm}$ for untreated Poly-NDPE films, with no changes of the rms-roughness upon UV-irradiation under inert atmosphere. After development in anisole, only a slight increase of the roughness to $R_q = 0.26 \pm 0.02\,\text{nm}$ was observed, which is within the experimental error range. Poly-NDPE layers illuminated under ambient conditions show similar results with $R_q = 0.25 \pm 0.02\,\text{nm}$. After development, these films exhibit a higher roughness of $R_q = 0.84 \pm 0.02\,\text{nm}$. This increase in roughness further suggests the presence of photo-oxidation products, which are removed by the solvent during development. An UV-illumination of Poly-NDPE under inert atmosphere therefore leads to a better surface quality and was used for device fabrication. The morphology of the pentacene layer, evaporated onto these dielectric layers, shows a high degree of similarity for untreated, illuminated and developed Poly-NDPE films with grain sizes reaching up to 4.5 µm, as depicted in Figure 2.15. The large grain size and the homogeneous morphology of the pentacene layers can be attributed to the very smooth surfaces of both untreated and treated Poly-NDPE layers. Consistently, the grain size is also independent of the irradiation dose.[46]

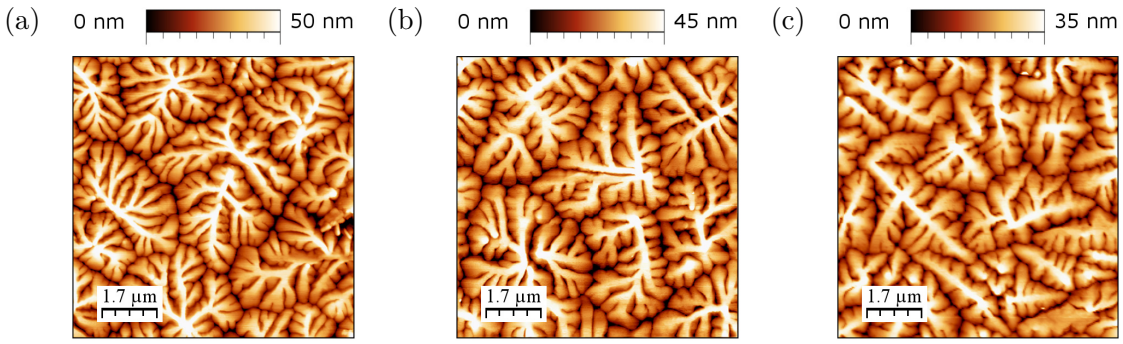

Figure 2.15: Pentacene deposited on untreated Poly-NDPE (a), after UV-illumination with $E = 0.94\,\text{J/cm}^2$ (b) and after UV-illumination and development (c). Work done by Andreas Petritz[46]

The investigated Poly-NDPE gate dielectrics exhibit a low leakage current of $10 \times 10^{-6}\,\mathrm{A/cm^2}$ at 1 MV/cm (for 39 nm Poly-NDPE layers) and a capacitance of $50\,\mathrm{nF/cm^2}$. The output and transfer characteristics of the resulting OTFTs are plotted in Figure 2.16. These devices show field effect mobilities up to $0.8\,\mathrm{cm^2/V\,s}$ at operation voltages as low as -4.5 V. The low sub-threshold swing in the order of 0.1 V/dec, as well as the hysteresis-free transistor characteristics, indicate a very low interface trap density. Furthermore, the performance of these devices is stable upon UV-irradiation and development.[46]

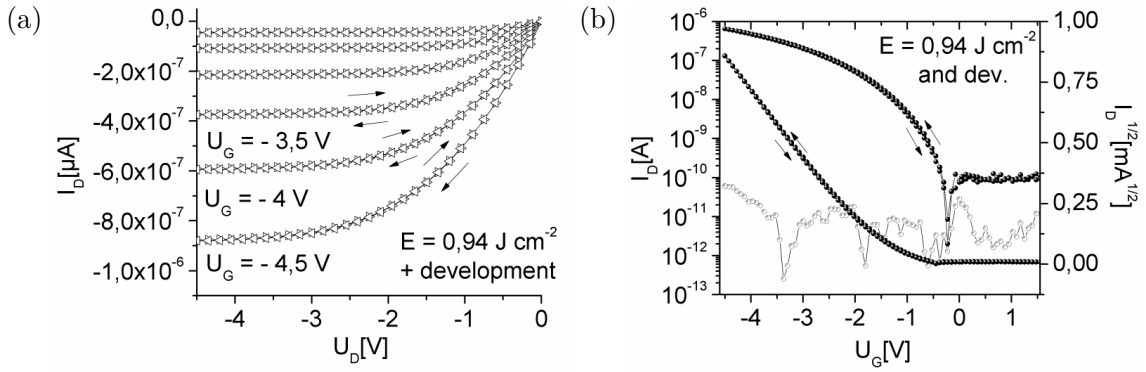

Figure 2.16: Output characteristics (a) and transfer characteristics (b) of pentacene-based OTFTs with a channel length of 70 µm and a channel width of 1.5 mm with a photopatterned Poly-NDPE dielectric layer ($E = 0.94\,\mathrm{J/cm^2}$). Work done by Andreas Petritz[46]

The excellent interface properties, as well as the high stability and low achievable film thickness of Poly-NDPE dielectrics therefore renders this material a promising candidate for high-performing OTFTs and fast organic electronic circuits.

2.3 Experimental

2.3.1 Materials

Unless otherwise stated, all chemicals were obtained from commercial sources and were used without further purification. Table 2.2 lists all used chemicals, as well as their respective source and purity.

Table 2.2: List of used chemicals (1)

Substance	**Supplier**	**Purity**
(±)*endo,exo*-Bicyclo[2.2.1]hept-5-ene-2,3-dicarboxylic acid dimethyl ester	Alfa Aesar	94%
(±)*endo,exo*-Bicyclo[2.2.1]hept-5-ene-2,3-dicarboxylic acid dichloride	Sigma Aldrich	97%
Chloroform	Roth	$\geq$ 99%
Cyclohexane	Roth	$\geq$ 99.5%
Ethyl acetate	Roth	$>$ 99.5%
Grubbs-I catalyst	Sigma Aldrich	n. a.
Grubbs-II catalyst	Sigma Aldrich	n. a.
Heptane	Fluka	$\geq$ 99%
Methanol	Roth	$\geq$ 99.5%
1-Naphthol	Sigma Aldrich	$\geq$ 99%
Phenol	Fluka	$\geq$ 98%
Pyridine	Sigma Aldrich	$\geq$ 99%
Sodium hydrogen carbonate	Roth	$\geq$ 99%
Tetrahydrofurane	Roth	$\geq$ 99.5%
Toluene	Roth	$\geq$ 99.5%

2.3.2 Methods

Thin Layer Chromatography (TLC)

TLC plates with a 0.2 mm thick silica gel layer, containing a fluorescence indicator with aluminium foil backing (Roth, N729.1), were used with cyclohexane and ethyl acetate in different mixing ratios as the mobile phase. For detection, an universal UV-lamp (CAMAG, model 29200) with a wavelength of $\lambda = 254$ nm and aqueous $KMnO_4$ solutions were utilized.

Column Chromatography

For column chromatography, silica gel 60 (0.06–0.2 mm, Roth P090.3) was used as the stationary phase, with different mixtures of cyclohexane and ethyl acetate as the mobile phase.

Gel Permeation Chromatography (GPC)

The mass- and number average molecular weights (M_w and M_n), as well as the dispersity (Đ), were determined by means of gel permeation chromatography in tetrahydrofurane. A micro-volume double piston pump with a flow rate of 1 ml/min and separation columns from Varian, with a particle size of 5 mm were utilized. The detection was done with a combined refractive index–viscosity detector (WYATT Technology, Optilab DSP). Polystyrene standards from Polymer Labs were used for calibration.

Sample Preparation

A Spin Coater (Model 4000) from Electronic Micro Systems Ltd was used with rotational speeds between 1000 rpm and 4000 rpm. Polymer films were fabricated from chloroform or anisole solutions with concentrations ranging from 5 mg/ml to 20 mg/ml, containing various amounts of bisazide.

Optical Spectroscopy

Fourier Transform Infrared (FTIR) spectra were recorded on a Perkin Elmer Spectrum One instrument with a spectral range of 450 to 4000 cm^{-1} and a resolution of 1 cm^{-1} on CaF_2 plates in transmission mode. Evaluation of the recorded spectra was done using the software OPUS 7.0. UV- and Visible Light (UV/Vis) spectra were recorded on a Varian Cary 50 UV/Vis spectrometer in absorbance mode on CaF_2 plates. The obtained spectra were evaluated, using the software Cary WinUV 3.00.

Nuclear Magnetic Resonance (NMR) Spectroscopy

^{1}H-NMR and ^{13}C-NMR spectra were recorded with a Varian 400-NMR spectrometer, operating at 399.84 MHz and 100.55 MHz, respectively and were referenced to $Si(CH_3)_4$. A relaxation delay of 10 s and 45° pulses were used for acquisition. Solvent residual peaks were used for referencing the NMR spectra to the corresponding values

given in literature. The software MestReC 4.7 was used for the evaluation of the recorded spectra.

UV-Irradiation

Unless otherwise stated, UV-irradiation was carried out under nitrogen atmosphere. The light intensity (power density) at the sample surface was measured with a spectroradiometer (Solatell, Sola Scope 2000) in the wavelength range of 230–470 nm. Table 2.3 states the used UV-sources:

Table 2.3: List of used UV-sources (1)

UV-source	**Intensity [mW/cm^2]**
Lumen Dynamics OmniCure Series 2000	0.03
Heraeus Noblelight GPH212T5L	0.18
Benda NU 72	1.3

Photolithographic patterning was carried out with a mask-aligner (SUSS, MJB4, 500 W HgXe) with a measured power density of 21.3 mW/cm^2.

Contact Angle Measurements

Contact angle measurements were conducted on a KRÜSS DSA 100 Contact Angle Measuring System. The used liquids were ultra-pure water (surface tension $\gamma = 72.8\,\mathrm{mN/m}$, separable in a polar component $\gamma_P = 51\,\mathrm{mN/m}$ and a dispersive component $\gamma_D = 21.8\,\mathrm{mN/m}$) and diiodomethane ($\gamma = 50.8\,\mathrm{mN/m}$, $\gamma_P = 0\,\mathrm{mN/m}$ and $\gamma_D = 50.8\,\mathrm{mN/m}$). The surface energy of the investigated layers was calculated via the Owens–Wendt–Rabel–Kaelble method (OWRK) from five droplets of water and diiodomethane, respectively.

Device Fabrication

Organic thin film transistors were fabricated in a staggered bottom-gate architecture. The 30 nm Al gate electrode was processed on pre-cleaned glass slides by e-beam evaporation through a shadow mask. The Poly-NDPE dielectric layer on the aluminium gate electrode was photopatterned through a metal shadow mask and rinsed with anisole to remove non-exposed areas. After the photolithographic step, a 50 nm thick pentacene layer was evaporated onto the preheated samples at 65 °C at a rate of 0.2 nm/min for the first 5 nm and 0.6 nm/min for the remaining 45 nm. Source

and drain electrodes were deposited by e-beam evaporation of gold through a shadow mask in order to form 50 nm thick contacts. After production, all samples were protected from light and stored under argon atmosphere. The channel length of the fabricated OTFTs ranged from 70 µm to 240 µm. The channel width ranged from 1.5 mm to 4.4 mm.

Electrical characterization

Dielectric properties were determined by frequency dependent capacitance (C-f) and current-voltage (I-V) measurements on sandwich structures (30 nm Al - Poly-NDPE - 50 nm Al) with an overlap area of 0.1 cm^2 on glass substrates with an LCR meter (Hioki 3532-50 LCR). Electrical measurements of the OTFTs were carried out under exclusion of light, using a parameter analyser from mb-Technologies.

2.3.3 Monomer Synthesis

(±)*endo,exo*-Bicyclo[2.2.1]hept-5-ene-2,3-dicarboxylic acid diphenyl ester (NDPE)

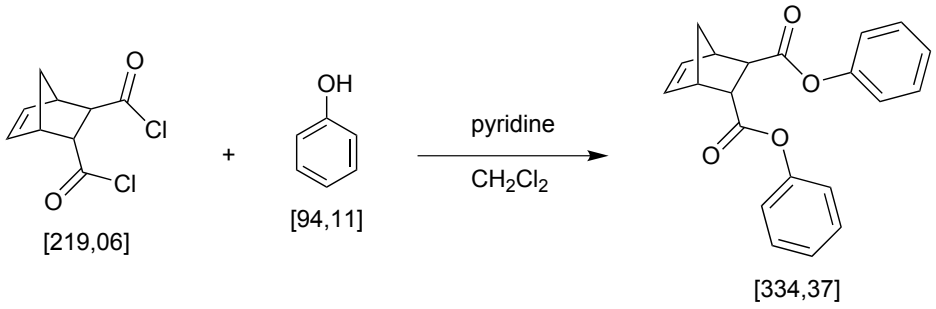

Figure 2.17: Synthesis of (±)*endo,exo*-bicyclo[2.2.1]hept-5-ene-2,3-dicarboxylic acid diphenyl ester

Phenol (20 g, 212.5 mmol) and pyridine (23.73 g, 0.3 mol) were diluted in 250 ml of dry CH_2Cl_2. (±)*endo,exo*-Bicyclo[2.2.1]hept-5-ene-2,3-dicarboxylic acid dichloride (21.9 g, 0.1 mol) was then added under vigorous stirring. The reaction mixture was stirred for 24 h at room temperature under nitrogen atmosphere and the progress of the reaction was followed by means of TLC (Cy/EA = 1). The precipitate was filtered and the product was extracted with HCl (5%, 3×80 ml), $NaHCO_3$ (sat., 3×80 ml) and H_2O (80 ml). The product was then dried under reduced pressure on a rotary evaporator. Purification was done by column chromatography (Cy/EA = 8).

Yield: 25.03 g (75%) of a white solid.

^{1}H-NMR (δ, 400 MHz, $CDCl_3$): 7.39 (m, 4 H, $ph^{3,5}$), 7.24 (m, 2 H, ph^4), 7.07, 7.13 (d, 4 H, $ph^{2,6}$), 6.43, 6.29 (m, 2 H, $nb^{5,6}$), 3.78 (m, 1 H, nb^3), 3.52 (s, 1 H, nb^4), 3.41 (s, 1 H, nb^1), 3.09 (m, 1 H, nb^2), 1.78, 1.63 (d, 2 H, nb^7)
^{13}C-NMR (δ, 125 MHz, $CDCl_3$): 172.9 (2 C, COOPh), 150.8 (2 C, ph^1), 150.8 (2 C, ph^1), 137.9, 135.1 (2 C, $nb^{5,6}$), 129.4 (4 C, $ph^{3,5}$), 125.8 (2 C, ph^4), 121.4 (4 C, $ph^{2,6}$), 48.2 (2 C, $nb^{1,4}$), 47.4 (2 C, $nb^{2,3}$), 46.1 (1 C, nb^7)

2.3.4 Polymer Synthesis

Poly(bicyclo[2.2.1]hept-2-ene) (Poly-NB)

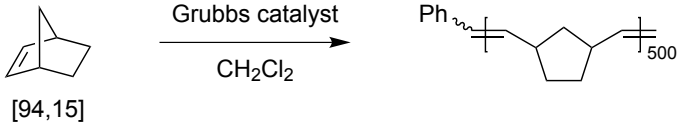

Figure 2.18: Synthesis of poly(bicyclo[2.2.1]hept-2-ene)

17.5 mg (21.3 µmol) of Grubbs-I catalyst were added to a solution of bicyclo[2.2.1]hept-2-ene in CH_2Cl_2 (998 mg, 10.60 mmol) under vigorous stirring (molar ratio 1:500). The progress of the reaction was monitored by TLC (Cy/EA = 2). The polymerization reaction was stopped by adding 100 µl of ethyl vinyl ether. The solution was then reduced to 5–10 ml under a flow of nitrogen and precipitated in cold MeOH. The precipitate was dried *in vacuo* at room temperature over night.

Yield: 750 mg (75%) of a white solid.

IR-data (cm^{-1}, CaF_2): 2943, 2864, 966
^{1}H-NMR (δ, 400 MHz, $CDCl_3$): 5.1–5.35 (2 H, CH=CH), 2.26–2.80 (2 H, $nb^{3,5}$), 1.18–1.9 (6 H, $nb^{1,2,4}$)

Poly((±)*endo,exo*-bicyclo[2.2.1]hept-5-ene-2,3-dicarboxylic acid dimethyl ester) (Poly-NDME)

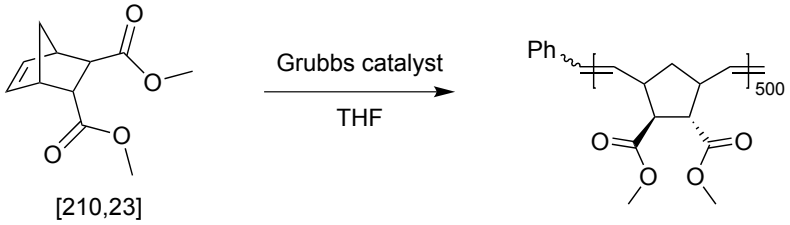

Figure 2.19: Synthesis of poly((±)*endo,exo*-bicyclo[2.2.1]hept-5-ene-2,3-dicarboxylic acid dimethyl ester)

1.73 mg (2.4 µmol) of the Grubbs-III type catalyst were added to a solution of (±)*endo,exo*-bicyclo[2.2.1]hept-5-ene-2,3-dicarboxylic acid dimethyl ester in THF (250.2 mg, 1.19 mmol), under vigorous stirring (molar ratio 1:500). The progress of the reaction was monitored by TLC (Cy/EA = 2). The polymerization reaction was stopped by adding 100 µl of ethyl vinyl ether. The solution was then reduced to 5–10 ml under a flow of nitrogen and precipitated in cold MeOH. The precipitate was dried *in vacuo* at 50°C over night.

Yield: 202.6 mg (81%) of a white–grey solid.

IR-data (cm^{-1}, CaF_2) 2953, 1732, 1437, 1200, 1170
^{1}H-NMR (δ, 400 MHz, $CDCl_3$): 5.21–5.58 (2 H, CH=CH), 3.55–3.75 (6 H, $-COOCH_3$), 2.64–3.36 (4 H, $nb^{1,2,3,5}$), 1.36–2.10 (2 H, nb^4)

Poly((±)*endo,exo*-bicyclo[2.2.1]hept-5-ene-2,3-dicarboxylic acid diphenyl ester) (Poly-NDPE)

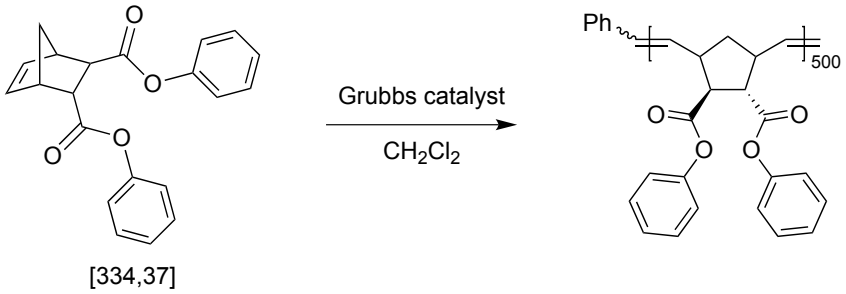

[334,37]

Figure 2.20: Synthesis of poly((±)*endo,exo*-bicyclo[2.2.1]hept-5-ene-2,3-dicarboxylic acid diphenyl ester)

3.06 mg (4.2 µmol) of Grubbs-III type catalyst were added to a solution of (±)*endo,exo*-bicyclo[2.2.1]hept-5-ene-2,3-dicarboxylic acid diphenyl ester (703.4 mg, 2.10 mmol) in CH_2Cl_2 under vigorous stirring (molar ratio 1:500). The progress of the reaction was monitored by TLC (Cy/EA = 2). The polymerization reaction was stopped by adding 100 µl of ethyl vinyl ether. The solution was then reduced to 5–10 ml under a flow of nitrogen and precipitated in cold MeOH. The precipitate was dried *in vacuo* at room temperature over night.

Yield: 664 mg (94%) of a white solid.

IR-data (cm^{-1}, CaF_2) 2954, 1751, 1592, 1492, 1192, 1183, 1141
^{1}H-NMR (δ, 400 MHz, $CDCl_3$): 6.75–7.40 (10 H, Ph), 5.40–5.86 (2 H, CH=CH), 2.84–3.74 (4 H, $nb^{1,2,3,5}$), 1.40–2.36 (2 H, nb^4)

2.3.5 Synthesis of the Grubbs-III Type Catalyst

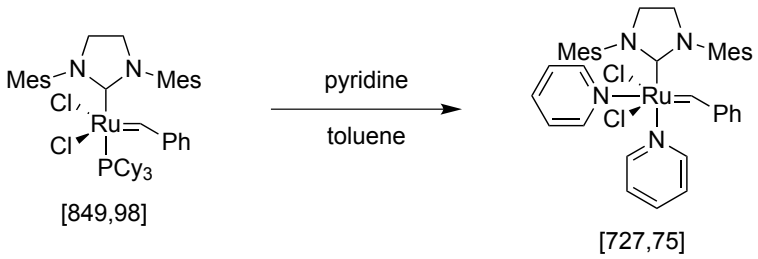

Figure 2.21: Synthesis of the Grubbs-III type catalyst

233.2 mg (2.95 mmol) of pyridine were added to a solution of Grubbs-II catalyst (50.2 mg, 59.1 µmol) in 5 ml toluene and stirred for 3 hours at room temperature. The product was precipitated in 40 ml cold heptane and filtered with a glass frit. After washing the product with copious amounts of heptane, it was dried for 3 hours at room temperature *in vacuo*.

Yield: 30 mg (60%) of a green solid.

2.4 Summary and Conclusions

In order to achieve thin, photopatternable polymer films for applications as a dielectric layer, the UV-induced crosslinking of poly(bicyclo[2.2.1]hept-2-ene) (Poly-NB), poly((±)*endo,exo*-bicyclo[2.2.1]hept-5-ene-2,3-dicarboxylic acid dimethyl ester) (Poly-NDME) and poly((±)*endo,exo*-bicyclo[2.2.1]hept-5-ene-2,3-dicarboxylic acid diphenyl ester) (Poly-NDPE) with a bisazide compound was investigated.

By adding 10 wt% 2,6-bis(4-azidobenzylidene)-4-methylcyclohexanone (BAC-M), to Poly-NDME solutions prior spin coating, a photo-induced crosslinking of thin Poly-NDME films can be achieved. This reaction was monitored by means of FTIR spectroscopy. A sol-gel analysis of Poly-NDME films, containing 3–15 wt% BAC-M was further performed, showing that the amount of bisazide significantly influences the achievable insoluble fraction and the gel-point dose. A BAC-M content of 15 wt% leads to an insoluble fraction of 99% after illumination with 4.1 mJ/cm^2, providing a sufficient crosslinking density with an adequate sensitivity of the material. A comparison of the thermal and photo-induced crosslinking behaviour of Poly-NB, Poly-NDME and Poly-NDPE was done, showing a similar crosslinking behaviour of the different materials with a minor influence of the side groups on the achievable gel-fraction and gel-point dose.

The UV-illumination of Poly-NDPE with a wavelength of $\lambda = 254$ nm leads to a photo-Fries rearrangement, which is accompanied by a crosslinking of the macromolecules. This reaction enables a selective crosslinking, which was verified by means of FTIR spectroscopy and sol–gel analysis. From the obtained sol-gel curves, a gel-point dose of 83 mJ/cm^2 was determined by means of Charlesby-Pinner calculations. Additionally, contact lithography was utilized to achieve photopatterned Poly-NDPE films with resolutions in the micrometre-range, without the need for additional photoinitiators or crosslinking components. These films exhibit very smooth surfaces with a rms-roughness of $R_q = 0.24$ to 0.26 nm for the photolithographic process under inert atmosphere and $R_q = 0.25$ to 0.84 nm under ambient atmosphere with a slight increase in polarity.

Due to the fact that Poly-NDPE is inherently photopatternable, this material was investigated as a gate dielectric, exhibiting low leakage currents of 10×10^{-6} A/cm^2 at 1 MV/cm and a capacitance of 50 nF/cm^2. The resulting OTFTs further exhibit field effect mobilities up to 0.8 cm^2/V s at operation voltages as low as -4.5 V with a

low sub-threshold swing in the order of 0.1 V/dec, as well as hysteresis-free transistor characteristics.

The good performance of these devices, as well as the excellent interface properties, high stability and low achievable film thickness therefore renders dielectric layers based on crosslinked polynorbornenes promising candidates for well-performing organic electronic circuits. The photopatterning capability of Poly-NDPE, furthermore allows a simplified processing of organic electronic devices based on this material.

3 Photolithographic Patterning of Cellulose

Parts of the work in this chapter have been published previously in *Applied Physics Letters* and are accepted for publication in *Cellulose*.[62,63] Contact angle measurements, OTFT fabrication and electrical characterization were performed at the Institute for Surface Technologies and Photonics at the Joanneum Research Forschungsgesellschaft mbH in cooperation with Andreas Petritz.

3.1 Introduction

Cellulose, as the most abundant biopolymer on earth and major component of green plants has been investigated comprehensively over the past years and still receives much interest as a versatile material in research and industrial applications, due to its unique set of properties.[64,65] Most notably, the combination of its mechanical properties, environmental stability and raw material availability renders cellulose an ideal candidate for environmentally sustainable and bio-compatible products for a wide range of applications, including papers, fibres, textiles, packaging materials, hygienic products and support materials in chromatography and life science applications.[66] In the past two decades, other cellulose-based materials also entered the focus of interest, since advances in preparation and analysis allowed to move from macro- and microscale to nanoscale materials. A wide variety of cellulose-based materials[67,68], such as nanofibrils[69], nanocrystals[70], nanofibres[71], nanoparticles[72], aerogels[73] and ultra-thin cellulose films[74–76] have recently been explored, to give just a few examples. These nanomaterials provide unique mechanical and non-linear optical properties, which have been utilized for the design of advanced functional materials.[70] Particularly, the isolation of nanocrystalline moieties from bulk cellulose leads to a variety of advanced applications of cellulose in charge storage for supercapacitors[77,78], high mechanical strength materials[79] and optics.[80] Lately, also large efforts have been made to use (nano)paper as a substrate or as a dielectric layer for organic field effect transistors, since paper offers several advantageous properties, such as low price, ready availability and excellent printability with organic polymers.[81–83]

One of the main disadvantages of cellulose, however, is its poor solubility in common organic solvents and therefore a constrained processability, limiting its applications especially in the field of organic electronics. In this regard, the possibility to fabricate thin films is an important prerequisite for the intended use as a gate dielectric in organic thin film transistors. In order to overcome these limitations, various procedures for the regeneration of cellulose from organosoluble cellulose derivatives have been developed, leading to novel biodegradable functional materials.[64] A promising derivative for the preparation of cellulose thin films is trimethylsilyl cellulose (TMSC), which, depending on its degree of substitution of Si moieties (DS_{Si}), is soluble in several common organic solvents including more eco-friendly solvents such as ethanol and can be regenerated to cellulose by a treatment with vapours or solutions of hydrochloric acid.[74,75,84] Blends of TMSC and other polymers such as styrene or lignins, have already been employed for the fabrication of micro- and nanostructures due to phase separation.[85,86] The major drawback of this method, however, is that laterally patterned structures can hardly be realized.

In many areas of research, ranging from bio-sensors to lab-on-a-chip devices or organic electronics, there is a need for efficient methods for fabricating microstructured cellulose surfaces. For the realization of complex organic circuits, high throughput methods for lateral patterning of dielectric materials are of particular importance, in order to enable the fabrication of electrical interconnections. So far, methods to create such cellulose micropatterns are rare and include soft lithography and deep UV lithography, using UV-light with wavelengths below $\lambda = 260\,\mathrm{nm}$, both of which have some disadvantages and limitations.[87,88] While the use of soft lithography is laborious, the high energy input of deep UV lithography limits its usage in a variety of material fabrication processes (e. g. for OTFT devices). In addition, the cellulose patterns are created by photo-degradation in the illuminated areas, which only allows for the realization of negative-tone photoresists.

A widely used concept for the fabrication of polymer microstructures is based on a photo-induced alteration of the solubility of polymeric materials. This concept is also applied in chemically amplified photoresists (CAR), which utilize photoacid generators (PAGs) to adjust the solubility by means of UV-light.[89] Although chemically amplified photoresists, which exploit desilylation reactions, are well known, these methods have not been used previously for the fabrication of patterned cellulose thin films from easily accessible TMSC.[90,91]

The photo-induced regeneration of cellulose from TMSC with the aid of photoacid generators is therefore investigated, enabling the fabrication of cellulose microstructures by means of UV-light. Furthermore, possibilities for the realization of both positive- and negative type cellulose patterns are explored by exploiting either changes in solubility or by utilizing selective enzymatic digestion, following the concept of dual-tone photoresists. Going a step beyond conventional lithographic techniques, the described approach allows the realization of patterned cellulose structures with sub-micrometre feature sizes by the use of advanced patterning techniques, such as two photon absorption (TPA) lithography or holographic lithography. The described biopolymer based photoresist shows a high potential for applications in organic electronics and is a suitable material for photopatternable ultrathin dielectric layer for low-voltage pentacene based OTFTs.

3.2 Results and Discussion

3.2.1 Characterization of Trimethylsilyl Cellulose (TMSC) Films

In order to determine suitable solvents for the preparation of cellulose thin films, the solubility of TMSC with a degree of substitution of trimethylsilyl groups (DS_{Si}) of 2.8, which was used for this study, was evaluated by means of gravimetric analysis. The chemical structure of TMSC is shown in Figure 3.1. Table 3.1 states the determined solid fraction of these solutions, representing the solubility of TMSC in the examined solvents. Chloroform and toluene offered the best solubility for TMSC and were therefore used for further thin film preparation and characterization.

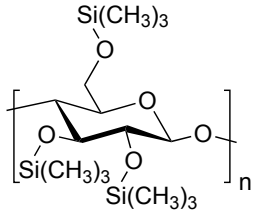

Figure 3.1: Chemical structure of trimethylsilyl cellulose (TMSC)

Table 3.1: Solubility of TMSC in different solvents

Solvent	**Solubility [mg/ml]**
Chloroform	33.6
Toluene	24.2
Dichloromethane	9.2
Heptane	9.0
Tetrahydrofurane	9.0
Anisole	2.0
Acetone	1.8

Individual TMSC films were prepared from chloroform and toluene solutions on silicon wafers with varying TMSC concentrations (c_{TMSC}) with consistent spin coating parameters ($v = 2000\,\mathrm{rpm}$, $a = 1000\,\mathrm{rpm/s}$). The film thickness (d_{film}) and rms-roughness (R_q), determined over an area of $2.5\times2.5\,\mu\mathrm{m}$, were evaluated by means of atomic force microscopy (AFM) and are summarized in Table 3.2. It can be seen, that TMSC films prepared from toluene solutions exhibit R_q values in the range of 3.4 to 9.7 nm with a film thickness between 31 and 76 nm, whereas films prepared from chloroform solutions lead to significantly lower R_q values of 0.56 to 0.68 nm

with a thickness in the range of 74 to 347 nm, also reflecting the better solubility of the investigated TMSC in chloroform. As expected, the thickness of the TMSC layers generally increases when the concentration is increased. The rms-roughness of TMSC films prepared from toluene solution also increases significantly, providing R_q values which are comparable with values reported in literature.[92–94] The TMSC films, which were prepared from chloroform solutions exhibit particularly smooth surfaces, suitable for possible applications as dielectrics in organic electronic devices.

Table 3.2: Film thickness and rms-roughness of TMSC thin films, prepared with different parameters

Solvent	$\mathbf{c_{TMSC}}$ **[mg/ml]**	$\mathbf{d_{film}}$ **[nm]**	$\mathbf{R_q}$ **[nm]**
Toluene	10	31	3.38
	20	59	5.95
	30	76	9.74
Chloroform	10	74	0.556
	20	178	0.634
	30	347	0.676

The corresponding AFM micrographs of the TMSC films prepared from toluene and chloroform solutions are shown in Figure 3.2 and reveal distinct differences in their morphology. While an increase of the TMSC concentration leads to noticeable changes in the morphology of films prepared from toluene solutions, the TMSC films prepared from chloroform solutions exhibit similar surface properties with very smooth surfaces.

A variation of the spin parameters revealed only minor differences in the film thickness and rms-roughness. Table 3.3 shows the measured values for TMSC films, spin coated from chloroform solutions with rotational speeds from $v = 2000$ to 6000 rpm with a constant TMSC concentration ($c_{TMSC} = 20$ mg/ml). These measurements also reveal very smooth surfaces with R_q values between 0.53 and 0.65 nm. Moreover, the AFM micrographs in Figure 3.3 show pinhole-free surfaces with a homogeneous morphology and a high similarity, independent of the spinning speed.

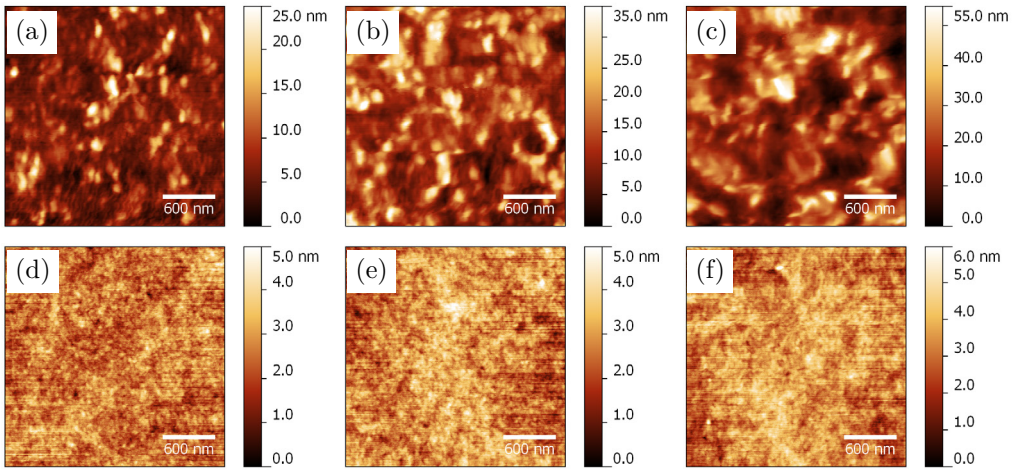

Figure 3.2: AFM micrographs of TMSC films, spin coated from toluene solutions(a-c) and chloroform solutions (d-f) with TMSC concentrations of 10 mg/ml (a,d), 20 mg/ml (b,e) and 30 mg/ml (c,f)

Table 3.3: Film thickness and rms-roughness of TMSC thin films, prepared from chloroform solutions with varying parameters

Solvent	**Rotational speed [rpm]**	$\mathbf{d_{film}}$ **[nm]**	$\mathbf{R_q}$ **[nm]**
Chloroform	2000	126	0.650
	4000	116	0.532
	6000	114	0.606

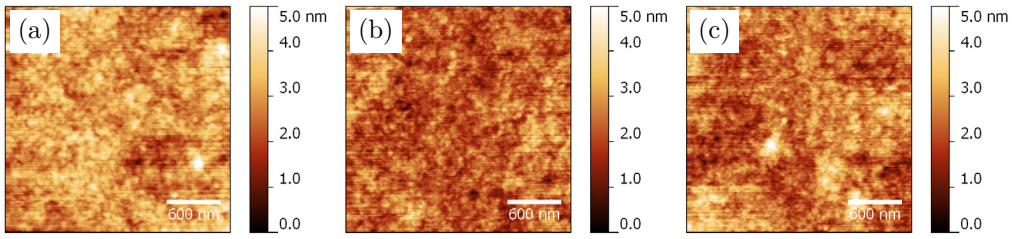

Figure 3.3: AFM micrographs of TMSC films, spin coated from chloroform solutions with rotational speeds of 2000 rpm (a), 4000 rpm (b) and 6000 rpm (c)

3.2.2 Dielectric Properties of Regenerated Cellulose Films

It has been demonstrated previously, that an acid induced desilylation of ultra-thin TMSC films with $d_{film} < 100\,\text{nm}$ is possible by an exposure to vapours or solutions of HCl, leading to cellulose films with a well defined morphology.[74] This reaction is depicted in Figure 3.4 and is also referred to as 'regeneration'. The suitability of such regenerated cellulose thin films as a dielectric layer in organic thin film transistors (OTFTs) was investigated by applying TMSC as a precursor for the fabrication of high-k dielectric layers in pentacene- and fullerene (C_{60}) based OTFTs and complementary inverter structures.

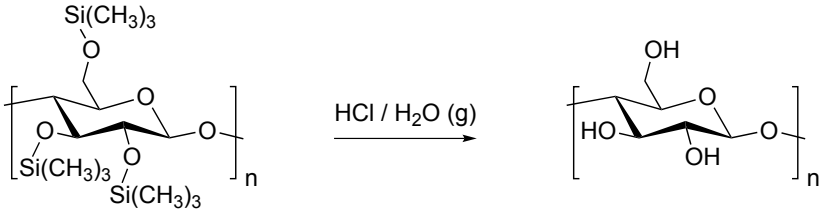

Figure 3.4: Acid induced regeneration of TMSC to cellulose[74]

These dielectric layers were fabricated by exposing spin coated TMSC films ($c = 10\,\text{mg/ml}$, $v = 2000\,\text{rpm}$, $a = 1000\,\text{rpm/s}$) to vapours of a 3 M HCl solution for 90 seconds at room temperature, whereby a desilylation takes place, resulting in fully regenerated cellulose films with a thickness of approximately 16 nm. As expected, the regeneration of TMSC to cellulose strongly influences the surface polarity and thickness of the layers, due to the cleavage of the trimethylsilyl moieties, leading to the generation of hydroxyl groups. These groups can form hydrogen bonds between and within the cellulose macromolecules, leading to a decrease of the free volume between polymer chains.[95] A schematic representation of the hydrogen bonds of cellulose macromolecules is depicted in Figure 3.5.

Moreover, the polarity of these surfaces strongly increases after an exposure to wet gaseous hydrochloric acid. A reduction of the contact angle of H_2O from $98.26 \pm 0.5°$ to $30.56 \pm 0.5°$ after 90 seconds of regeneration is observed, revealing that the desilylation reaction leads to more hydrophilic surfaces. The polarity (ratio of polar component of the surface energy γ_P to the total surface energy γ) of the prepared TMSC films increases from 7.7% to 40.5%, also confirming the acid induced desilylation of TMSC, leading to regenerated cellulose thin films. A dielectric constant of $\epsilon_R = 2.3 \pm 0.2$ for TMSC films prior to regeneration and $\epsilon_R = 8.7 \pm 0.5$ after a regeneration to cellulose was measured.[62]

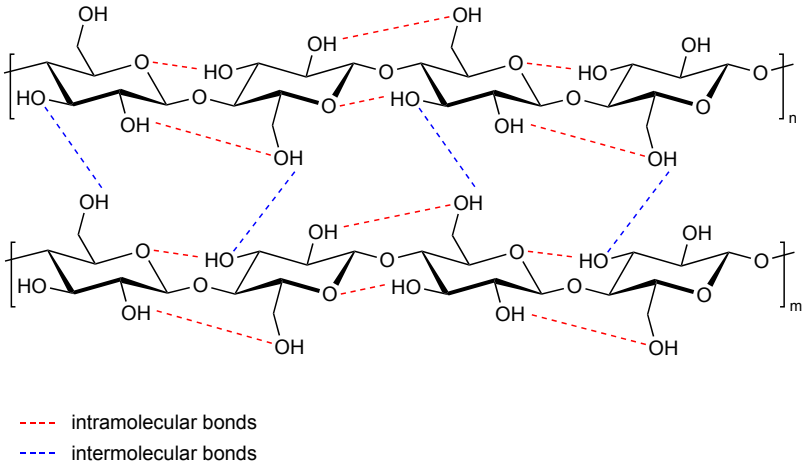

Figure 3.5: Intra- and interchain hydrogen bonding in cellulose

C_{60}- and pentacene-based OTFTs with a hybrid inorganic-organic dielectric with a 8 nm Al_2O_3 layer and a 16 nm cellulose layer, with the device setup illustrated in Figure 3.6, were furthermore fabricated.

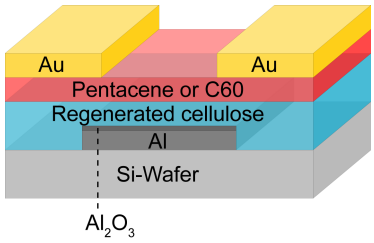

Figure 3.6: Device architecture of OTFTs with a regenerated cellulose dielectric

The electrical characteristics of the devices are plotted in Figure 3.7 and display a clear saturation of the drain current level with the gate bias and no hysteresis between forward and reverse drain voltage sweep. The C_{60}-based OTFTs operate under 3 V with no hysteresis, a low threshold voltage of 1.2 V, a small sub-threshold swing down to 190 mV/dec and a field-effect mobility as high as 0.08 $cm^2/V\,s$. Pentacene-based OTFTs show an operation voltage of -2 V, a low threshold voltage of -0.9 V, a small sub-threshold swing of 150 mV/dec and a field-effect mobility in the range of 0.1 $cm^2/V\,s$. Additionally, complementary inverters which are the basic element of any logic circuit, could be realized. These devices operate at supply voltages between 2.5 V and 3.5 V, with small-signal gains up to 60 and high balanced noise margin values of 82% at $V_{DD} = 2.5\,V$, demonstrating the potential of cellulose thin films for sustainable electronic devices.[62]

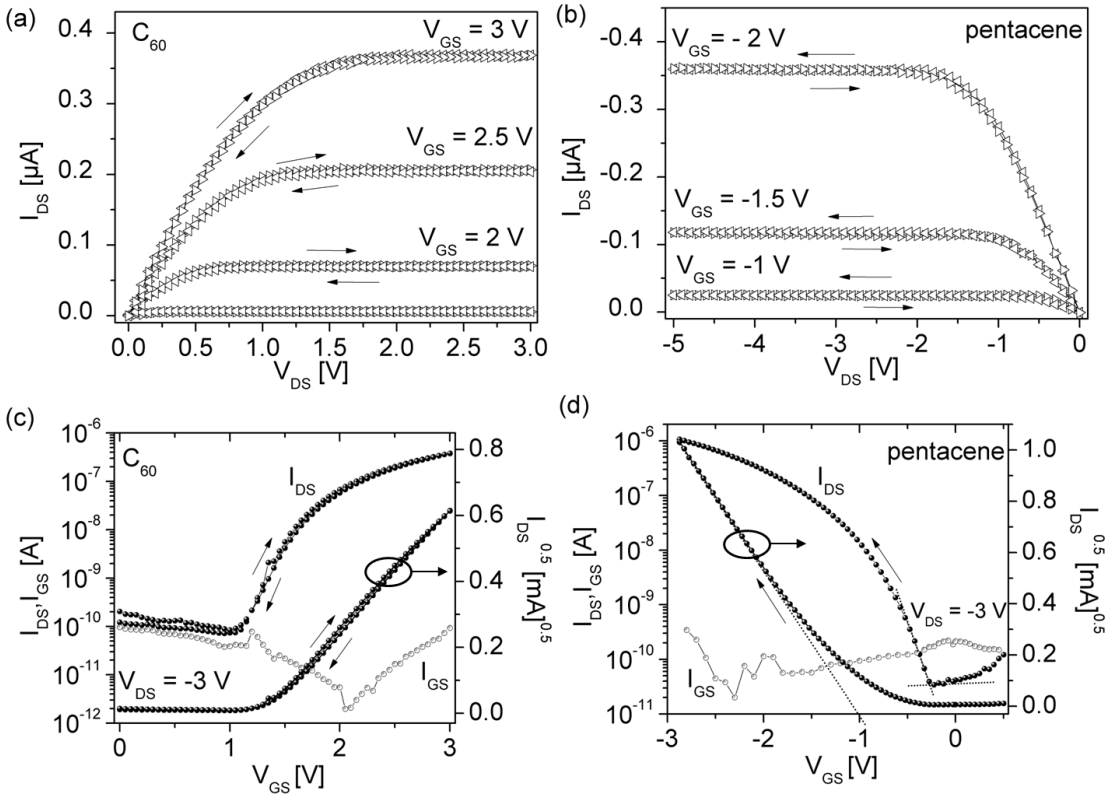

Figure 3.7: Output- and transfer characteristics of C_{60} OTFTs (a,c) and pentacene OTFTs (b,d) with channel lengths of 70 µm and channel widths of 1.5 mm with cellulose–Al_2O_3 hybrid gate dielectrics. The gate leakage current characteristics $I_{GS}(V_{GS})$ are also displayed. Work done by Andreas Petritz[62]

3.2.3 Photo-Induced Desilylation of TMSC

Since an acid induced desilylation of TMSC to cellulose is possible by exposing TMSC films to vapours or solutions of HCl (see Figure 3.4), the possibility for a UV-induced desilylation reaction with the aid of photoacid generators (PAGs) can be considered as an alternative method to achieve regenerated cellulose films. These compounds lead to the generation of an acid upon exposure to UV light and can result in a cleavage of acid labile bonds in polymers, leading to a different solubility behaviour.[96] The proposed photo-induced desilylation reaction of TMSC is shown in Figure 3.8.

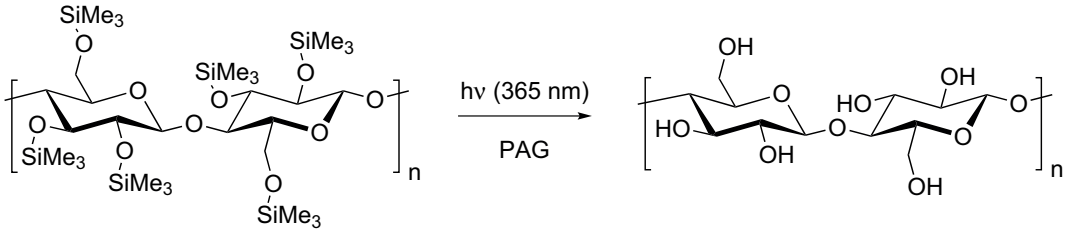

Figure 3.8: Photo-induced desilylation of TMSC, using a photoacid generator (PAG)

Investigation of the Photoreaction

In order to investigate the photo-induced desilylation of trimethylsilyl cellulose, thin films containing 1 to 10 wt% of the non-ionic photoacid generator *N*-hydroxynaphthalimide triflate (NHNT, see Figure 3.9) were prepared by spin coating onto CaF_2 plates from chloroform solutions ($c = 20\,\mathrm{mg/ml}$, $v = 2000\,\mathrm{rpm}$, $a = 1000\,\mathrm{rpm/s}$). The irradiation of the films was done directly after spin coating under ambient conditions using a medium pressure Hg lamp, equipped with a filter transmissive for wavelengths in the range from 350 to 450 nm. The filter was applied in order to prevent degradation of the cellulose, which is known to take place preferentially at wavelengths lower than 300 nm, while it is commonly accepted that light having higher wavelengths generally does not induce chemical changes in cellulose in the absence of photo-sensitizers such as TiO_2.[97]

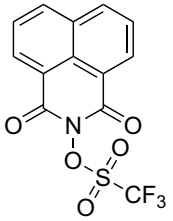

Figure 3.9: Chemical structure of *N*-hydroxynaphthalimide triflate (NHNT)

The absorption spectrum of the used photoacid generator, as well as the emission spectrum of the UV source, are plotted in Figure 3.10. It has to be noted, that the spectral overlap of the UV absorption spectrum of the PAG and the used polychromatic irradiation source is small, leading to higher irradiation times for a complete desilylation. Nonetheless, this setup was viable for an investigation of the photo-induced desilylation reaction.

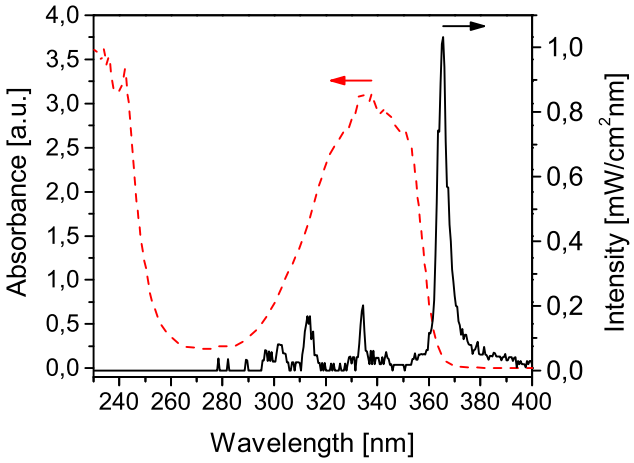

Figure 3.10: Absorption spectrum of NHNT in chloroform (red dashed line) and emission spectrum of the used polychromatic light source (black line)

UV-exposure of the used photoacid generator incorporated in the TMSC-films yields triflic acid as the main photo-product, which subsequently causes a cleavage of the trimethylsilyl groups, converting TMSC to cellulose in the irradiated areas. The photo-induced desilylation was followed by means of FTIR spectroscopy in transmission mode, by comparing the spectra before and after UV-illumination. Figure 3.11 shows the obtained FTIR spectra of thin TMSC films, containing 2 wt% NHNT, before and after exposure to polychromatic UV-light with an irradiation dose of 5.2 J/cm^2. The FTIR spectrum of these films exhibit weak signals for O-H stretching vibrations at 3490 cm^{-1} before illumination, which can be explained by an incomplete substitution of the hydroxyl moieties of cellulose with trimethylsilyl groups. These O-H bands are expected for TMSC films with a degree of substitution of 2.8, which was used for this study. Additionally, the FTIR spectrum of the non-illuminated film shows characteristic bands for C-H stretching vibrations between 2800 and 3000 cm^{-1}, as well as Si-C rocking vibrations at 1250 cm^{-1}. The complex bands at 1000 to 1200 cm^{-1} are due to combinations of C-O stretching of the glycopyranose rings and Si-O-C stretching vibrations of the attached side groups. After illumination of the TMSC-films containing 2 wt% NHNT, the intensity of the O-H stretching vibration at 3445 cm^{-1} is increased while the intensity of the Si-C rocking vibration at 1250 cm^{-1}, as well as of the C-H stretching vibrations at 2957 cm^{-1} is significantly decreased. The observed changes in the FTIR spectra show, that the photo-induced desilylation leads to an almost complete regeneration of TMSC to cellulose, which are in accordance with the proposed reaction in Figure 3.8.

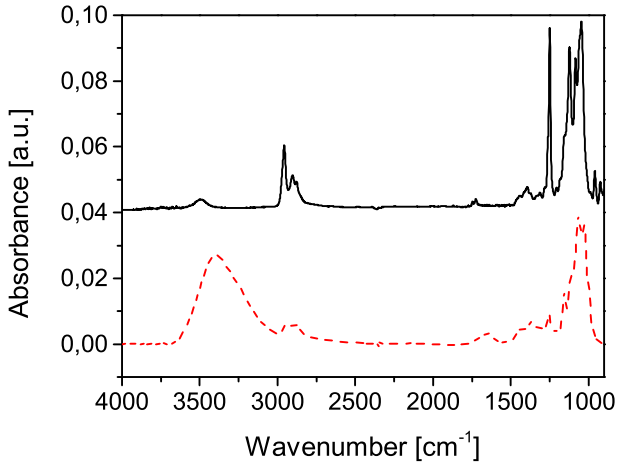

Figure 3.11: FTIR spectra of TMSC, containing 2 wt% PAG on CaF_2 before illumination (black line) and after illumination (red dashed line, $E = 5.2\,\mathrm{J/cm^2}$)

The amount of photoacid generator in thin TMSC films was found to significantly influence the degree of desilylation of TMSC. In order to determine the minimum necessary amount of NHNT, as well as the needed irradiation dose for a successful photopatterning, TMSC-solutions containing 1 to 10 wt% NHNT were freshly prepared and spin coated onto CaF_2 plates. The decrease of the Si-C rocking bands was observed via FTIR spectroscopy during stepwise illumination with polychromatic UV light. After each illumination step, FTIR measurements were performed as quickly as possible and the height of the Si-C signals of the individual films at $1250\,\mathrm{cm^{-1}}$ was evaluated. Figure 3.12 shows the relative intensities of the remaining Si-C bands during illumination with polychromatic UV-light for TMSC-films with NHNT-contents of 1, 2, 5 and 10 wt%, respectively.

In these experiments, the TMSC samples with 1 wt% NHNT only exhibit a minor decrease of the Si-C band to values of 93% of the original peak height at an irradiation dose of $7.3\,\mathrm{J/cm^2}$. TMSC films with 2 wt% already show a stronger decrease of the Si-C signal to values in the range of 71 to 73% after illumination with $7.3\,\mathrm{J/cm^2}$. The prepared TMSC samples, containing 5 and 10 wt% NHNT, however, exhibit a much stronger decline of the Si-C signal, showing an exponential decrease of the signal to 10% and 11% of the original signal, respectively, after irradiation with $7.3\,\mathrm{J/cm^2}$. For all measured samples it was observed, that the photo-induced desilylation did not proceed significantly after illumination with $1.8\,\mathrm{J/cm^2}$. However, it is well known that the photo-generated protons catalyse the desilylation reaction for a certain

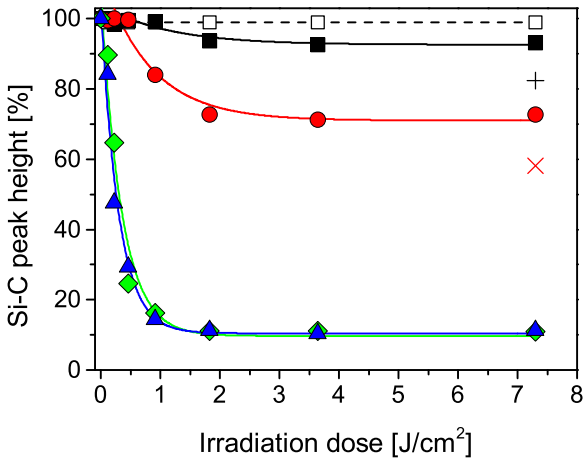

Figure 3.12: Photo-induced depletion of the silyl ether groups in TMSC films, containing no photoacid generator (open squares), 1 wt% NHNT (black squares), 2 wt% NHNT (red circles), 5 wt% NHNT (green diamonds) and 10 wt% NHNT (blue triangles) during UV-illumination and 24 hours after illumination for 1 wt% NHNT (black plus sign) and 2 wt% NHNT (red cross sign)

degree after UV-irradiation. This phenomenon is already known from cationic photopolymerization reactions and is referred to as "dark reaction". To further investigate this reaction, FTIR-spectra of the TMSC films with NHNT-contents of 1,2,5 and 10 wt%, illuminated with 7.3 J/cm^2, were recorded after storage under exclusion of light for 24 hours at ambient conditions. The remaining peak heights of the Si-C signals of the TMSC-films with 5 wt% and 10 wt% did not change significantly, whereas, the remaining Si-C signals of TMSC-films with 1 wt% and 2 wt% NHNT decreased from 93 to 82% and 73 to 58%, respectively, illustrating that for these concentrations, the desilylation reaction proceeds after the initial UV-illumination.

A decrease of the Si-C band of approximately 50 to 60%, which can be associated to a partial regeneration of TMSC to cellulose, has proven to be sufficient to allow a selective dissolution of the non-illuminated areas of the TMSC films. Therefore, for all further experiments, the NHNT-content was chosen as 2 wt%, with a subsequent storage of the samples in darkness over night after the illumination, in order to keep the photoacid generator content as low as possible, but nonetheless allowing a photolithographic patterning of the TMSC films.

Negative-type Development

A direct photolithographic patterning of TMSC films, containing small amounts of NHNT, is possible, due to the fact that the regenerated cellulose is insoluble in common organic solvents like chloroform or toluene. This leads to negative-type cellulose structures after a development in an appropriate solvent. The changes in solubility of the TMSC films, caused by the photo-induced desilylation reaction, were assessed by means of sol-gel analysis, i. e. by a comparison of the C-O-C stretching vibration of the glycosidic bond of the cellulose backbone at 1150 to 1170 cm^{-1} via FTIR spectroscopy. The insoluble content was determined by comparing the intensities of the C-O-C bands of the TMSC films directly after UV-illumination and after UV-illumination, followed by development in chloroform for 10 minutes, which allows a determination of the remaining film thickness. Figure 3.13 represents the insoluble content or gel-content of TMSC-films containing 2 wt% NHNT and 5 wt% NHNT as a function of the irradiation dose. A logistic fit of the obtained values shows a strong increase of the insoluble content of the TMSC films during UV-illumination up to an irradiation dose of 1.1 J/cm^2. At higher irradiation doses, only minor changes of the insoluble content of TMSC-samples with 2 wt% NHNT can be observed, with values ranging from 69 to 73%. TMSC-films containing 5 wt% NHNT show a similar behaviour under UV-illumination, but exhibit a higher insoluble content in the range of 91 to 98% for irradiation doses higher than 1.1 J/cm^2.

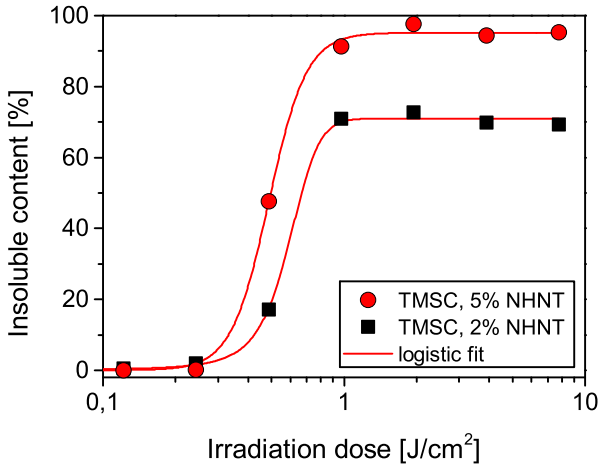

Figure 3.13: Gel-fraction (insoluble fraction) of TMSC films containing 2 wt% NHNT (black squares) and 5 wt% NHNT (red circles) during UV-illumination

In order to exclude changes in solubility caused by a UV-induced degradation of the cellulose backbone, additional TMSC-samples containing 5 wt% NHNT were illuminated with irradiation doses ranging from 10.3 J/cm^2 to 77.4 J/cm^2. The C-O-C stretching vibrations of the glycosidic bond did not change significantly after illumination and all samples showed similar values for the insoluble content (85 to 90%), indicating that for the used experimental setup, no degradation of the main polymer chains occurs.

Positive-type Development

Enzymatic digestion with cellulase from Trichoderma viride, a mixture of cellulose digesting enzymes, has already been demonstrated as a patterning method for regenerated cellulose films from TMSC by employing soft lithography.[87] The utilization of a selective enzymatic digestion of photolithographically patterned TMSC films for applications as a positive-tone resist is further investigated in this work.

In order to determine the duration needed for a complete enzymatic digestion, a TMSC-film containing 2 wt% NHNT was spin coated from a 20 mg/ml chloroform solution and was illuminated through a 10 µm quartz-chromium stripe mask with an irradiation dose of 4.6 J/cm^2. The determination of the remaining film thickness by means of FTIR spectroscopy was not applicable, because the glycosidic bonds, which were used for the previous sol-gel analysis, are expected to be hydrolysed due to enzyme activity. Since other FTIR signals were not found to be suitable for a sol-gel analysis, atomic force microscopy (AFM) was employed to characterize the films. After determination of the film thickness and rms-roughness of illuminated and non-illuminated areas by means of atomic force microscopy, the sample was immersed in a 1 mg/ml cellulase solution in sodium acetate buffer with a pH of 4.8, which was freshly prepared each time before immersing the sample for different durations. The remaining film thickness of the illuminated and non-illuminated areas, as well as the surface roughness of the illuminated areas were determined as a function of the development time. Figure 3.14 shows the remaining film thickness relative to the film thickness after UV-illumination in dependence of the duration of the enzymatic digestion. The graph reveals a steady decrease of the film thickness to approximately 4% of the original film thickness after 8 hours of immersion in enzyme solution. After 16 hours of development, no remaining cellulose film was found in the illuminated areas on the substrates. The non-illuminated areas did not change significantly in height, confirming that a selective enzymatic digestion with cellulase

is possible within the investigated system. Moreover, the rms-roughness of the TMSC films significantly increases during enzymatic digestion and decreases again after 8 hours of immersion in enzyme solution, indicating that only some residue of original film is remaining on the surface.

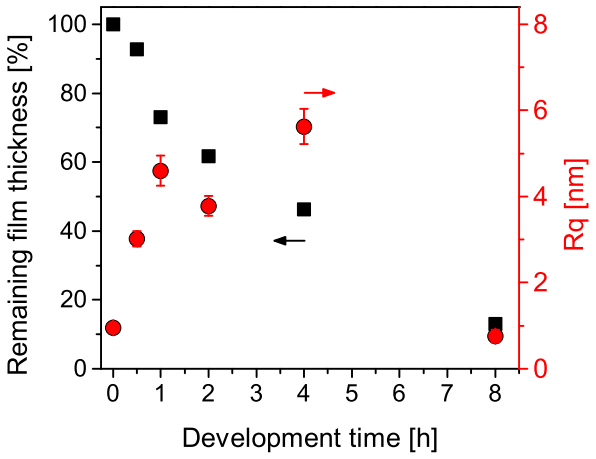

Figure 3.14: Remaining film thickness (black squares) and rms-roughness (red circles) of UV-illuminated TMSC films ($E = 4.6\,\mathrm{J/cm^2}$) after different durations of enzymatic digestion

In Figure 3.15, the remaining film thickness after enzymatic digestion of TMSC films, containing 2 wt% NHNT, is plotted as a function of the illumination dose. In this experiment the samples were illuminated through a 15 µm stripe mask with different irradiation doses, stored over night and subsequently developed in a 1 mg/ml cellulase solution in sodium acetate buffer with a pH of 4.8 for 18 hours. The remaining film thickness of the illuminated and non-illuminated areas was then determined by means of atomic force microscopy. The graph shows a steady decrease of the thickness of the remaining film to approximately 69% of the original film thickness at an irradiation dose of $0.6\,\mathrm{J/cm^2}$ and a significantly stronger decrease of the remaining thickness to 38% at an irradiation dose of $1.1\,\mathrm{J/cm^2}$. After UV- illumination with irradiation doses higher than $1.1\,\mathrm{J/cm^2}$, the films are completely digested with only some residue left on the surface. These results suggest, that the TMSC films with 2 wt% NHNT can also be partially digested after UV-illumination below a critical dose, rendering this material a possible candidate for greyscale-lithography.

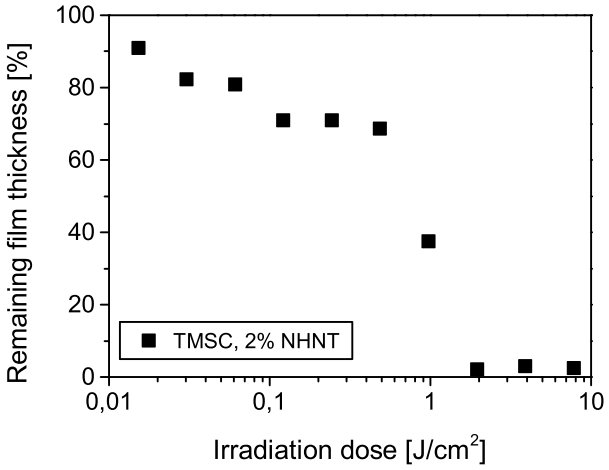

Figure 3.15: Remaining film thickness of UV-illuminated TMSC films, containing 2 wt% NHNT after development in enzyme solution

3.2.4 Investigation of the Surface Properties of Photopatterned TMSC

The rms-roughness of the differently treated samples was additionally determined by means of atomic force microscopy. Figure 3.16 shows the corresponding AFM micrographs and line roughness profiles for TMSC films, containing 2 wt% NHNT, after each treatment step. The R_q values of non-illuminated areas and illuminated areas do not differ significantly and exhibit values of 0.70 ± 0.04 and 0.78 ± 0.05 nm, respectively. After development in chloroform, the rms-roughness of the remaining cellulose surface was determined as 0.75 ± 0.05 nm, which is still within the range of variation for individually prepared TMSC films, illustrating that the development step in chloroform does not significantly influence the roughness of the remaining cellulose features. The remaining areas of photopatterned TMSC films, which were enzymatically digested and regenerated to cellulose, show an increase of the rms-roughness to 1.82 ± 0.02 nm, indicating that a positive type development with enzymes and hydrochloric acid negatively influences the surface properties to some degree under the chosen conditions.

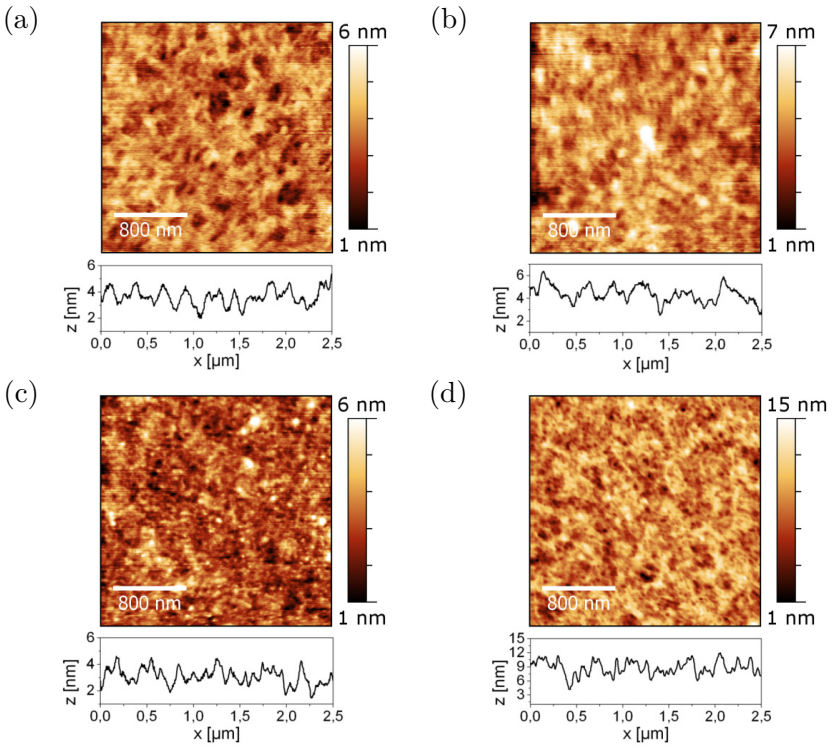

Figure 3.16: AFM micrographs and corresponding line roughness profiles of TMSC films, containing 2 wt% NHNT before (a) and after (b) illumination with polychromatic UV light ($E = 5.2\,\mathrm{J/cm^2}$), followed negative type development (c) and positive type development (d)

3.2.5 Contact Lithography

Contact lithography, which is an established method for the fabrication of well defined patterns in the micrometre- and sub-micrometre range, was employed to achieve negative- as well as positive-type cellulose structures from TMSC films.

In order to achieve cellulose microstructures on silicon wafers, TMSC films, containing 2 wt% NHNT, were spin coated from chloroform solutions with a concentration of 5 mg/ml. Photolithographic patterning of these films was performed on a mask-aligner system, equipped with a filter transmissive for wavelengths in the range of 365 nm. After UV-illumination with an irradiation dose of $5.4\,\mathrm{J/cm^2}$, the development of the TMSC films was either done in chloroform for 10 minutes for negative type patterning or, alternatively, for 18 h in a 1 mg/ml cellulase solution for positive type patterning. Figure 3.17 shows a schematic representation of the different steps, which were carried out in order to create either positive or negative-type cellulose microstructures.

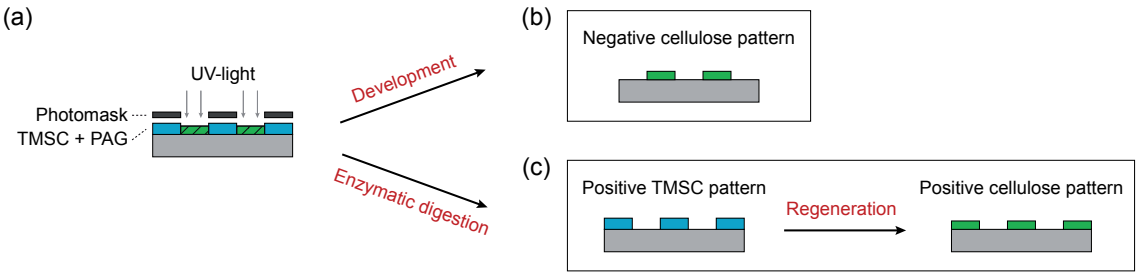

Figure 3.17: Schematic representation of the photopatterning process of TMSC (a) with subsequent development (b) or enzymatic digestion followed by regeneration (c)

After UV-irradiation of the films, a decrease in the layer thickness of the structures stemming from TMSC and cellulose, respectively, is observed. This reduction in film thickness upon conversion of TMSC to cellulose can be related to a change in the density of the film due to the removal of the trimethylsilyl groups of TMSC (see Figure 3.8 on page 51) and the formation of intra- and intermolecular hydrogen bonds of the resulting cellulose macromolecules. Figure 3.18 shows atomic force microscopy data of a TMSC film with 2 wt% NHNT, after patterned illumination on a mask-aligner ($E = 5.4\,\mathrm{J/cm^2}$). After the UV-illumination, a reduction of the film thickness of approximately 33 nm is observed in the illuminated areas, corresponding to a reduction of 23% related to the original film thickness.

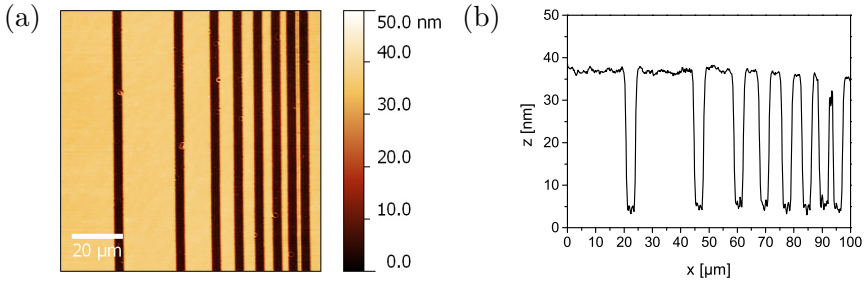

Figure 3.18: AFM micrograph (a) and corresponding line profile (b) of TMSC, containing 2 wt% NHNT after illumination on a mask-aligner

Furthermore, diffraction effects, which are most likely caused by the shrinkage of the film, can be observed at the transitions between illuminated and non-illuminated areas. These effects negatively influence the achievable resolution of the photolithographic patterning for very fine features. In Figure 3.19 an AFM image of a separate photopatterned TMSC sample, containing 5 wt% NHNT, is depicted, showing the mentioned diffraction patterns in the illuminated areas.

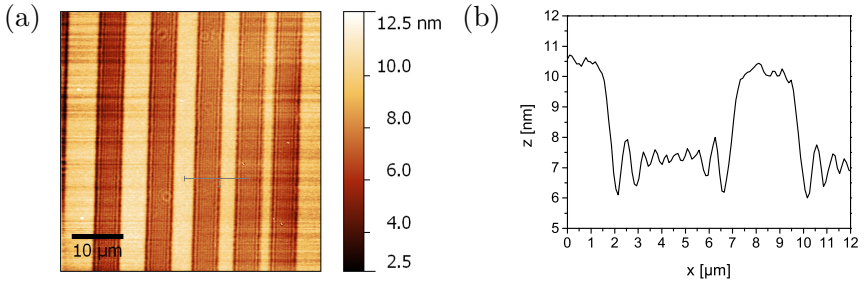

Figure 3.19: AFM micrograph of TMSC, containing 5 wt% NHNT after illumination on a mask-aligner (a) and corresponding height profile (b)

A negative-type development of these UV-illuminated TMSC films, containing 2 wt% NHNT, was accomplished by immersing the samples in chloroform for 10 minutes after photolithographic patterning, leading to a complete dissolution of the remaining non-illuminated areas. The development of the illuminated TMSC films yields well-defined negative-type cellulose structures with lateral resolution in the range of 1–2 µm. Figure 3.20 shows an AFM micrograph and the corresponding line profile of the resulting structures, featuring cellulose patterns with a line width of 4 µm and increasing gap distances of 1 to 20 µm. The height of these structures was determined as approximately 51 nm. It can be observed, that at the smallest gap distance of 1 µm an interjacent line is formed due to diffraction of the UV-light, as mentioned before. Nonetheless, the achievable resolution is adequate for low cost applications where high-throughput processing of these bio-compatible layers is desired (e. g. for large-area flexible organic electronic devices).[98,99]

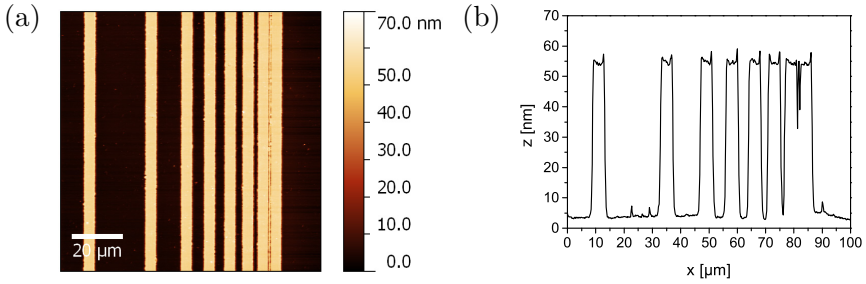

Figure 3.20: AFM micrograph (a) and corresponding line profile (b) of TMSC, containing 2 wt% NHNT after patterned illumination, followed by negative-type development

For a positive-type development of photolithographically patterned TMSC films, enzymatic digestion of cellulose using cellulase from *Trichoderma viride* was performed in order to achieve TMSC microstructures. After illumination of a TMSC film,

containing 2 wt% NHNT on a mask-aligner, the sample was developed in a 1 mg/ml solution of cellulase in an acetate buffer with a pH of 4.8, over night. The resulting TMSC patterns, shown in Figure 3.21, exhibit a varying structure height between 105 nm and 55 nm for features with a width below 10 µm.

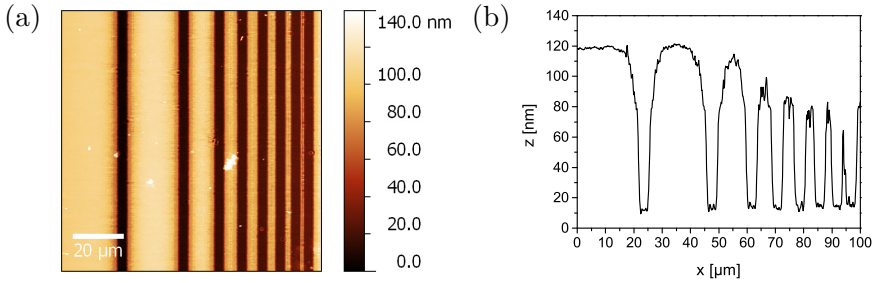

Figure 3.21: AFM micrograph (a) and corresponding line profile (b) of TMSC, containing 2 wt% NHNT after patterned illumination, followed by positive-type development

The variation in height and the lower lateral resolution of these positive-type developed TMSC films, which is in the range of some micrometres can be explained by the observed diffraction effects, where the scattered light leads to a partial desilylation of TMSC. Due to the extended time of enzymatic digestion and the fact that also partially regenerated cellulose is digested by the used enzymes[100,101], the edges of the obtained TMSC patterns are poorly defined. This behaviour is also reflected by the sol-gel analysis in Figure 3.15 on page 58. The visible particles on the surface, appearing bright in the AFM micrographs, are likely contaminations due to sample handling. The positive-type TMSC structures were furthermore regenerated to cellulose by exposing the films to vapours of hydrochloric acid for 90 seconds. Figure 3.22 illustrates the resulting AFM micrographs of the cellulose microstructures, exhibiting a reduction of the step height of 66% to approximately 36 nm, caused by the desilylation of TMSC. The achievable lateral resolution of these cellulose patterns is not further influenced by the vapour phase acid desilylation and is still adequate for various micro-structuring applications. Figure 3.23 shows additional AFM micrographs and the respective 3D-reconstructed images of the photopatterned TMSC films, illustrating the achievable resolution and line-edge properties.

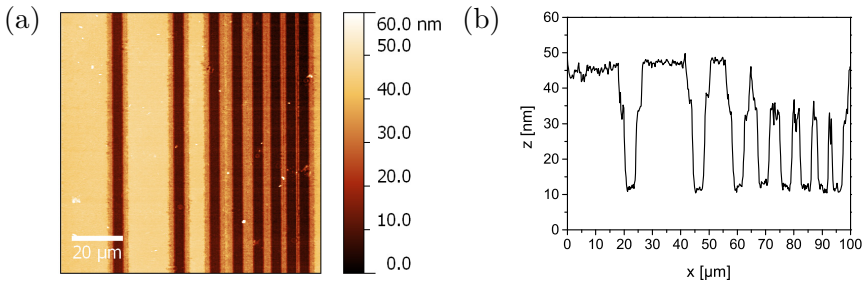

Figure 3.22: AFM micrograph (a) and corresponding line profile (b) of TMSC, containing 2 wt% NHNT after patterned illumination, followed by positive-type development and vapour phase acid regeneration

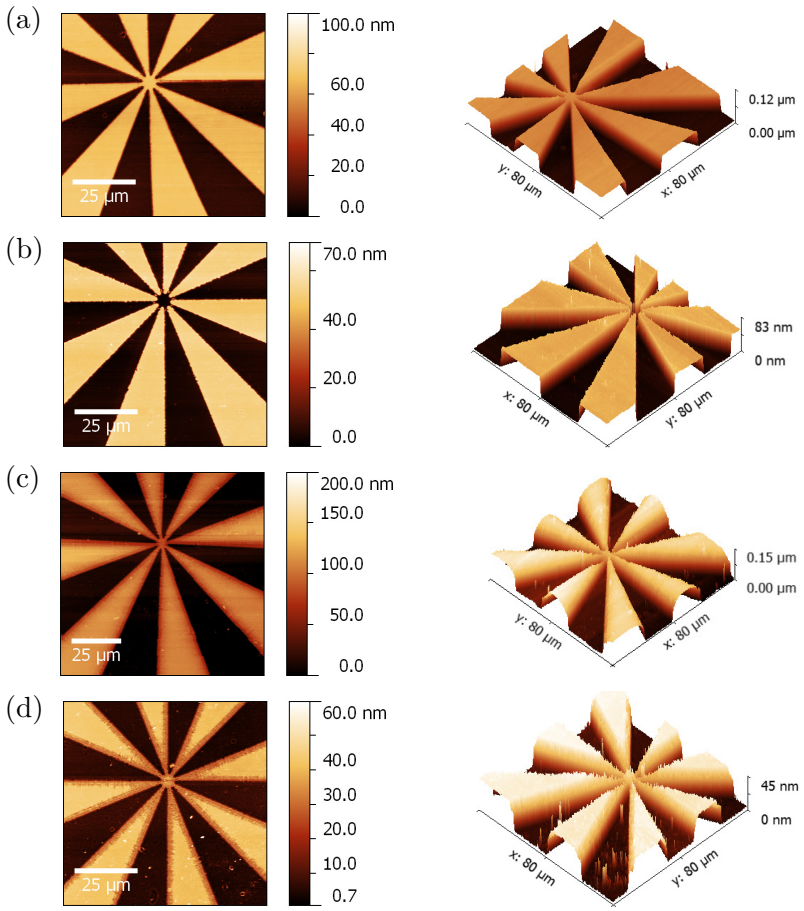

Figure 3.23: AFM micrograph and 3D reconstructed image of TMSC, containing 2 wt% NHNT after illumination (a) followed by negative-type development (b), positive-type development (c) and subsequent regeneration (d)

Photolithographic Patterning of TMSC with DS_{Si} = 1.5

To further demonstrate the possibility of using more eco-friendly solvents for the photopatterning process, the described patterning approach has been applied to TMSC with a DS_{Si} of 1.5, which is soluble in ethyl acetate. The advantage of ethyl acetate over halogenated, aromatic or even non-halogenated hydrocarbons in terms of environmental, health and safety considerations has already been reported previously.[102] TMSC films were fabricated by spin coating from ethyl acetate solutions, containing 5 wt% NHNT, onto silicon wafers. The photolithographic patterning was carried out on a mask-aligner in analogy to the previous experiments with an irradiation dose of 5.4 J/cm^2 and a subsequent development was in ethyl acetate for 30 min. Figure 3.24 depicts optical micrographs of the resulting films before and after development of the photopatterned films, revealing clearly visible patterns with micrometre-resolution. The parameters for this particular patterning experiments were not further optimized in terms of achievable resolution. Nonetheless, these results show the applicability of the described patterning approach for TMSC with various degrees of substitution of trimethylsilyl groups, also enabling the use of more eco-friendly solvents for the development step.

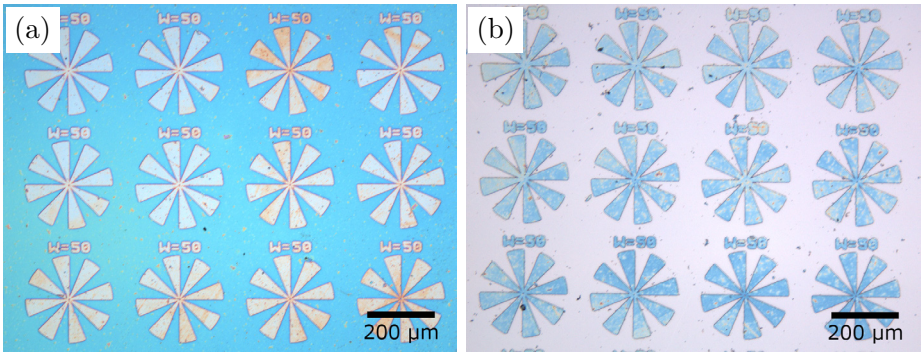

Figure 3.24: Optical micrographs of TMSC (DS_{Si} 1.5) films after patterned illumination with $E = 5.4\,J/cm^2$ (a) and after subsequent development in ethyl acetate (b)

3.2.6 Two-Photon Absorption (TPA) Lithography

Advancing from micro- to sub-micrometre resolutions, two-photon absorption (TPA) lithography was evaluated for the fabrication of highly defined cellulose patterns. The two-photon excitation technique enables the fabrication of patterns with lateral resolutions of less than 100 nm and is considered as a promising technology with

unique advantages regarding nanofabrication, due to its intrinsic 3D processing capability.[103,104] In this patterning setup, the laser beam ($\lambda = 780\,\mathrm{nm}$, repetition rate 100 MHz, pulse width 150 fs) causes multi-photon absorption in its focus area, leading to an energy transfer to the PAG, which initiates the desilylation reaction.

Because of the lower achievable resolution of enzymatic digestion in contrast to development in organic solvents, as mentioned before, only negative-type development was performed in these experiments. For the fabrication of sub-micrometre cellulose structures, TMSC films containing 5 wt% NHNT were patterned on a commercial lithographic setup (Nanoscribe Photonic Professional). A parameter screening was performed to determine the most suitable combination of laser power and lateral feed rate for generating consistent and well defined cellulose patterns. Figure 3.25 shows an optical micrograph of the resulting structures after development in toluene for 15 minutes. It was found, that at least 6–7 mW at 100 µm/s are necessary for a successful regeneration of cellulose by means of TPA.

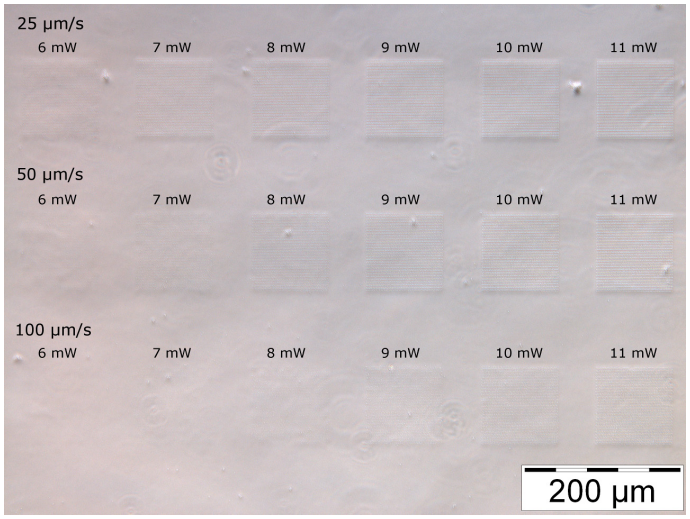

Figure 3.25: Optical micrograph of TMSC, containing 10 wt% NHNT after TPA lithography with varying parameters and subsequent development

For a compromise between the duration of patterning and a complete desilylation of the TMSC layers, a laser power of 15 mW and lateral feed rate of 50 µm/s were chosen for all further TPA experiments. Figure 3.26 shows AFM micrographs of laterally patterned TMSC films, containing 5 wt% of NHNT, obtained under the chosen conditions. The resulting cellulose patterns are already visible directly after TPA lithography, due to the expected shrinkage of the films. A subsequent development of this film in toluene for 15 minutes yields free-standing cellulose structures with a

height of approximately 180 nm and a lateral resolution of 554 nm (full width at half maximum, FWHM), as shown in detail in Figure 3.27.

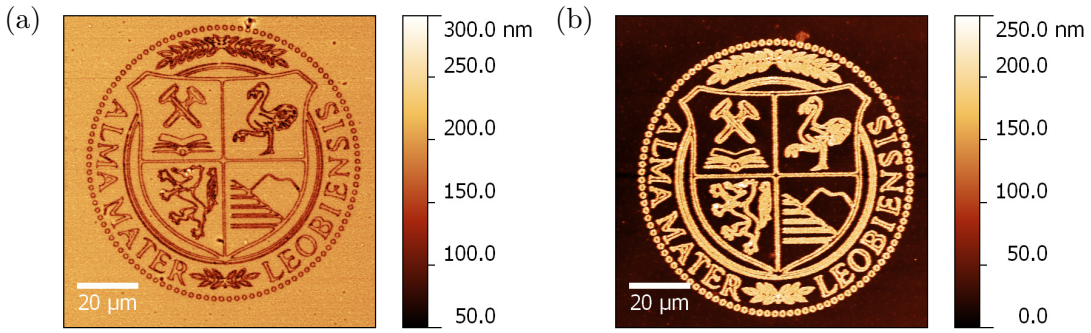

Figure 3.26: AFM micrographs of TMSC films, containing 10 wt% NHNT after two-photon absorption lithography (a), followed by a subsequent development in toluene (b)

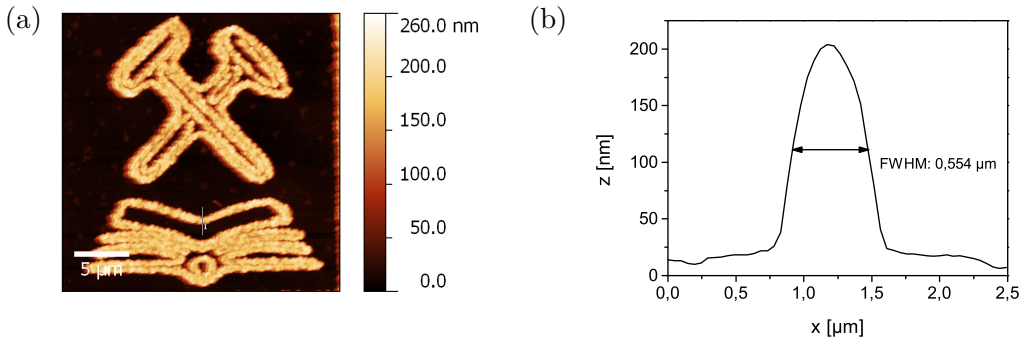

Figure 3.27: AFM micrograph of TMSC films, containing 10 wt% NHNT after illumination and development (a) and corresponding height profile of a single line (b)

These results show, that even sub-micrometre cellulose patterns can easily be achieved through the photo-induced desilylation of TMSC. Although the used photoacid generator offers an appropriate UV absorption behaviour that corresponds with the applied laser wavelength under two-photon conditions, the TPA activity of this commercially available PAG has not been determined in detail. It can be assumed, that tailored photoinitiators which provide better two-photon absorption coefficients, i. e. high TPA cross section, enable even higher resolutions, comparable to those reported for cationic photoresists. [105]

3.2.7 Holographic Lithography

Laser interference lithography was additionally investigated as a tool for the generation of periodic cellulose microstructures from TMSC.

To achieve interferometry patterns, TMSC films, containing 2 wt% of NHNT, were spin coated onto silicon wafers from chloroform solutions with a concentration of 20 mg/ml. UV-illumination was performed on an argon ion laser with a split beam setup, operating at a wavelength of 351 nm. After UV-illumination, these films were either developed in chloroform or enzymatically digested, using a cellulase solution. As already observed previously, the prepared TMSC films exhibit visible patterns directly after UV-illumination, due to a reduction of the film thickness in the illuminated areas as mentioned before. The stripe patterns, which are depicted in Figure 3.28a show some irregularities, which can be explained by a non-uniformity of the prepared TMSC films and an insufficient stabilization of the experiment setup, which requires exposure times in excess of 1 minute for a complete desilylation.

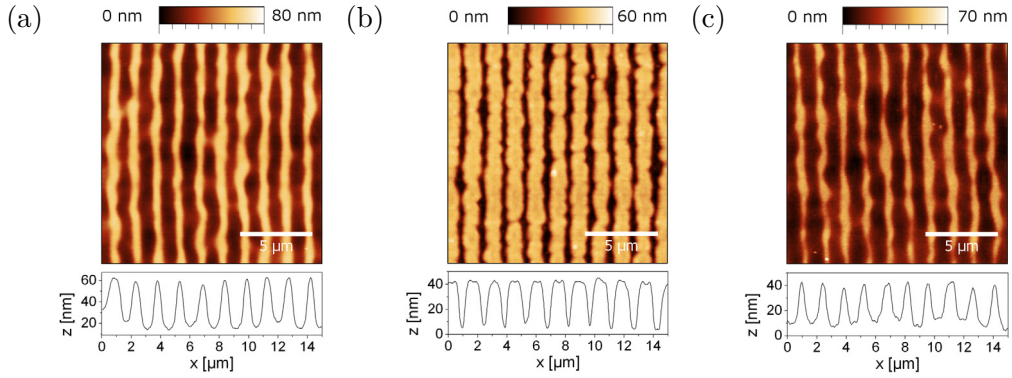

Figure 3.28: AFM micrographs of TMSC, containing 5 wt% NHNT after holographic lithography (a) followed by negative-type (b) and positive-type (c) development

The achieved patterns, visible in the AFM micrographs, show a pitch of approximately 1.5 µm and a height of the patterns in the range of 40–45 nm. A negative-type development was done in chloroform for 10 minutes in order to remove the remaining non-illuminated areas. The resulting regenerated cellulose patterns can be seen in Figure 3.28b and show similar line patterns with some irregularities. The height of the resulting cellulose patterns is in the range of 35–40 nm. After UV-illumination of the TMSC films, a positive-type development was done in a 1 mg/ml cellulase solution in acetate buffer with a pH of 4.8, in order to remove the illuminated areas containing regenerated cellulose. The resulting patterns show similar features as

observed in the previous patterning experiments. The AFM image in Figure 3.28c suggests, that the photo-regenerated areas were completely removed. The remaining TMSC patterns exhibit a height in the range of 25 to 30 nm.

Even though the resolution of these patterning experiments can still be improved, TMSC films containing a photoacid generator are in principle suited for large area interferometric patterning, providing either positive or negative cellulose patterns.

3.2.8 Application of Photopatterned TMSC as Gate Dielectric

In order to demonstrate the potential of this cellulose based photoresist in the field of organic electronics, photopatterned TMSC films were implemented as dielectric layers in low-voltage pentacene based OTFTs, with the device setup illustrated in Figure 3.29.

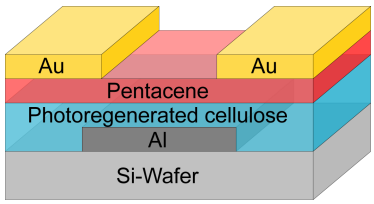

Figure 3.29: Device architecture of OTFTs with a photo-regenerated cellulose dielectric

For that purpose, the dielectric properties of 32 nm thin cellulose films, obtained by negative-type photopatterning of spin coated TMSC films, containing 2 wt% NHNT, were investigated in capacitor structures. These devices revealed leakage currents in the order of 10^{-6} A/cm^2 at an electric field of 1.3 MV/cm and a capacitance of approximately 130 nF/cm^2, corresponding to a dielectric constant of $\epsilon_R = 5.4 \pm 0.7$ at 1 kHz. The observed permittivity is significantly lower in comparison to the values observed for cellulose films fabricated by vapour phase acid hydrolysis ($\epsilon_R = 8.4 \pm 0.5$). This can be explained by residuals of TMSC in the films, due to an incomplete photo-induced regeneration of the pristine TMSC layers, which exhibit a permittivity of $\epsilon_R = 2.3 \pm 0.2$. Although, this low PAG concentration leads to an incomplete conversion of the TMSC films to cellulose, the changes in solubility are sufficient for a successful photopatterning, whereas higher NHNT contents and their ionic photo-cleavage products may negatively influence the device stability. Therefore, a NHNT content of 2 wt% was found to be ideal for the fabrication of pentacene based OTFTs.

The electrical characteristics of these devices with negative-type photolithographically patterned cellulose films as gate dielectrics are plotted in Figure 3.30 and reveal a good performance with an onset voltage $V_{on} = 0.8\,\mathrm{V}$, a threshold voltage of $V_{thr} = 1.25\,\mathrm{V}$ and a sub-threshold swing S as low as 110 mV/dec. Moreover, no hysteresis, gate leakage currents in the range of 80 pA, OFF-currents around 60 pA and a linear field-effect mobility μ_{lin} of $0.08\,\mathrm{cm^2/V\,s}$ were observed.

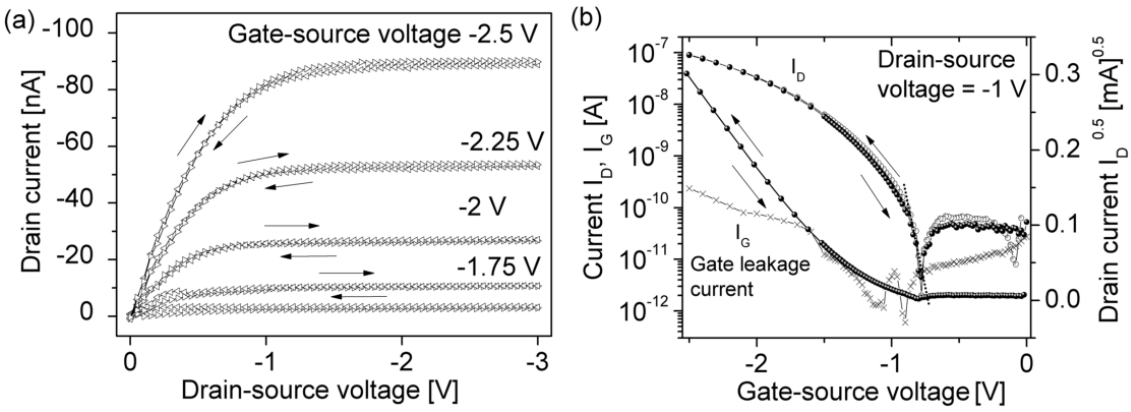

Figure 3.30: Output characteristics (a) and transfer characteristics (b) of pentacene-based OTFTs with a photopatterned TMSC gate dielectric, featuring a channel length of 70 µm and channel width of 1.5 mm. The gate leakage current characteristics $I_G(V_G)$ is also displayed. Work done by Andreas Petritz [63]

In general, patternable dielectric materials have to offer reasonable dielectric properties in addition to an appropriate resist behaviour in terms of sensitivity and resolution, which are met by the investigated cellulose based material. Furthermore, the extracted values for the interface charge trap density (N_{ss}) are exceptionally low, which is directly affecting the device performance and is particularly essential for the fabrication of fast and stable organic electronic circuits. [63]

3.3 Experimental

3.3.1 Materials

Unless otherwise stated, all chemicals were obtained from commercial sources and were used without further purification. Table 3.4 lists all used chemicals as well as their respective source and purity.

Table 3.4: List of used chemicals (2)

Substance	**Supplier**	**Purity**
Acetone	Roth	$\geq 99.5\%$
Anisole	Roth	$\geq 99\%$
Cellulase from *T. viride*	Sigma Aldrich	n. a.
Chloroform	Roth	$\geq 99\%$
N-Hydroxynaphthalimide triflate	Sigma Aldrich	$\geq 99\%$
Dichloromethane	Roth	$> 99.5\%$
Heptane	Fluka	$\geq 99\%$
Tetrahydrofurane	Roth	$\geq 99.5\%$
Toluene	Roth	$\geq 99.5\%$
Trimethylsilyl cellulose (DS_{Si} 2.8)	Thuringian Institute of Textile and Plastics Research e. V	n. a.
Trimethylsilyl cellulose (DS_{Si} 1.5)	Stefan Spirk, Graz University of Technology	n. a.

3.3.2 Methods

Sample Preparation

Silicon wafers were obtained from Taisil Electronic Materials Corp. and were rinsed with acetone and cleaned with a polymer cleaning solution (First Contact, Photonic Cleaning Technology, LLC) after cutting. A Spin Coater Model 4000 from Electronic Micro Systems Ltd was used with rotational speeds between 1000 rpm and 6000 rpm was used. TMSC films were fabricated from chloroform solutions with concentrations ranging from 5 mg/ml to 20 mg/ml, containing various amounts of photoacid generator onto silicon wafers.

UV-Irradiation

UV-irradiation was carried out with a medium pressure Hg-lamp (100 W, Newport, 66990) equipped with a filter transmissive for wavelengths in the range of 350–450 nm. The light intensity (power density) at the sample surface was measured with a UV radiometer (UV Power Puck, EIT, Inc.) and was determined as 7.6 mW/cm^2 in the spectral range from 250–390 nm (UV-A, UV-B and UV-C). Photolithographic patterning was carried out with a mask-aligner (SUSS, MJB4, 500 W HgXe) equipped with a filter transmissive for wavelengths in the range of 365 nm with a measured power density of 9.0 mW/cm^2. Holographic lithography was performed on an interferometric setup, containing a split beam setup with an argon ion laser (Coherent Innova 300C) with a wavelength of 351 nm.

TPA Lithography

For all TPA lithography experiments, a commercial lithography setup (Photonic Professional, Nanoscribe GmbH) was used. A laser power between 6 and 15 mW and lateral feed rates between 25 and 100 µm/s with a 100× oil immersion objective with a numerical aperture of NA = 1.4 and a tight focusing of the laser beam were chosen.

Development

After photolithographic patterning, development was performed in organic solvents at room temperature or alternatively via enzymatic digestion using cellulase from *Trichoderma viride* (1 mg/ml, dissolved in a 100 mM sodium acetate/acetic acid buffer at pH 4.8). The samples were immersed in 3 to 5 ml of cellulase solution at 37 °C for different periods of time.

Optical Spectroscopy

Fourier Transform Infrared (FTIR) spectra were recorded on a Perkin Elmer Spectrum One instrument with a spectral range of 450 to 4000 cm^{-1} and a resolution of 1 cm^{-1} in transmission mode on CaF_2 plates. Evaluation of the recorded spectra was done using the software OPUS 7.0. UV- and Visible Light (UV/Vis) spectra were recorded on a Varian Cary 50 UV/Vis spectrometer in absorbance mode on CaF_2 plates. The obtained spectra were evaluated, using the software Cary WinUV 3.00.

Atomic Force Microscopy

AFM micrographs were recorded with a Nanosurf FlexAFM instrument, using silicon AFM probes with a resonance frequency of 190 kHz and a force constant of 48 N/m (Tap190AL-G, Budgetsensors) in tapping mode. Evaluation of the recorded AFM images was done, using the software Gwyddion 2.32.

Contact Angle Measurements

Contact angle measurements were conducted on a KRÜSS DSA 100 Contact Angle Measuring System. The used liquids were ultra-pure water (surface tension $\gamma = 72.8\,\mathrm{mN/m}$, separable in a polar component $\gamma_P = 51\,\mathrm{mN/m}$ and a dispersive component $\gamma_D = 21.8\,\mathrm{mN/m}$) and diiodomethane ($\gamma = 50.8\,\mathrm{mN/m}$, $\gamma_P = 0\,\mathrm{mN/m}$ and $\gamma_D = 50.8\,\mathrm{mN/m}$). The surface energy of the investigated layers was calculated via the Owens–Wendt–Rabel–Kaelble method (OWRK) from five droplets of water and diiodomethane, respectively.

Device Fabrication

Organic thin film transistors were fabricated in a staggered bottom-gate top-contact architecture. The 40 nm thick aluminium gate electrode was evaporated through a shadow mask at a rate of 1 nm/s under high vacuum conditions. A metal shadow mask was used for photopatterning of the gate dielectric. After spin coating and photolithographic patterning of the dielectric, a 35 nm thick pentacene layer was evaporated. 50 nm source- and drain electrodes were deposited by thermal evaporation of gold through a shadow mask. OTFTs were fabricated with a channel-length of 70 µm and width of 1.5 mm and were protected from light and stored under argon atmosphere after their production.

Electrical characterization

Dielectric properties were determined by frequency dependent capacitance (C-f) and current-voltage (I-V) measurements on sandwich structures (30 nm Al - regenerated cellulose - 50 nm Al) with an overlap area of $0.1\,\mathrm{cm}^2$ on glass substrates with an LCR meter (Hioki 3532-50 LCR). Electrical measurements of the OTFTs were carried out under exclusion of light, using a parameter analyser from mb-Technologies.

3.4 Summary and Conclusions

Trimethylsilyl cellulose (TMSC) thin films were fabricated by means of spin coating from toluene- and chloroform solutions, showing smooth and pinhole free surfaces with a rms-roughness of $R_q = 3.4$–$9.7\,\text{nm}$ and $R_q = 0.56$–$0.68\,\text{nm}$, respectively.

TMSC films were investigated as a precursor for the fabrication of high-κ cellulose dielectric layers in pentacene- and fullerene (C_{60}) based OTFTs and complementary inverter structures. These films showed a dielectric constant of $\epsilon_R = 2.3 \pm 0.2$ and $\epsilon_R = 8.7 \pm 0.5$ after exposing TMSC films to vapours of wet gaseous HCl, with an increase of the polarity from 7.7% to 40.5%. OTFTs with hysteresis-free behaviour with low leakage currents and a well balanced mobility in the range of $0.1\,\text{cm}^2/\text{V s}$ for both p- and n-channel operation could be fabricated. Additionally, complementary inverter structures could be realized, operating at supply voltages between 2.5 V and 3.5 V, with small-signal gains up to 60 and high balanced noise margin values of 82% at $V_{DD} = 2.5\,\text{V}$.

The photo-induced desilylation reaction of TMSC films, containing 1 to 10 wt% of a photoacid generator (PAG) was investigated by means of FTIR spectroscopy. The amount of PAG in thin TMSC films significantly influences the degree of desilylation of TMSC under illumination with polychromatic UV-light, with PAG contents higher than 5 wt% showing a nearly complete desilylation, after UV-irradiation with a dose of $1.8\,\text{J/cm}^2$.

The negative-type resist behaviour of these films was evaluated by means of a sol-gel analysis, revealing an appropriate photoresist behaviour of the TMSC layers with an insoluble fraction up to 84% for 2 wt% PAG and 95% for 5 wt% PAG. A positive-type photoresist behaviour of TMSC can further be realized by the selective enzymatic digestion of photolithographically patterned films with cellulase from *Trichoderma viride*. UV-illumination and negative-type photolithographic patterning does not significantly influence the rms-roughness of TMSC films, revealing values in the range of 0.70–0.78 nm. However, after a positive-type development the remaining areas show a higher rms-roughness of $1.82 \pm 0.02\,\text{nm}$ due to a partial enzymatic digestion of the TMSC film.

Furthermore, contact lithography was employed to achieve positive and negative cellulose structures from TMSC films, containing 2 wt% PAG, on a mask-aligner system with possible resolutions in the low micrometre-range. Two-photon absorption (TPA) lithography was additionally utilized for the fabrication of highly defined

cellulose patterns in a negative-type process, resulting in cellulose structures with a lateral resolution of approximately 550 nm. Laser interference lithography was further utilized as a tool for the generation of periodic cellulose microstructures, resulting in patterns with a pitch of approximately 1.5 µm, achieved by positive-, as well as negative-type development.

The potential of these photosensitive TMSC layers in organic electronics has been demonstrated by assembling pentacene based OTFTs with an ultra-thin patterned cellulose gate dielectric with leakage currents in the order of 10^{-6} A/cm^2 at an electric field of 1.3 MV/cm and a dielectric constant of $\epsilon_R = 5.4 \pm 0.7$ at 1 kHz. These devices revealed good performance with an onset voltage $V_{on} = 0.8$ V, a threshold voltage of $V_{thr} = 1.25$ V and a sub-threshold swing S as low as 110 mV/dec. Moreover, no hysteresis, gate leakage currents in the range of 80 pA, OFF-currents around 60 pA and a linear field effect mobility μ_{lin} of 0.08 cm^2/V s were observed.

The versatile and straightforward photopatterning capability of this biopolymer-based material promises fast, highly integrated, low-voltage organic electronic circuits, with a clearly simplified fabrication of via-holes and, therefore, also a simplified design of circuits. These advantageous properties open the way for a variety of demanding bio-compatible device architectures.

4 Photo-Induced Crosslinking of Gold Nanoparticles

Parts of the work in this chapter have been applied for patenting[106] and are also in preparation for publication at the time of writing this thesis.[107] Four-point probe measurements, OTFT fabrication and device characterization were performed at the Institute for Surface Technologies and Photonics at the Joanneum Research Forschungsgesellschaft mbH in cooperation with Andreas Petritz. UV-photoelectron spectroscopy was performed by Alexander Fian.

4.1 Introduction

The possibility for a direct patterning of electrically conductive thin films plays an important role for a cost effective fabrication of components for electronic devices, such as radio-frequency identification (RFID) tags[108], organic light emitting diodes (OLEDs)[109], organic thin film transistors (OTFTs)[110,111] or organic solar cells[112], as well as (semi)transparent coatings[113]. In the field of organic electronics, an economical and efficient fabrication of electrically conductive structures is of particular interest and can be achieved by utilizing high-throughput solution-based processing methods.[8] In this regard, especially for a solution-based fabrication of conductive structures and electrodes, conductive polymers[114,115], metallic nanoparticles[116,117] or carbon based materials, such as carbon nanotubes (CNT)[118,119] and graphene[120,121] are suitable materials and allow a processing without the need for costly and time-consuming vacuum steps.

Among the mentioned material classes, stabilized metallic nanoparticles have already proven to be suitable candidates for the fabrication of electrodes, due to the fact that their physical and chemical properties can be tailored to the specific application.[122,123] Hereby, the conductivity of sintered metallic nanoparticle films can reach the range of the conductivity of vapour deposited metal layers.[124] Depending on the particle size and on the stabilizing ligands, nanoparticle layers can be sintered even at temperatures below 200 °C[125,126] to give electrically conductive layers, therefore also enabling the use of flexible polymer substrates. A further important issue for a successful use of solution-processable materials is the availability of

appropriate high-resolution patterning techniques. Besides indirect structuring techniques of nanoparticle layers, such as immobilization methods on functionalized surfaces[127,128] or transfer printing methods[129], also a variety of methods for a direct patterning of nanoparticle layers in the micrometre or sub-micrometre range have been reported. Direct patterning can be achieved by various methods, including laser sintering[126], electron beam sintering[130], soft lithography[131] and various photolithographic techniques[132–134]. Compared with indirect patterning techniques, methods for a direct patterning often have the advantage that the resulting height of the structures can be easily adjusted, enabling structures with a high aspect ratio of height to width, which is typically desired for applications in electronics and optics. However, drawbacks of the described methods for the patterning of stabilized metallic nanoparticles often reside in large efforts and costs in terms of both operation and equipment, which renders them inefficient for high-throughput industrial applications. In many cases also comparably high sintering temperatures are required to fabricate electrically conductive structures from Au-nanoparticles, limiting their application on polymer substrates.

In order to combine the advantages of a direct patterning with high resolutions and sintering at moderate temperatures, the UV-induced crosslinking of stabilized Au-nanoparticles is investigated. As a result thereof, a loose network of crosslinked particles is formed so that the organic content, i. e. the remaining stabilizing ligands and crosslinking agent, can be removed at temperatures below 250 °C. These moderate temperatures are advantageous for an efficient fabrication of electrically conductive structures on flexible polymer substrates. Moreover, photolithographic patterning methods possess the advantage of being well known and established techniques, facilitating an implementation of this method in well-controlled fabrication processes.

4.2 Results and Discussion

4.2.1 Synthesis of Stabilized Au-Nanoparticles

Gold nanoparticles with different stabilizing ligands and organic content were investigated and characterized. The chemical structure of the nanoparticles, used in this work is shown in Figure 4.1.

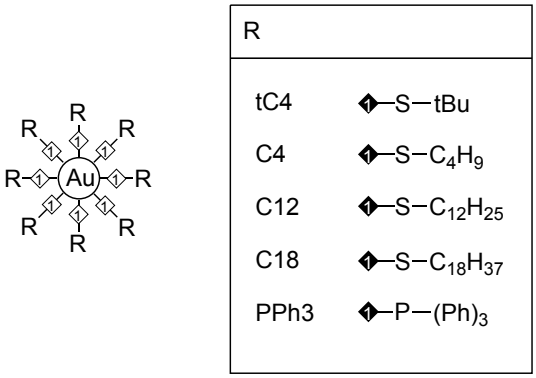

Figure 4.1: Chemical structure of the investigated stabilized Au-nanoparticles

These nanoparticles were synthesized according to the method described by Brust et al.[135] with adapted synthesis conditions, in order to influence the resulting particle size and allow for an easier material handling. The synthesis of gold nanoparticles stabilized with *tert*-butylthiol (tC4), 1-butanethiol (C4), 1-dodecanethiol (C12) and 1-octadecanethiol (C18) was performed with a molar ratio of thiol groups to $AuCl_4^-$ ions of $\chi_{SH/Au} = 2$. After 3 hours of reaction time, the products were precipitated in ethanol and dried *in vacuo*, leading to yields of approximately 40–60%.

By adjusting the $\chi_{SH/Au}$ ratio during synthesis, it is possible to influence the resulting particle-cluster sizes and, therefore, also the physical properties of the nanoparticles.[122] A ratio of $\chi_{SH/Au} = 2$ was found to be ideal in this respect for 1-butanethiol stabilized nanoparticles. These particles are of particular interest for the desired application as electrodes, due to their physical properties, generally allowing relatively low temperatures for sintering.[136] Synthesis with $\chi_{SH/Au} = 2$ resulted in a powdery material with a dark brown colour, which can be easily re-dispersed in organic solvents, such as toluene or chloroform. A thiol to gold ratio of $\chi_{SH/Au} = 1$, in contrast, led to a more waxy material, being more difficult to handle, e. g. for sample preparation.

Au-nanoparticles stabilized with triphenylphosphane (PPh3) were synthesized in analogy to alkanethiol stabilized particles with a molar ratio of phosphor to $AuCl_4^-$

ions of $\chi_{P/Au} = 3$. The product was precipitated in heptane after 3 hours of reaction time and dried *in vacuo*, leading to a yield of 52% for this particular synthesis.

4.2.2 Au-Nanoparticle Characterization

UV/Vis Spectroscopy

UV/Vis measurements of all prepared nanoparticles were performed in chloroform and are shown in Figure 4.2. The measurements reveal characteristic absorbance curves with a weak surface plasmon absorption peak at 514 nm for C4 Au-nanoparticles and at 502 nm for tC4 Au-nanoparticles. All other investigated stabilized nanoparticles do not show a pronounced plasmon resonance peak, indicating that some larger particles with core diameters $d_{core} > 2$ nm or particle aggregates are present in the C4- and tC4 nanoparticle dispersions.[123]

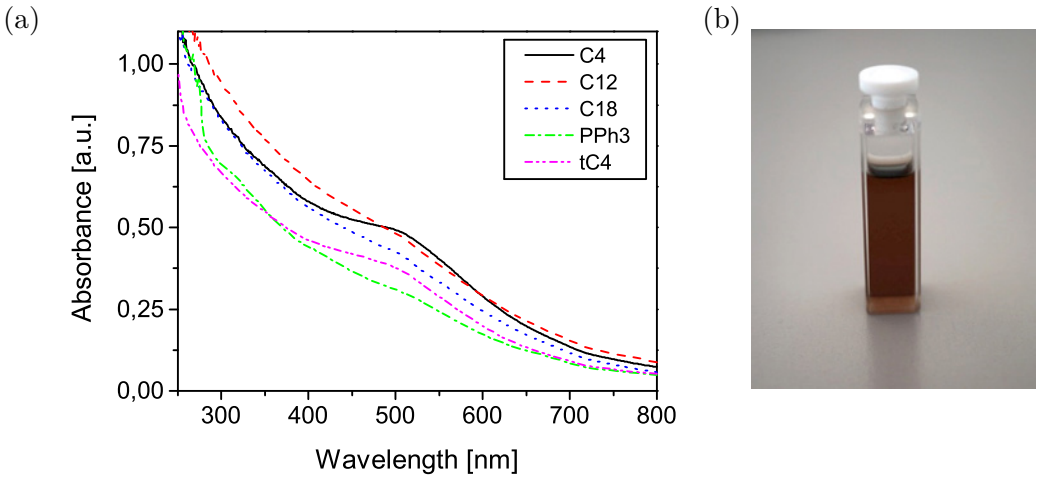

Figure 4.2: UV/Vis spectra of the investigated Au-nanoparticles (a) and photograph of a dispersion of AuNP-C4 in chloroform (b)

Transmission Electron Microscopy (TEM)

To determine the size and size distribution of the synthesized nanoparticles, transmission electron microscopy (TEM) measurements were conducted. The samples were prepared by placing small amounts of the nanoparticle dispersions on a carbon coated copper grid, followed by evaporation of the solvent. Figure 4.3 shows the recorded TEM images of 1-butanethiol stabilized Au-nanoparticles, revealing uniform particles with a mean size of approximately 5 nm.

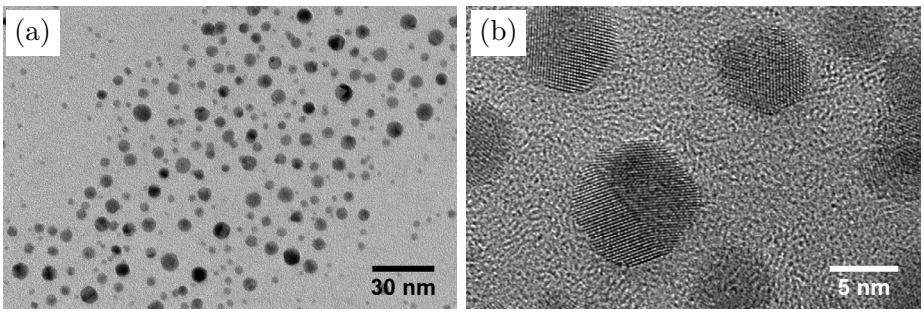

Figure 4.3: TEM images of 1-butanethiol stabilized Au-nanoparticles

The particle size and size distribution shown in Figure 4.4 were determined by an evaluation of the TEM images and are in good accordance with the conducted UV/Vis measurements. A mean diameter of 4.96 ± 2.05 nm was determined with particle sizes ranging from 1.35–10.61 nm, whereby the particles with diameters $d_{core} > 2$ nm most likely contribute to the plasmon resonance peak visible in the UV/Vis spectrum in Figure 4.2.

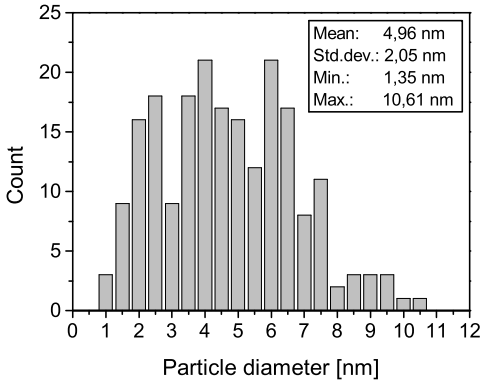

Figure 4.4: Particle size distribution of C4 Au-nanoparticles

TEM measurements of 1-dodecanethiol and 1-octadecanethiol stabilized Au-nanoparticles, illustrated in Figure 4.5, exhibit similar particle shapes and sizes with diameters in the range of 2–5 nm. An exact determination of the particle size distribution was not possible due to a lack of contrast of the TEM images, impeding an exact evaluation of the images.

The synthesized triphenylphosphane stabilized Au-nanoparticles exhibited a poor solubility behaviour due to some aggregation of the particles, leading to an insoluble residue. This behaviour is also reflected in the TEM images, where larger aggregates with particles having diameters of 10–20 nm (see Figure 4.6a), as well as smaller particles with diameters in the range of 2–3 nm (see Figure 4.6b), are observed.

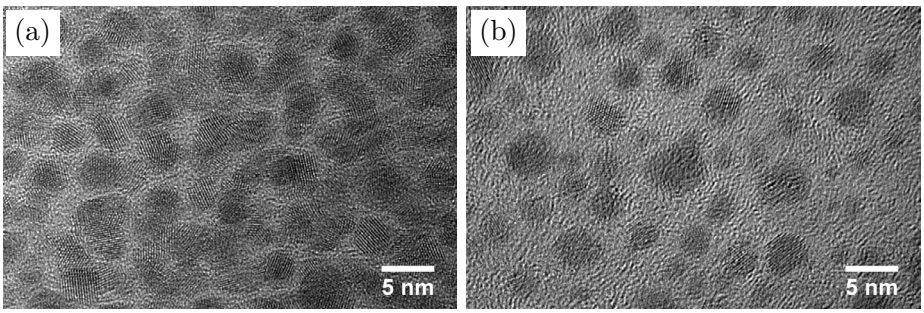

Figure 4.5: TEM images of 1-dodecanethiol (a) and 1-octadecanethiol (b) stabilized Au-nanoparticles

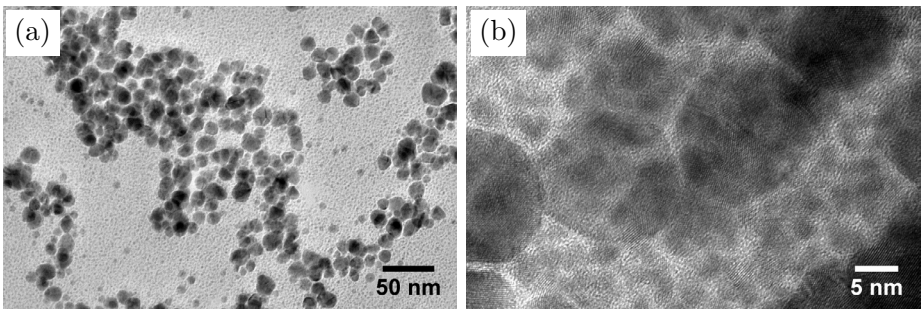

Figure 4.6: TEM images of triphenylphosphane stabilized Au-nanoparticles

Au-nanoparticles with *tert*-butylthiol as a stabilizing ligand also showed a poor solubility behaviour. Similar to the PPh3 nanoparticles, some insoluble material remained when dispersing the material in chloroform. The TEM measurements in Figure 4.7 reveal a heterogeneous particle size distribution with cluster sizes ranging from 2–20 nm in diameter. This inconsistent particle size distribution is most likely due to the poor stabilizing ability of the tC4 ligands in combination with a low thermal stability, leading to an aggregation of the particles even at low temperatures.

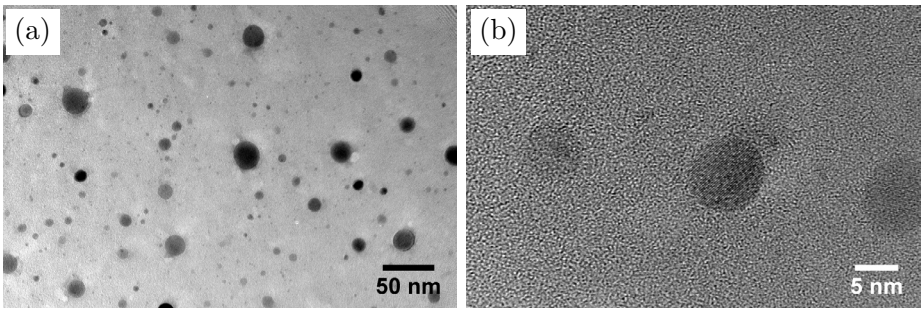

Figure 4.7: TEM images of *tert*-butylthiol stabilized Au-nanoparticles

Thermal Analysis

Thermogravimetric analysis (TGA) was employed to determine the influence of the stabilizing ligands on the required sintering temperature. Small amounts of the different nanoparticles were therefore heated from room temperature to 600 °C at a heating rate of 10 °C/min under nitrogen atmosphere. The TGA measurements of the different Au-nanoparticles reveal characteristic weight loss curves, as shown in Figure 4.8, due to a desorption of the stabilizing ligands. The extracted values for the onset temperature of the main mass loss (T_{onset}) and the differential thermogravimetry (DTG) peak temperatures (T_{peak}), representing the temperature at which the highest mass loss occurs, are additionally listed in Table 4.1.

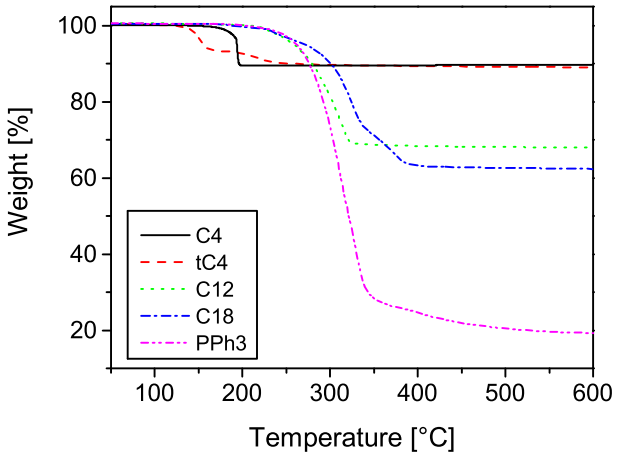

Figure 4.8: Weight loss curves of C4 (black line), tC4 (red dashed line), C12 (green dotted line), C18 (blue dash-dot line) and PPh3 (magenta dash-double dot line) Au-nanoparticles

Table 4.1: Extracted values for the mass loss, onset temperature and peak temperature of the mass loss of the investigated Au-nanoparticles

Ligand	**Mass loss [%]**	**T_{onset} [°C]**	**T_{peak} [°C]**
tC4	11	139	152
C4	12	203	206
C12	32	272	316
C18	37	292	330
PPh3	77	282	316

It can be seen, that the onset temperature generally increases with an increasing chain length of alkanethiol stabilized particles (tC4, C4, C12 and C18). This behaviour has been described in literature and can be ascribed to the differences in volatility of the stabilizing ligands. It has been observed that ligands with higher molecular weight generally show a higher thermal stability.[137] The investigated alkanethiol stabilized Au-nanoparticles feature onset temperatures in the range of 139 to 292 °C, whereas triphenylphosphane stabilized Au-nanoparticles show an onset of the main mass loss at 282 °C. Moreover, the measured total mass loss corresponds well with the organic content of the stabilizing ligands. The stated DTG peak temperatures are often used for a comparison of the sintering temperature[138] and lie between 152 to 330 °C for the alkanethiol stabilized Au-nanoparticles and at 316 °C for the triphenylphosphane stabilized particles. With regard to organic electronics, where fabrication processes are ideally compatible with flexible substrates (i. e. polymer films), low processing temperatures are desired. The stated T_{onset} and T_{peak} values, however, do not represent the lowest possible temperature at which sintering of Au-nanoparticle layers is possible, due to the fact, that the sintering process proceeds at a certain rate, depending on particle size, temperature and additional oxidation processes.[136]

In order to investigate the sintering process at lower temperatures and to determine the influence of oxygen on the destabilization of C4 Au-nanoparticles, isothermal TGA measurements were performed at 150 °C in different atmospheres. This temperature was chosen due to the fact, that a minor mass loss was observed in the TGA measurements for C4 nanoparticles at 150 °C. The TGA curves were obtained by heating the samples to 150 °C under nitrogen atmosphere at a heating rate of 10 °C/min, changing the atmosphere in the measurement chamber and monitoring the mass loss as a function of time at constant temperature. Figure 4.9 shows the corresponding weight loss curves of three C4 Au-nanoparticle samples, measured in nitrogen, synthetic air and oxygen, respectively, as a function of time. A clear influence of the oxygen content on the duration needed for a desorption of the stabilizing ligands is visible. The respective DTG peak of the main mass loss occurs after a duration of 55 minutes under nitrogen atmosphere and decreases significantly to 30 minutes in synthetic air and to 15 minutes in oxygen, demonstrating that the investigated nanoparticles are suitable candidates for the preparation of conductive layers at processing temperatures, which are compatible with polymer substrates.[139]

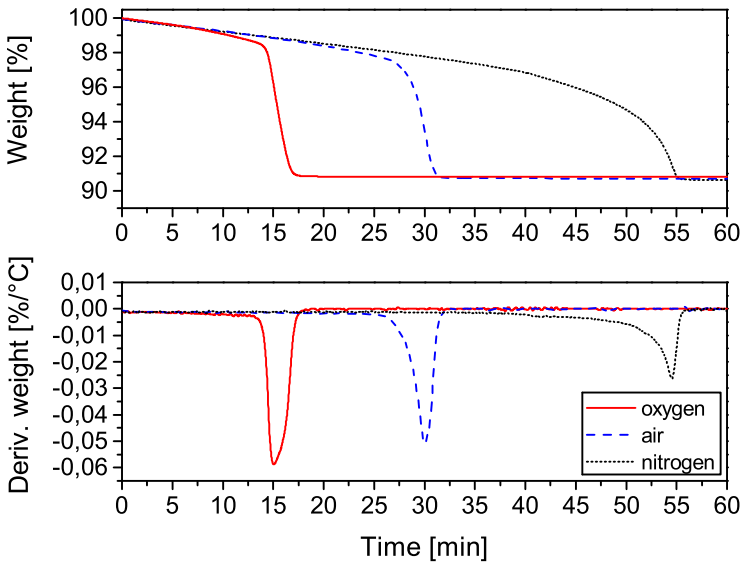

Figure 4.9: Isothermal TGA measurements of C4 Au-nanoparticles performed under oxygen (red line), synthetic air (blue dashed line) and nitrogen (black dotted line)

4.2.3 Preparation of Conductive Au-Nanoparticle Films

For the preparation of Au-nanoparticle thin films, it is of particular importance to achieve homogeneous, aggregate-free layers. tC4, as well as PPh3 Au-nanoparticles were therefore not further regarded for the fabrication of thin films, due to aggregation of the particles and a generally poor dispersibility. C4, C12 and C18 particles, in contrast exhibit a better dispersibility, leading to uniform thin films. From these Au-nanoparticles, 1-butanethiol stabilized particles are the most promising candidate due to the comparably low required sintering temperature.

To determine the resulting film thickness before and after sintering of Au-nanoparticle thin films, nanoparticle dispersions with varying concentrations were spin coated onto glass slides ($v = 1000\,\mathrm{rpm}$, $a = 1000\,\mathrm{rpm/s}$). A thermal treatment at a temperature of 280 °C for a duration of 10 minutes was chosen in order to guarantee a complete sintering of the films. Figure 4.10 reveals the resulting film thickness before and after the sintering step, determined by means of profilometry. As expected, a linear increase of the resulting film thickness is observed for higher nanoparticle concentrations, with values lying between $12 \pm 2\,\mathrm{nm}$ for $10\,\mathrm{mg/ml}$ nanoparticle dispersions and $132 \pm 15\,\mathrm{nm}$ for $100\,\mathrm{mg/ml}$ dispersions. After sintering, the film thickness is reduced significantly due to the removal of the stabilizing ligands and a

reordering of the nanoparticle thin films. For 100 mg/ml Au-nanoparticle dispersions, a reduction of the film thickness of approximately 62% was determined.

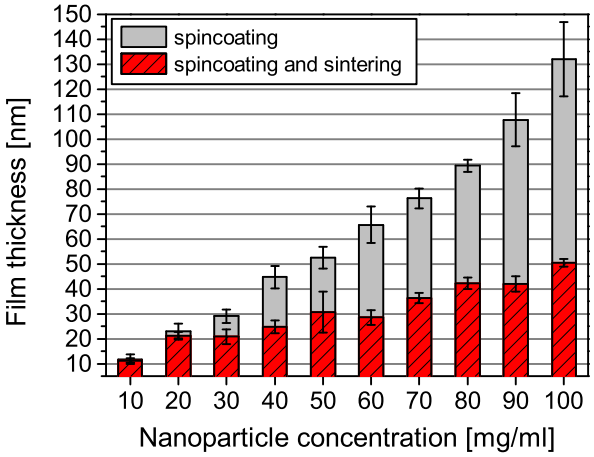

Figure 4.10: Thickness of C4 Au-nanoparticle films, fabricated by spin coating from dispersions with varying nanoparticle contents before (grey solid bars) and after sintering (red striped bars)

The sheet resistivity of these layers was measured with a four-point probe setup. Table 4.2 lists the film thickness, determined by means of profilometry, as well as the calculated sheet resistivity of the C4 Au-nanoparticle films, prepared from dispersions in chloroform with different nanoparticle concentrations (c_{AuNP}). It was found, that a film thickness of approximately 29 nm ($c_{AuNP} = 50$ to 60 mg/ml) of the sintered Au-nanoparticle layers is sufficient to achieve electrical conductivity. The measured values for the film thickness showed notable variations due to an inhomogeneity of the spin coated films. Therefore, an exact correlation of the film thickness with the sheet resistivity can not be made. The lowest determined value of 2.61 Ω/sq for 50 nm thin films, however, lies in the range of evaporated metal layers and are well suited for conductive thin films or for the application as electrodes.[124]

An evaluation of the electrical conductivity of such spin coated layers as a function of the temperature was additionally performed to determine a suitable sintering temperature. Therefore, the current between two point probes, with a distance of approximately 4 mm was determined as a function of the temperature. For these experiments, C4 Au-nanoparticle films were prepared by spin coating onto glass substrates ($c = 100$ mg/ml, $v = 800$ rpm, $a = 1000$ rpm/s). Figure 4.11 shows the resulting resistance curves of the C4 Au-nanoparticle films during heating with a constant rate of 10 °C/min. A slow decrease of the resistance can be observed at

Table 4.2: Film thickness and sheet resistivity of spin coated and sintered C4 Au-nanoparticle films

c_{AuNP} [mg/ml]	Film thickness [nm]	Sheet resistivity [Ω/sq]
50	31 ± 8	9.87
60	29 ± 3	14.73
70	36 ± 2	8.60
80	42 ± 2	3.22
90	42 ± 3	7.80
100	50 ± 2	2.61

the beginning of the heating process, with a sharp decline at 178 °C, leading to an electrically conductive film. A second sample was heated to 150 °C at a rate of 10 °C/min and the temperature was kept constant for 40 minutes to demonstrate, that such conductive Au-nanoparticle thin films can also be fabricated by sintering at 150 °C. The resulting resistance curve is plotted in Figure 4.11b and exhibits a slower decline of the resistance over time with multiple sharp transitions. The main decrease of the resistance is observed after a thermal treatment for approximately 15 minutes. After a sintering duration of 30 minutes, no further significant changes are observed, which is in good accordance to the previously conducted TGA measurements.

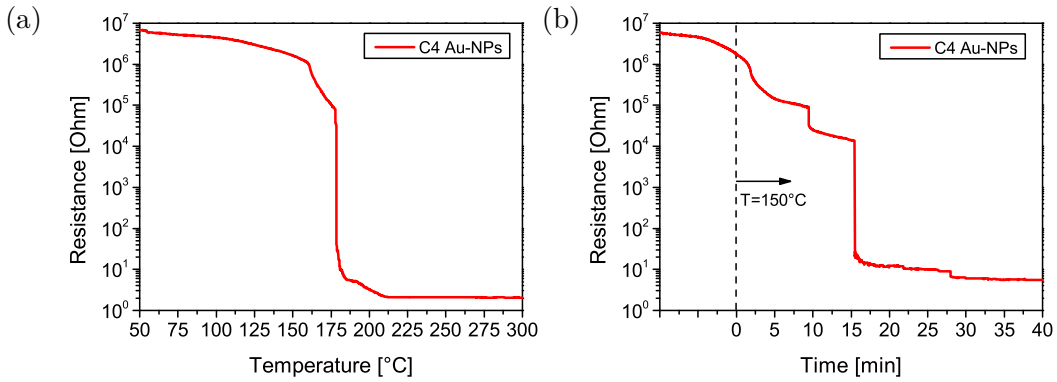

Figure 4.11: Resistance curves of C4 Au-nanoparticles under heating from room temperature to 300 °C (a) and under isothermal heating at 150 °C (b)

4.2.4 Photo-Induced Crosslinking of Au-Nanoparticles

Various approaches have been made previously to achieve a photolithographic patterning of stabilized Au-nanoparticle films. Sun et al. utilized a UV-laser in combination with near-field scanning optical microscopy (NSOM) to accomplish a photo-oxidation

of the stabilizing ligands.[132] Although this approach yields nanoparticle-patterns with high resolutions, it is not feasible for high-throughput fabrication due to the high energy input required and elaborate experiment setup. Huh and Subramani et al. utilized crosslinking of the stabilizing ligands via dimerization or charge reversal reactions.[133,134] Photopatterning of these materials with resolutions in the micrometre-range is possible, however, only a low conductivity of the generated Au-nanoparticle patterns was achieved. Thus, an additional sintering step would be needed in order to achieve sufficient conductivity. Due to the expected high thermal stability of the described stabilizing ligands, this step most likely requires temperatures, which are no longer compatible with polymer substrates. Therefore, the combination of high-resolution photolithographic patterning and low sintering temperatures is of particular interest for the application of Au-nanoparticles in organic electronics.

Photo-induced crosslinking of the ligands of 1-butanethiol stabilized Au-nanoparticles was utilized to achieve a lateral patterning of spin coated Au-nanoparticle films. Small amounts (1–10 wt%) of 2,6-bis(4-azidobenzylidene)-4-methylcyclohexanone (BAC-M) were used as a crosslinking agent and were added to the nanoparticle dispersion prior to spin coating. The UV-irradiation of BAC-M at a wavelength of $\lambda = 365\,\text{nm}$ leads to the generation of nitrene radicals which can subsequently react with the nanoparticle ligands, by a C–H bond insertion, or by hydrogen abstraction from CH_2 groups, leaving free radicals which terminate by coupling reactions, leading to an insoluble nanoparticle network. The UV-illumination has to be performed under inert atmosphere in order to prevent unwanted reactions of the photo-generated nitrene radicals with ambient oxygen and to achieve crosslinking of the stabilizing ligands. After a subsequent sintering step at a suitable temperature, laterally patterned conductive features can therefore be achieved. A schematic illustration of the photopatterning process is depicted in Figure 4.12.

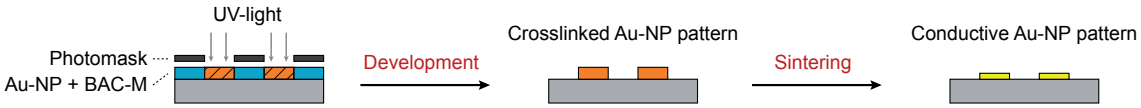

Figure 4.12: Photopatterning process of thiol stabilized Au-nanoparticles with BAC-M

For the evaluation of suitable bisazide concentrations for photolithographic patterning, Au-nanoparticle films with varying amounts of BAC-M were prepared from chloroform dispersions by means of spin coating ($c = 20\,\mathrm{mg/ml}$, $v = 1000\,\mathrm{rpm}$, $a = 1000\,\mathrm{rpm/s}$). These layers were subsequently illuminated under nitrogen atmosphere using a simple quartz-chromium shadow mask with an irradiation dose of $12.1\,\mathrm{J/cm^2}$. Figure 4.13 shows the resulting patterns after a development in chloroform for 10 minutes. It can be observed, that increasing BAC-M concentrations lead to less well defined patterns with increasingly blurred features. BAC-M concentrations of 10 wt% and above lead to a crystallization of the bisazide component and are not suitable for photopatterning. However, line patterns could still be observed. Therefore, for all further photopatterning experiments, BAC-M concentrations between 3 and 5 wt% were used.

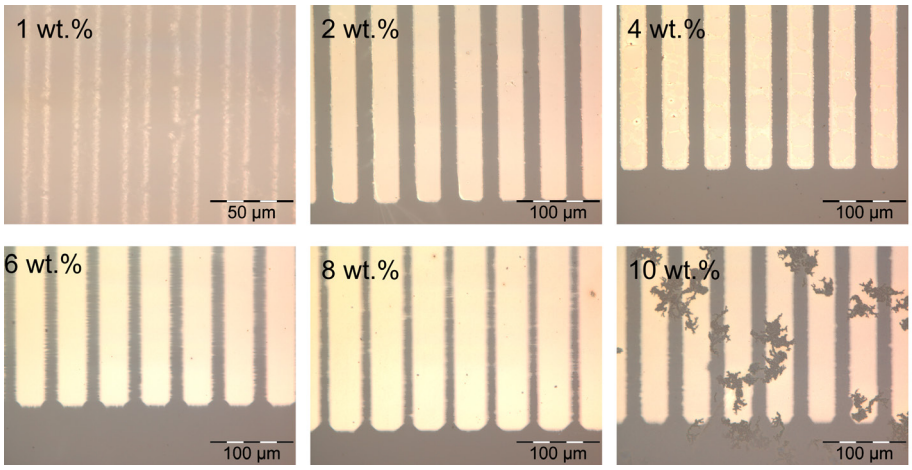

Figure 4.13: C4 Au-nanoparticle films, containing different amounts of BAC-M after photolithographic patterning

SEM micrographs of these photopatterned Au-nanoparticle films, containing 5 wt% BAC-M after UV-irradiation with a dose of $12.1\,\mathrm{J/cm^2}$, are shown in Figure 4.14. The resulting line patterns exhibit a porous surface with blurred edges which may be caused by scattering of the UV light due to the porosity of the nanoparticle layers. The achievable resolution lies in the range of several micrometres which is nonetheless suitable for various electrode applications.

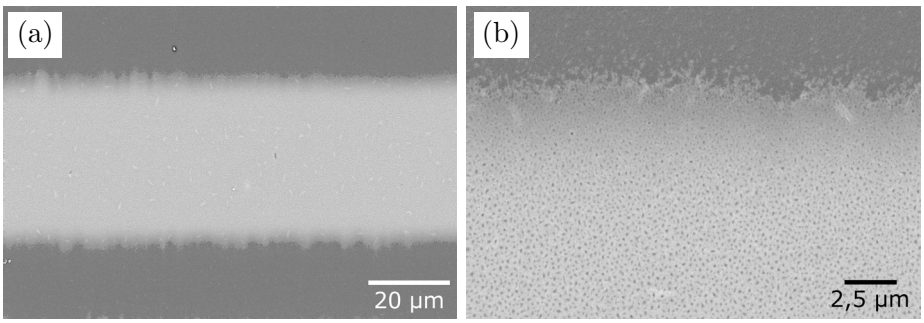

Figure 4.14: Backscattered secondary electron images of a photopatterned Au-nanoparticle film, containing 5 wt% BAC-M

The porosity of these layers was further investigated by means of SEM and the influence of the photopatterning process on the surface properties was compared. Figure 4.15 depicts SEM micrographs of Au-nanoparticle layers, containing 5 wt% BAC-M before and after UV-illumination with a dose of 12.1 J/cm^2, as well as after subsequent development in chloroform. In these images, a porosity of the fabricated Au-nanoparticle layers can be observed after each processing step with no clear influence of the individual steps.

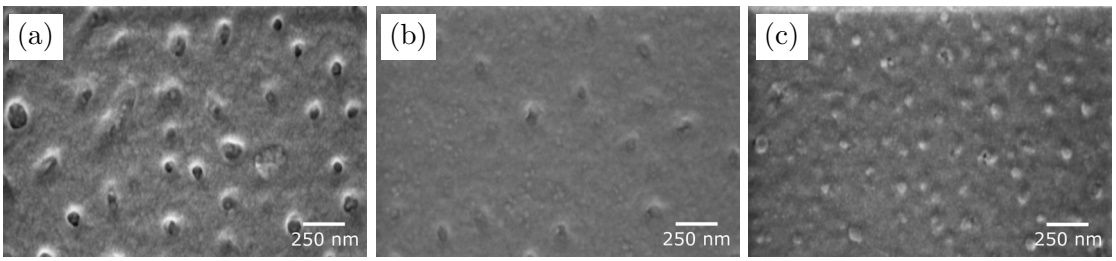

Figure 4.15: Secondary electron images of Au-nanoparticle layers, containing 5 wt% BAC-M, before illumination (a), after illumination (b) and after illumination and development (c)

In order to determine a suitable irradiation dose for a complete crosslinking, Au-nanoparticle films containing 5 wt% BAC-M were spin coated and illuminated with polychromatic UV-light with varying irradiation doses. After a development in chloroform, the remaining film thickness of the crosslinked films was determined by means of profilometry. The resulting curve in Figure 4.16 reveals an increase of the film thickness under UV-illumination with irradiation doses up to 9.7 J/cm^2, with no further significant changes at higher doses. From these measurements, it can be concluded that a formation of a loose nanoparticle network takes place, influencing the film thickness of the resulting films after development.

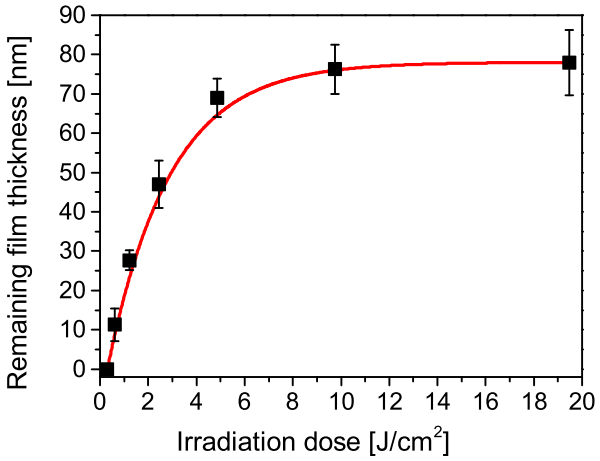

Figure 4.16: Remaining film thickness of photopatterned C4 Au-nanoparticle films after development as a function of the irradiation dose

The comparably high irradiation dose needed for a complete crosslinking can be explained by a non-ideal overlap between the emission of the UV-source and the absorption of BAC-M. The measured emission- and absorption spectra are given in Figure 4.17. BAC-M exhibits a local maximum of absorption at $\lambda = 360\,\text{nm}$, therefore also allowing the use of monochromatic light sources for a better overlap and shorter irradiation-time, required for crosslinking.

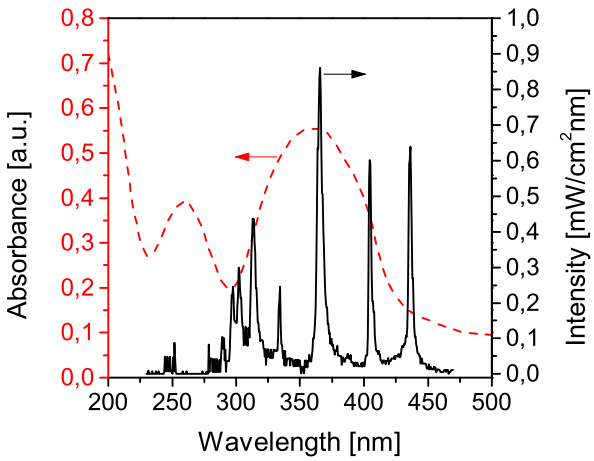

Figure 4.17: Absorption spectrum of BAC-M (red dashed line) and emission spectrum of the used polychromatic UV-source

4.2.5 Contact Lithography

Photolithographic patterning on a mask-aligner was furthermore performed to achieve patterns with lateral resolutions in the low micrometre-range. Spin coated Au-NP films ($c = 20\,\mathrm{mg/ml}$, $v = 1000\,\mathrm{rpm}$, $a = 1000\,\mathrm{rpm/s}$), containing 5 wt% BAC-M were illuminated on a mask-aligner system in hard contact mode through a quartz-chromium mask and were subsequently developed in chloroform. The resulting features were investigated by means of optical microscopy and scanning electron microscopy and exhibit resolutions in the single digit micrometre-range. The SEM micrographs in Figure 4.18 show the resulting structures, also exhibiting a porous surface of the material after UV-illumination and development. Furthermore, the resulting line patterns exhibit blurred edges, nonetheless allowing resolutions in the range of 3 to 4 µm.

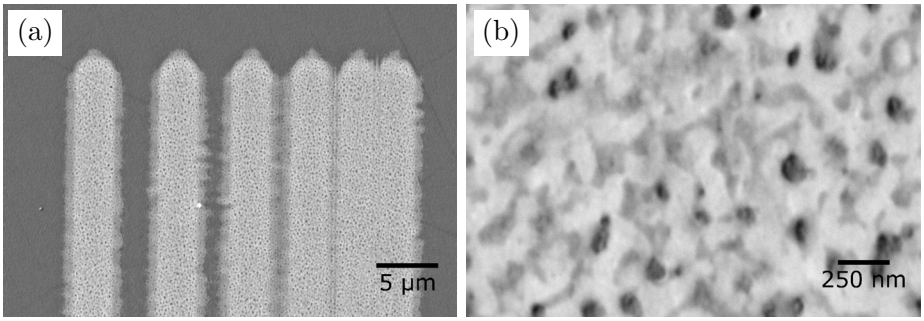

Figure 4.18: Backscattered secondary electron images of C4 Au-nanoparticle films after photolithographic patterning on a mask-aligner

In order to improve the achievable resolution of the material, the BAC-M-content was decreased to 3 wt%, resulting in uniform films with fewer impurities. Development was furthermore done in toluene for 10 to 15 minutes to avoid negative influences, which may be caused by a strong swelling of the crosslinked film. The adhesion of the resulting photopatterned layers to glass substrates was also verified by a simple scotch-tape test. The crosslinked nanoparticle layers showed a good adhesion to glass substrates and silicon wafers and were not pulled off by the tape when it was removed, providing a clear advantage to conventional evaporated gold layers.

As previously mentioned, the sintering process leads to a decrease of the film thickness of the Au-nanoparticle films. The height of crosslinked features, fabricated by means of spin coating ($c = 100\,\mathrm{mg/ml}$, $v = 800\,\mathrm{rpm}$, $a = 1000\,\mathrm{rpm/s}$) and photopatterning on a mask aligner, was determined by means of AFM measurements before and after sintering on a hotplate. In Figure 4.19, an AFM micrograph and the

corresponding height profile of a single photopatterned line is depicted, exhibiting an average height of $49 \pm 1.8\,\text{nm}$.

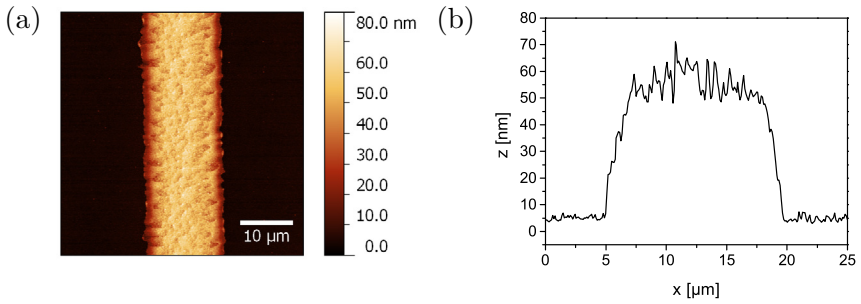

Figure 4.19: AFM micrograph (a) and line profile (b) of photopatterned Au-nanoparticles

After sintering at 280 °C for 10 minutes, a significant decrease of the feature height to $26 \pm 1.4\,\text{nm}$ was measured, corresponding to a decrease of the film thickness of 53%. An AFM micrograph and height profile of a sintered line is shown in Figure 4.20a-b. The resulting sintered Au-nanoparticle patterns show homogeneous surfaces with a rms-roughness of $R_q = 6.8\,\text{nm}$ after sintering, as depicted in the detailed AFM image and line-roughness profile in Figure 4.20c.

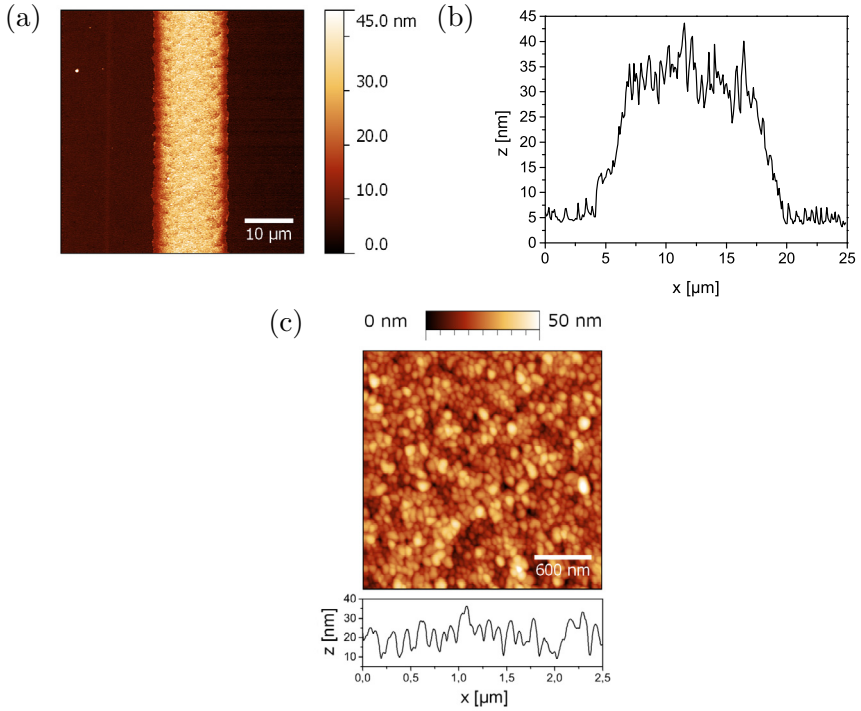

Figure 4.20: AFM micrograph (a) and line profile (b) of photopatterned Au-nanoparticles after sintering. A detailed AFM scan and line roughness profile is depicted in (c)

To further demonstrate the suitability of these photopatterned Au-nanoparticle films with a variety of surfaces, including flexible substrates, C4 Au-nanoparticle layers with 3 wt% BAC-M were prepared on PET films (Melinex ST725) and photopatterned on a mask-aligner. The resulting patterns show resolutions in the range of 1 to 2 µm (see Figure 4.21), also providing good adhesion to the polymer substrate. The adhesion of the crosslinked patterns was additionally verified by a scotch-tape test, in which the patterns were not pulled off by the tape. These advantageous properties illustrate the potential of such photopatternable films for flexible organic electronic devices.

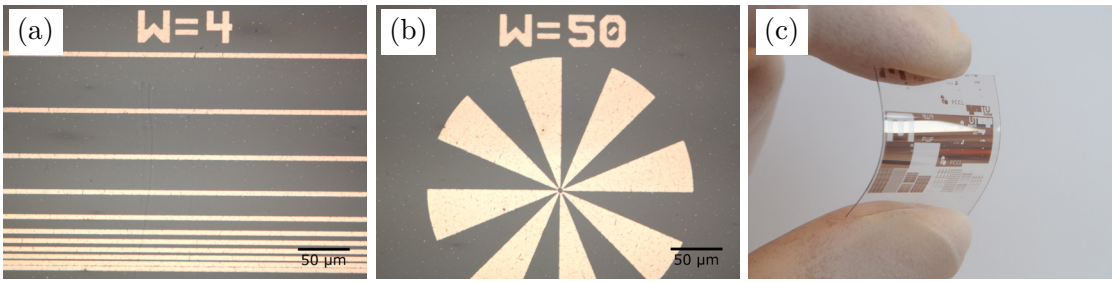

Figure 4.21: Optical micrographs (a,b) and photograph (c) of photopatterned C4 Au-nanoparticle layers on PET

4.2.6 Fabrication of Conductive Au-Nanoparticle Patterns

In order to monitor the sintering process of crosslinked Au-nanoparticle layers, such films containing 3 wt% BAC-M were spin coated onto glass slides and crosslinked by flood illumination on a medium pressure Hg lamp. After a development in toluene, the samples were heated from room temperature to 300 °C at a heating rate of 10 °C/min. The current between two point probes with a distance of approximately 4 mm was determined as a function of the temperature. Due to the photo-induced cross linking of the nanoparticles, higher temperatures are needed to remove the stabilizing ligands and to achieve sintering of the nanoparticle films. In Figure 4.22, the measured resistance is plotted as a function of the temperature, revealing a sharp decline at 272 °C with an onset of the decline at approximately 240 °C. The corresponding resistance curve for sintering at 240 °C is plotted in Figure 4.22b. In this experiment, the sample was heated to 240 °C at a rate of 10 °C/min and the temperature was then kept constant, leading to a complete sintering of these Au-nanoparticle films after approximately 35 minutes, demonstrating that also crosslinked Au-nanoparticle

films can be sintered at moderate temperatures. Four-point probe measurements of the sintered films further revealed a sheet resistivity of 2.31 Ω/sq, corresponding to a bulk resistivity of 8.03×10^{-8} Ω/m for the 35 nm thin films, which is suitable for the application as an electrode material.

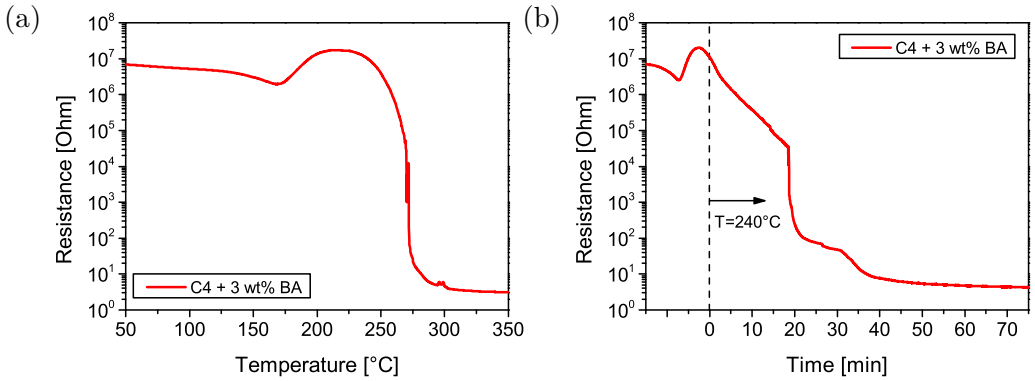

Figure 4.22: Resistance curves of photolithographically patterned C4 Au-nanoparticles under heating from room temperature to 350 °C (a) and under isothermal heating at 240 °C (b)

4.2.7 Holographic Lithography

Laser interference lithography was furthermore used as a tool to achieve large-area patterns with high resolutions. Thin Au-nanoparticle films, containing 5 wt% of BAC-M, were spin coated onto glass substrates from chloroform dispersions. After UV-illumination under nitrogen atmosphere, the films were developed in chloroform, leading to a removal of the non-irradiated areas and to crosslinked Au-nanoparticle line patterns with a pitch of approximately 1.46 µm. The height of these structures was measured by means of AFM and was determined as 30 to 40 nm. The crosslinked patterns, visible in the AFM image in Figure 4.23, however, exhibited a poor adhesion to the substrate and were poorly defined, in contrast to patterns achieved by contact lithography. The bright areas, visible in the bottom right corner of the image, are most likely due to a folding of crosslinked areas, which are partially detached from substrate. Nonetheless, photopatterning by means of holographic lithography is possible with this material, enabling advanced applications in optics and organic electronics.

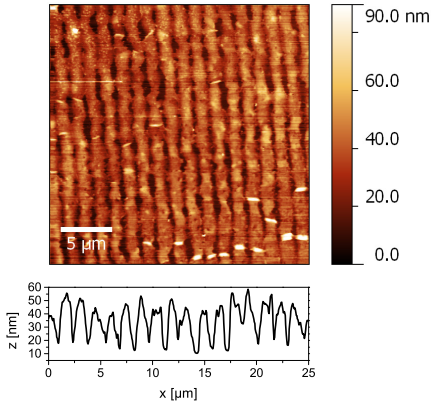

Figure 4.23: AFM micrograph and corresponding line profile of a C4 Au-nanoparticle film after holographic lithography

4.2.8 Application as OTFT Source/Drain Electrodes

To highlight the application of this photopatternable material in organic electronics, photopatterned Au-nanoparticle films were investigated as source/drain electrodes in pentacene based OTFTs. By utilizing the described photopatterning method, it was possible to fabricate OTFTs in a bottom-gate coplanar architecture, as illustrated in Figure 4.24. The OTFT channels were fabricated by UV-illumination and development of spin coated Au-nanoparticle films through a metal shadow mask, resulting in a channel length of approximately 10 µm.

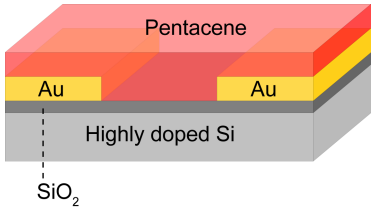

Figure 4.24: Device architecture of OTFTs with photo-regenerated Au-nanoparticle source/drain electrodes

The electrical characteristics of the fabricated devices are plotted in Figure 4.25. These OTFTs show a saturation of the drain current and a quadratic increase of the saturation drain current level with the gate bias. Moreover, an onset voltage $V_{on} = 1.7\,\mathrm{V}$, a sub-threshold swing of 1.2 V/dec and a threshold voltage $V_{thr} = -2.5\,\mathrm{V}$ were determined. The comparably low charge carrier mobility in the range of $3 \times 10^{-3}\,\mathrm{cm^2/V\,s}$ can be explained by a small-grain semiconductor growth with 300–700 nm grains in the transistor channel.

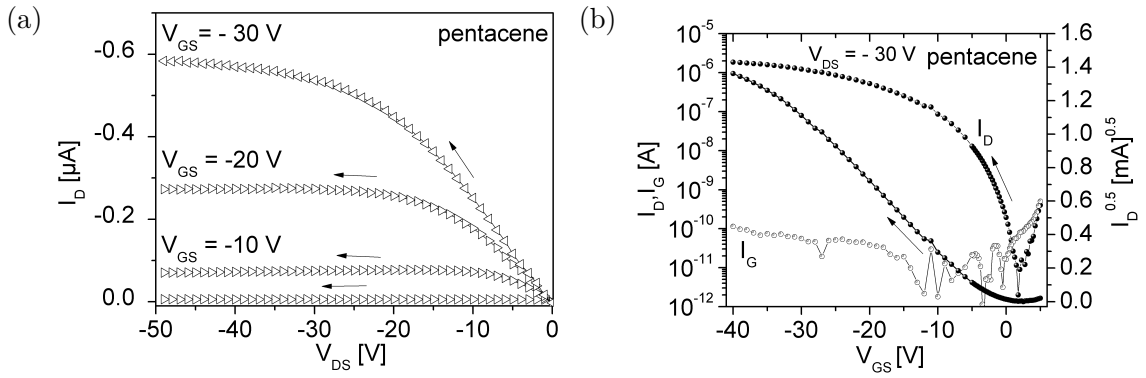

Figure 4.25: Output characteristics (a) and transfer characteristics (b) of pentacene-based OTFTs with photopatterned Au-nanoparticle source/drain electrodes with a channel width of 4 mm and a channel length of 10 µm. The gate leakage current characteristics I_G (V_{GS} is additionally displayed. Work done by Andreas Petritz

UV-photoelectron spectroscopy (UPS) measurements further revealed a work function of -4.55 eV for the Au-nanoparticle–pentacene contact, whereas evaporated gold exhibits a work function -4.9 eV, matching the HOMO level of pentacene at −5.0 eV. However, patterning of the evaporated Au contacts with conventional photolithography usually leads to a lower work function in the range of -4.2 eV. This reduction is due to residuals stemming from the photolithography process and can be ascribed to contaminations from the photoresist, developer or solvents.

The described photopatterned Au-nanoparticle electrodes, therefore, result in a higher quality contact with pentacene and a better energy–level alignment compared to conventional photolithographically patterned Au contacts. This behaviour is highly favourable for the fabrication of bottom-contact OTFT devices, considering that no further extensive cleaning or surface treatment steps of the Au-electrodes are necessary after photolithographic patterning. [107]

4.3 Experimental

4.3.1 Materials

Unless otherwise stated, all chemicals were obtained from commercial sources and were used without further purification. Table 4.3 lists all used chemicals, as well as their respective source and purity.

Table 4.3: List of used chemicals (3)

Substance	**Supplier**	**Purity**
2,6-Bis(4-azidobenzylidene)-4-methylcyclohexanone	Sigma Aldrich	97%
1-Butanethiol	Sigma Aldrich	99%
Chloroform	Roth	$\geq$ 99%
1-Dodecanethiol	Sigma Aldrich	$\geq$ 98%
Ethanol	Roth	$\geq$ 99.8%
Heptane	Roth	$\geq$ 99%
Hydrogen tetrachloroaurate(III) trihydrate	Alfa Aesar	99.99%
Methanol	Roth	$\geq$ 99.5%
2-Methyl-2-propanethiol	Sigma Aldrich	99%
1-Octadecanethiol	Sigma Aldrich	98%
Sodium borohydride	Sigma Aldrich	99%
Tetraoctylammonium bromide	Sigma Aldrich	98%
Toluene	Roth	$\geq$ 99.5%
Triphenylphosphane	Sigma Aldrich	$\geq$ 98.5%

4.3.2 Methods

Sample Preparation

Au-nanoparticle thin films were fabricated by spin coating from chloroform dispersions with concentrations ranging from $c = 10$ to $150\,\mathrm{mg/ml}$ ($v = 800$ to $1000\,\mathrm{rpm}$, $a = 1000\,\mathrm{rpm/s}$) onto different substrates. For photopatterning experiments, varying amounts of 2,6-bis(4-azidobenzylidene)-4-methylcyclohexanone were added to the nanoparticle dispersions prior to spin coating.

UV- and Visible Light (UV/Vis) Spectroscopy

UV/Vis spectra were recorded on a Varian Cary 50 UV/Vis spectrometer in absorbance mode on CaF_2 plates or alternatively in chloroform solution. The obtained spectra were evaluated, using the software Cary WinUV 3.00.

Thermogravimetric Analysis (TGA)

Thermogravimetric analysis was performed on a Mettler Toledo TGA/DSC 1 instrument with a gas flow of 30 ml min^{-1} and a heating rate of 10 K min^{-1}, using either nitrogen, synthetic air or oxygen for analysis. The software STARe 11.00a was used for the evaluation of the recorded curves.

Atomic Force Microscopy (AFM)

AFM micrographs were recorded with a Nanosurf FlexAFM instrument, using silicon AFM probes with a resonance frequency of 190 kHz and a force constant of 48 N m^{-1} (Tap190AL-G, Budgetsensors) in tapping mode. Evaluation of the recorded AFM images was done, using the software Gwyddion 2.32.

Profilometry

The film thickness of the samples was measured by means of contact stylus profilometry (VEECO Dektak 150 stylus profiler).

Transmission Electron Microscopy (TEM)

TEM measurements were performed at the Erich Schmid Institute of Materials Science, Leoben by Dr. Zaoli Zhang on a JEOL JEM-2100F instrument. Particle size and size-distributions were determined with the software ImageJ 1.47i.

Scanning Electron Microscopy (SEM)

SEM measurements were performed at the Materials Center Leoben by Bernhard Sartory on a cross-beam electron microscope (Zeiss Auriga CrossBeam workstation) with varying acceleration voltage and working distance.

UV-Irradiation

Unless otherwise stated, UV-irradiation was carried out under nitrogen atmosphere. The light intensity (power density) at the sample surface was measured with a spectroradiometer (Solatell, Sola Scope 2000) in the wavelength range of 230–470 nm. The following light sources and their intensity are listed in Table 4.4.

Photolithographic patterning was carried out with a mask-aligner (SUSS, MJB4, 500 W HgXe) with a measured power density of 21.3 mW/cm^2.

Table 4.4: List of used UV-sources (2)

UV-source	**Intensity [mW/cm^2]**
Newport 66990	20.17
Heraeus Noblelight GPH212T5L	0.18

Device Fabrication and Characterization

A highly doped Si-Wafer was used as the gate electrode (substrate) with a 100 nm thick SiO_2 layer as the gate dielectric. Photopatterned Au-nanoparticle layers were used as source and drain electrodes. A 35 nm thick pentacene layer was evaporated onto the preheated samples at 65 °C in high vacuum at a rate of 0.1 nm/min for the first 5 nm and 0.6 nm/min for the remaining 45 nm. After fabrication, all OTFT samples were protected from light and stored under argon atmosphere. The channel lengths of the fabricated OTFTs was 10 µm and the channel width ranged from 1 to 4 mm. Electrical measurements are carried out under exclusion of light under ambient conditions, using a parametric analyser from mb-Technologies.

4.3.3 Synthesis of Alkanethiol Stabilized Au-Nanoparticles

$$AuCl_4^-(aq) + N(C_8H_{17})_4^+(C_6H_5Me) \longrightarrow N(C_8H_{17})_4^+AuCl_4^-(C_6H_5Me)$$

$$m\,AuCl_4^-(C_6H_5Me) + n\,RSH(C_6H_5Me) + 3\,m\,e^- \longrightarrow 4\,m\,Cl^-(aq) + (Au_m)(RSH)_n(C_6H_5Me)$$

Figure 4.26: Synthesis of thiol stabilized Au-nanoparticles[135]

One equivalent of $HAuCl_4.3\,H_2O$ was dissolved in H_2O (30 mmol/l, yellow solution) and tetraoctylammonium bromide in toluene (1.5 eq, 50 mmol/l) was added under stirring. The colour of the organic phase changed to dark red–brown. The mixture was stirred for 30 minutes at room temperature. the organic phase was separated and the respective alkanethiol ($\chi_{SH/Au} = 2$) was added under vigorous stirring. After 10 minutes, $NaBH_4$ (10 eq) in H_2O (40 mmol/l) was added and the solution was stirred for further 3 hours. The colour of the organic phase changed to dark brown. The organic phase was then isolated and reduced to approximately 10 ml on a rotary evaporator (50 °C, 90 mbar) and precipitated in cold ethanol (2×). The precipitate was centrifuged and dried *in vacuo* at 40 °C for 2 hours. Table 4.5 states the inserted amounts of reactants and yields of the separate synthesis procedures.

Table 4.5: Amount of reactants for the synthesis of alkanethiol stabilized Au-nanoparticles

Ligand	**$HAuCl_4$ [mg]**	**Thiol [mg]**	**Yield [mg]**
2-Methyl-2-propanethiol (tC4)	505.7	57.9	238
1-Butanethiol (C4)	500	57.25	240
1-Dodecanethiol (C12)	300	89.35	151
1-Octadecanethiol (C18)	200	84.34	161

4.3.4 Synthesis of Triphenylphosphane Stabilized Au-Nanoparticles

The synthesis of triphenylphosphane stabilized Au-nanoparticles was performed in analogy to the procedure described in Figure 4.26. 200 mg of $HAuCl_4 . 3\,H_2O$ were dissolved in H_2O (30 mmol/l) and tetraoctylammonium bromide in toluene (50 mmol/l) was added under stirring. After 30 minutes, 463.2 mg of triphenylphosphane were added and after further 10 minutes of stirring, 222.7 mg $NaBH_4$ were added. The organic phase was isolated and reduced to approximately 10 ml on a rotary evaporator (50 °C, 90 mbar) and precipitated in heptane (2×). The precipitate was centrifuged and dried *in vacuo* at 40 °C for 2 hours.

Yield: 345 mg of a black solid.

4.4 Summary and Conclusions

Gold nanoparticles stabilized with *tert*-butylthiol (tC4), 1-butanethiol (C4), 1-dodecanethiol (C12), 1-octadecanethiol (C18) and triphenylphosphane (PPh3) were synthesized and characterized. Transmission electron microscopy (TEM) measurements of these particles showed similar particle shapes and sizes with diameters in the range of 2–5 nm for C4, C12 and C18 Au-nanoparticles and more irregular size distribution of the tC4 and PPh3 particles. PPh3 Au-nanoparticles exhibited larger aggregates with diameters of 10–20 nm, as well as smaller particles with diameters in the range of 2–3 nm. tC4 particles also showed a heterogeneous particle size distribution with cluster sizes ranging from 2–20 nm in diameter.

Thermogravimetric analysis (TGA) of the different Au-nanoparticles revealed a characteristic weight loss with generally higher onset temperatures at an increasing chain length of alkanethiol stabilized particles. The onset temperatures of the alkanethiol stabilized particles was observed in the range of 139 to 292 °C, whereas triphenylphosphane stabilized Au-nanoparticles show an onset of the main mass loss at 282 °C. The total mass loss corresponds well with the organic content of the stabilizing ligands, with differential thermogravimetry (DTG) peak temperatures in the range of 152–330 °C for alkanethiol stabilized Au-nanoparticles and at 316 °C for triphenylphosphane stabilized particles.

In order to determine the influence of oxygen on the destabilization of C4 Au-nanoparticles, isothermal TGA measurements were performed at 150 °C, using different atmospheres for measurement. The respective DTG peak of the main mass loss occurs after a duration of 55 minutes under nitrogen atmosphere and decreases significantly to 30 minutes in synthetic air and to 15 minutes in oxygen, respectively.

C4 Au-nanoparticle films with a thickness of 12–132 nm were prepared and sintered at 280 °C, leading to a significant reduction of the film thickness up to 62% of the original thickness. A sheet resistivity of 2.61 Ω/sq for 50 nm thin layers was measured after sintering of the Au-nanoparticle layers. An evaluation of the electrical conductivity of such layers as a function of the temperature was additionally performed, showing a sharp decline of the resistance at 178 °C, leading to electrically conductive films. When sintering such layers at 150 °C, electrical conductivity is achieved after approximately 15 minutes of thermal treatment.

The photo-induced crosslinking of the ligands of C4 Au-nanoparticles with 1–10 wt% of 2,6-bis(4-azidobenzylidene)-4-methylcyclohexanone as a crosslinking agent, was

further investigated. Under UV-illumination with irradiation doses up to 9.7 J/cm^2, the formation of an insoluble network was observed with no further significant changes at higher doses. Photolithographic patterning on a mask-aligner resulted in Au-nanoparticle patterns with resolutions in the range of 3–4 µm. Such layers were additionally prepared on flexible substrates, showing similar properties with resolutions in the range of 1–2 µm and a good adhesion to the substrate. Laser interference lithography was additionally used as a tool to achieve large-area patterns with high resolutions, leading to Au-nanoparticle structures with a pitch of approximately 1.46 µm and a height of 30–40 nm.

In order to monitor the sintering process of crosslinked Au-nanoparticle layers, such films were heated and the current flow between two point probes was measured. A sharp decline of the resistance at 272 °C with an onset at approximately 240 °C was observed. Sintering at 240 °C also leads to conductive layers after approximately 35 minutes. Four-point probe measurements of the sintered films revealed a sheet resistivity of 2.31 Ω/sq, corresponding to a bulk resistivity of 8.03×10^{-8} Ω/m for 35 nm thin films.

To demonstrate the potential of this material for applications in organic electronics, photopatterned Au-nanoparticle films were investigated as source- and drain electrodes in pentacene based OTFTs. The OTFT channels were fabricated by photolithographic patterning of spin coated Au-nanoparticle films through a shadow mask, resulting in channel lengths in the range of 10 µm. These OTFTs showed an onset voltage V_{on} of 1.7 V, a sub-threshold swing of 1.2 V/dec and a threshold voltage V_T of -2.5 V. A charge carrier mobility of these devices in the range of 3×10^{-3} cm^2/V s was measured. UV-photoelectron spectroscopy (UPS) measurements revealed a work function of -4.55 eV for the Au-nanoparticle–pentacene contact, suggesting a good energy–level alignment.

The described photopatterning method enables an efficient fabrication of electrically conductive structures with resolutions in the µm range, utilizing solution-based processing techniques, which are compatible with flexible polymer substrates having comparatively low temperature resistance. The moderate required temperatures and the good adhesion of the resulting structures to a variety of substrates, allows the realisation of a wide range of components for electronic and optical appliances.

List of Used Abbreviations

AFM	Atomic force microscopy
BAC-M	2,6-Bis(4-azidobenzylidene)-4-methylcyclohexanone
CNT	Carbon nanotubes
DTG	Differential thermogravimetry
FET	Field-effect transistor
FTIR	Fourier-transform infrared
GPC	Gel permeation chromatography
HOMO	Highest occupied molecular orbital
ISC	Intersystem crossing
ITO	Indium tin oxide
LUMO	Lowest unoccupied molecular orbital
MEM	Microelectromechanical system
NB	Bicyclo[2.2.1]hept-2-ene
NDME	(±)*endo,exo*-Bicyclo[2.2.1]hept-5-ene-2,3-dicarboxylic acid dimethyl ester
NDPE	(±)*endo,exo*-Bicyclo[2.2.1]hept-5-ene-2,3-dicarboxylic acid diphenyl ester
NHNT	*N*-Hydroxynaphthalimide triflate
NMR	Nuclear magnetic resonance
NSOM	Near-field scanning optical microscopy
OFET	Organic field-effect transistor
OLED	Organic light emitting diode
OPV	Organic photovoltaics
OTFT	Organic thin film transistor
PAG	Photoacid generator
PEDOT	Poly(3,4-ethylenedioxythiophene)
PET	Polyethylene terephthalate
PSS	Polystyrene sulfonate
RFID	Radio-frequency identification
ROMP	Ring-opening methathesis polymerization
SAM	Self-assembled monolayer
SEM	Scanning electron microscopy
TEM	Transmission electron microscopy
TGA	Thermogravimetric analysis
TLC	Thin layer chromatography
TMSC	Trimethylsilyl cellulose
TPA	Two-photon absorption
UPS	UV-photoelectron spectroscopy
UV	Ultra-violet

List of Figures

List of Tables

Bibliography

[1] H. Shirakawa, E. J. Louis, A. G. MacDiarmid, C. K. Chiang, and A. J. Heeger, *J. Chem. Soc., Chem. Commun.*, p. 578, 1977.

[2] J. H. Burroughes, D. D. C. Bradley, A. R. Brown, R. N. Marks, K. Mackay *et al.*, *Nature*, vol. 347, pp. 539–541, 1990.

[3] C. W. Tang and S. A. van Slyke, *Appl Phys. Lett.*, vol. 51, p. 913, 1987.

[4] A. Tsumura, H. Koezuka, and T. Ando, *Appl Phys. Lett.*, vol. 49, p. 1210, 1986.

[5] H. Koezuka, A. Tsumura, and T. Ando, *Synthetic Met.*, vol. 18, pp. 699–704, 1987.

[6] G. Horowitz, D. Fichou, X. Peng, Z. Xu, and F. Garnier, *Solid State Commun.*, vol. 72, pp. 381–384, 1989.

[7] A. Sazonov, D. Striakhilev, C.-H. Lee, and A. Nathan, *Proc. IEEE*, vol. 93, pp. 1420–1428, 2005.

[8] R. R. Søndergaard, M. Hösel, and F. C. Krebs, *J. Polym. Sci. Polym. Phys.*, vol. 51, pp. 16–34, 2013.

[9] N. Koch, *ChemPhysChem*, vol. 8, pp. 1438–1455, 2007.

[10] E. Cantatore, *Applications of Organic and Printed Electronics: A Technology-enabled Revolution*, ser. Integrated Circuits and Systems. Springer, Boston, 2013.

[11] H. Klauk, *Organic Electronics: Materials, Manufacturing and Applications*. Wiley-VCH, Weinheim, 2006.

[12] T. Grasser, G. Meller, and M. Baldo, *Organic Electronics*, ser. Adv. Polym. Sci. Springer, Heidelberg, 2010, vol. 223.

[13] J. E. Lilienfeld, "Method and apparatus for controlling electric currents," Patent US 1 745 175.

[14] D. Barbe and C. Westgate, *J. Phys. Chem. Solids*, vol. 31, pp. 2679–2687, 1970.

[15] M. L. Petrova and L. D. Rozenshtein, *Fiz. Tverd. Tela (Sov. Phys.-Sol. State)*, vol. 12, pp. 961–962, 1970.

[16] G. Horowitz, *Adv. Mater.*, vol. 10, pp. 365–377, 1998.

[17] S. Brotherton, *Introduction to Thin Film Transistors*. Springer International Publishing, 2013.

[18] M. A. Fox and J. K. Whitesell, *Organische Chemie: Grundlagen, Mechanismen, Bioorganische Anwendungen*, ser. Spektrum-Lehrbuch. Spektrum Akadem. Verl., Heidelberg, 1995.

[19] W. Brütting, *Physics of organic semiconductors*. Wiley-VCH, Weinheim, 2005.

[20] F.-J. M. zu Heringdorf, M. C. Reuter, and R. M. Tromp, *Nature*, vol. 412, pp. 517–520, 2001.

[21] G. Horowitz and M. Hajlaoui, *Synthetic Met.*, vol. 122, pp. 185–189, 2001.

[22] T. W. Kelley, P. F. Baude, C. Gerlach, D. E. Ender, D. Muyres *et al.*, *Chem. Mater.*, vol. 16, pp. 4413–4422, 2004.

[23] D. Gundlach, L. L. Jia, and T. Jackson, *IEEE Electron Device Lett.*, vol. 22, pp. 571–573, 2001.

[24] B. Wardle, *Principles and Applications of Photochemistry*. Wiley, Hoboken, 2009.

[25] M. Montalti and S. L. Murov, *Handbook of Photochemistry*, 3rd ed. CRC/Taylor & Francis, Boca Raton, 2006.

[26] J. Kagan, *Organic Photochemistry: Principles and Applications*. Academic Press, London, 1993.

[27] W. Schnabel, *Polymers and Light: Fundamentals and Technical Applications*. Wiley-VCH, Weinheim, 2007.

[28] S. Bräse and K. Banert, *Organic Azides: Syntheses and Applications*. John Wiley, Chichester, 2010.

[29] S. Bräse, C. Gil, K. Knepper, and V. Zimmermann, *Angew. Chem. Int. Ed.*, vol. 44, pp. 5188–5240, 2005.

[30] K. Fries and G. Finck, *Ber. Dtsch. Chem. Ges.*, vol. 41, pp. 4271–4284, 1908.

[31] J. Anderson and C. Reese, *P. Chem. Soc. London*, p. 217, 1960.

[32] H. Kobsa, *J. Org. Chem.*, vol. 27, pp. 2293–2298, 1962.

[33] R. Finnegan and J. Mattice, *Tetrahedron*, vol. 21, pp. 1015–1026, 1965.

[34] H.-I. Joschek and S. I. Miller, *J. Am. Chem. Soc.*, vol. 88, pp. 3269–3272, 1966.

[35] J. M. J. Frechet, T. G. Tessier, C. G. Willson, and H. Ito, *Macromolecules*, vol. 18, pp. 317–321, 1985.

[36] M. Shirai, W.-G. Ma, and M. Tsunooka, *Eur. Polym. J.*, vol. 29, pp. 913–918, 1993.

[37] K. H. Chae, G. J. Sun, J. K. Kang, and T. H. Kim, *J. Appl. Polym. Sci.*, vol. 86, pp. 1172–1180, 2002.

[38] M. J. Bowden and S. R. Turner, *Electronic and Photonic Applications of Polymers*, ser. Advances in Chemistry Series. American Chemical Society, Washington DC, 1988, vol. 218.

[39] W. M. Horspool and F. Lenci, *CRC Handbook of Organic Photochemistry and Photobiology*, 2nd ed. CRC Press, Boca Raton, 2004.

[40] C. A. Mack, *Fundamental Principles of Optical Lithography: The Science of Microfabrication*. Wiley, Chichester, 2007.

[41] M. Göppert-Mayer, *Ann. Phys.*, vol. 401, pp. 273–294, 1931.

[42] W. Kaiser and C. Garrett, *Phys. Rev. Lett.*, vol. 7, pp. 229–231, 1961.

[43] M. Wang, *Lithography*. Intech, 2010.

[44] J. H. Moon, J. Ford, and S. Yang, *Polym. Adv. Technol.*, vol. 17, pp. 83–93, 2006.

[45] D. Xia, Z. Ku, S. C. Lee, and S. R. J. Brueck, *Adv. Mater.*, vol. 23, pp. 147–179, 2011.

[46] A. Petritz, A. Wolfberger, A. Fian, J. R. Krenn, T. Griesser *et al.*, *Org. Electron.*, vol. 14, pp. 3070–3082, 2013.

[47] A. Facchetti, M.-H. Yoon, and T. J. Marks, *Adv. Mater.*, vol. 17, pp. 1705–1725, 2005.

[48] D. Vuillaume, C. Boulas, J. Collet, J. V. Davidovits, and F. Rondelez, *Appl. Phys. Lett.*, vol. 69, p. 1646, 1996.

[49] M. J. Panzer, C. R. Newman, and C. D. Frisbie, *Appl. Phys. Lett.*, vol. 86, p. 103503, 2005.

[50] X.-H. Zhang, B. Domercq, X. Wang, S. Yoo, T. Kondo *et al.*, *Org. Electron.*, vol. 8, pp. 718–726, 2007.

[51] M. Zirkl, A. Haase, A. Fian, H. Schön, C. Sommer *et al.*, *Adv. Mater.*, vol. 19, pp. 2241–2245, 2007.

[52] S. H. Kim, S. Y. Yang, K. Shin, H. Jeon, J. W. Lee *et al.*, *Appl. Phys. Lett.*, vol. 89, p. 183516, 2006.

[53] M. E. Roberts, N. Queraltó, S. C. B. Mannsfeld, B. N. Reinecke, W. Knoll *et al.*, *Chem. Mater.*, vol. 21, pp. 2292–2299, 2009.

[54] F. A. Yildirim, R. Meixner, R. R. Schliewe, W. Bauhofer, H. Goebel *et al.*, *MRS Proc.*, vol. 937, 2006.

[55] M. Egginger, M. Irimia-Vladu, R. Schwödiauer, A. Tanda, I. Frischauf *et al.*, *Adv. Mater.*, vol. 20, pp. 1018–1022, 2008.

[56] M. S. Sanford, J. A. Love, and R. H. Grubbs, *Organometallics*, vol. 20, pp. 5314–5318, 2001.

[57] A. Wolfberger, B. Rupp, W. Kern, T. Griesser, and C. Slugovc, *Macromol. Rapid Commun.*, pp. 518–522, 2011.

[58] T. Griesser, A. Wolfberger, U. Daschiel, V. Schmidt, A. Fian *et al.*, *Polym. Chem.*, vol. 4, p. 1708, 2013.

[59] A. Charlesby and S. H. Pinner, *P. Roy. Soc. A.-Math. Phy.*, vol. 249, pp. 367–386, 1959.

[60] T. Höfler, T. Griesser, X. Gstrein, G. Trimmel, G. Jakopic *et al.*, *Polymer*, vol. 48, pp. 1930–1939, 2007.

[61] T. Griesser, T. Höfler, S. Temmel, W. Kern, and G. Trimmel, *Chem. Mater.*, vol. 19, pp. 3011–3017, 2007.

[62] A. Petritz, A. Wolfberger, A. Fian, M. Irimia-Vladu, A. Haase *et al.*, *Appl. Phys. Lett.*, vol. 103, p. 153303, 2013.

[63] A. Wolfberger, A. Petritz, A. Fian, B. Stadlober, and T. Griesser, *Cellulose (accepted for publication).*

[64] D. Klemm, B. Heublein, H.-P. Fink, and A. Bohn, *Angew. Chem. Int. Ed.*, vol. 44, pp. 3358–3393, 2005.

[65] X. Qiu and S. Hu, *Materials*, vol. 6, pp. 738–781, 2013.

[66] D. Klemm, B. Philipp, T. Heinze, U. Heinze, and W. Wagenknecht, *Comprehensive Cellulose Chemistry.* Wiley-VCH, Weinheim, 1998, vol. 1.

[67] R. J. Moon, A. Martini, J. Nairn, J. Simonsen, and J. Youngblood, *Chem. Soc. Rev.*, vol. 40, p. 3941, 2011.

[68] D. Klemm, F. Kramer, S. Moritz, T. Lindström, M. Ankerfors *et al.*, *Angew. Chem. Int. Ed.*, vol. 50, pp. 5438–5466, 2011.

[69] R. T. Olsson, M. A. S. A. Samir, G. Salazar-Alvarez, L. Belova, V. Ström *et al.*, *Nature Nanotechnol.*, vol. 5, pp. 584–588, 2010.

[70] Y. Habibi, L. A. Lucia, and O. J. Rojas, *Chem. Rev.*, vol. 110, pp. 3479–3500, 2010.

[71] S. J. Eichhorn, A. Dufresne, M. Aranguren, N. E. Marcovich, J. R. Capadona *et al.*, *J. Mater. Sci.*, vol. 45, pp. 1–33, 2010.

[72] S. Elazzouzi-Hafraoui, Y. Nishiyama, J.-L. Putaux, L. Heux, F. Dubreuil *et al.*, *Biomacromolecules*, vol. 9, pp. 57–65, 2008.

[73] H. Jin, Y. Nishiyama, M. Wada, and S. Kuga, *Colloid. Surface. A*, vol. 240, pp. 63–67, 2004.

[74] M. Schaub, G. Wenz, G. Wegner, A. Stein, and D. Klemm, *Adv. Mater.*, vol. 5, pp. 919–922, 1993.

[75] E. Kontturi, P. Thüne, and J. Niemantsverdriet, *Polymer*, vol. 44, pp. 3621–3625, 2003.

[76] E. Kontturi, P. C. Thüne, and J. W. H. Niemantsverdriet, *Langmuir*, vol. 19, pp. 5735–5741, 2003.

[77] S. Y. Liew, W. Thielemans, and D. A. Walsh, *J. Phys. Chem. C*, vol. 114, pp. 17 926–17 933, 2010.

[78] S. Y. Liew, D. A. Walsh, and W. Thielemans, *R. Soc. Chem. Adv.*, vol. 3, p. 9158, 2013.

[79] E. D. Cranston, M. Eita, E. Johansson, J. Netrval, M. Salajková *et al.*, *Biomacromolecules*, vol. 12, pp. 961–969, 2011.

[80] E. D. Cranston and D. G. Gray, *Biomacromolecules*, vol. 7, pp. 2522–2530, 2006.

[81] Y. Fujisaki, H. Koga, Y. Nakajima, M. Nakata, H. Tsuji *et al.*, *Adv. Funct. Mater.*, vol. 24, pp. 1657–1663, 2014.

[82] E. Fortunato, N. Correia, P. Barquinha, L. Pereira, G. Goncalves *et al.*, *IEEE Electr. Device L.*, vol. 29, pp. 988–990, 2008.

[83] J. Huang, H. Zhu, Y. Chen, C. Preston, K. Rohrbach *et al.*, *ACS Nano*, vol. 7, pp. 2106–2113, 2013.

[84] E. Kontturi and A. Lankinen, *J. Am. Chem. Soc.*, vol. 132, pp. 3678–3679, 2010.

[85] L. Nyfors, M. Suchy, J. Laine, and E. Kontturi, *Biomacromolecules*, vol. 10, pp. 1276–1281, 2009.

[86] L. Taajamaa, O. J. Rojas, J. Laine, K. Yliniemi, and E. Kontturi, *Chem. Commun.*, vol. 49, p. 1318, 2013.

[87] R. Kargl, T. Mohan, S. Köstler, S. Spirk, A. Doliška *et al.*, *Adv. Funct. Mater.*, vol. 23, pp. 308–315, 2013.

[88] M. Tanaka, A. P. Wong, F. Rehfeldt, M. Tutus, and S. Kaufmann, *J. Am. Chem. Soc.*, vol. 126, pp. 3257–3260, 2004.

[89] H. Ito, M. Ueda, and W. P. England, *Macromolecules*, vol. 23, pp. 2589–2598, 1990.

[90] J. Wells C. Cunningham, "Characterization of a new organosilicon photoresist," M. J. Bowden, Ed. SPIE, 1987.

[91] J. Wells C. Cunningham, J. C. McFarland, and C.-E. Park, "Characterization of a new organosilicon photoresist," H. L. Stover and S. Wittekoek, Eds. SPIE, 1987.

[92] E. Kontturi, T. Tammelin, and M. Österberg, *Chem. Soc. Rev.*, vol. 35, p. 1287, 2006.

[93] T. Mohan, R. Kargl, A. Doliška, A. Vesel, S. Köstler *et al.*, *J. Colloid Interf. Sci.*, vol. 358, pp. 604–610, 2011.

[94] T. Mohan, T. Ristić, R. Kargl, A. Doliska, S. Köstler *et al.*, *Chem. Commun.*, vol. 49, p. 11530, 2013.

[95] H. A. Krässig, *Cellulose: Structure, Accessibility, and Reactivity*, ser. Polymer Monographs. Gordon and Breach Science, Yverdon, 1993, vol. 11.

[96] E. Reichmanis, F. M. Houlihan, O. Nalamasu, and T. X. Neenan, *Chem. Mater.*, vol. 3, pp. 394–407, 1991.

[97] H. Fan, G. Li, F. Yang, L. Yang, and S. Zhang, *J. Chem. Technol. Biot.*, vol. 86, pp. 1107–1112, 2011.

[98] S. R. Forrest, *Nature*, vol. 428, pp. 911–918, 2004.

[99] S. Logothetidis, *Mater. Sci. Eng. B-Adv.*, vol. 152, pp. 96–104, 2008.

[100] E. T. Reese, *Ind. Eng. Chem.*, vol. 49, pp. 89–93, 1957.

[101] M. Itävaara, M. Siika-aho, and L. Viikari, *J. Environ. Polym. Degr.*, vol. 7, pp. 67–73, 1999.

[102] C. Capello, U. Fischer, and K. Hungerbühler, *Green Chem.*, vol. 9, p. 927, 2007.

[103] S. Juodkazis, V. Mizeikis, K. K. Seet, M. Miwa, and H. Misawa, *Nanotechnology*, vol. 16, pp. 846–849, 2005.

[104] K.-S. Lee, R. H. Kim, D.-Y. Yang, and S. H. Park, *Prog. Polym. Sci.*, vol. 33, pp. 631–681, 2008.

[105] W. H. Teh, U. Dürig, G. Salis, R. Harbers, U. Drechsler *et al.*, *Appl. Phys. Lett.*, vol. 84, pp. 4095–4097, 2004.

[106] A. Wolfberger and T. Griesser, "Method of manufacturing an electrically conductive or semiconductive structure and electronic device comprising the same," Patent GB 1 319 263.8.

[107] A. Wolfberger, A. Petritz, A. Fian, B. Stadlober, and T. Griesser, *Publication in preparation.*

[108] V. Subramanian, J. Frechet, P. Chang, D. Huang, J. Lee *et al.*, *Proc. IEEE*, vol. 93, pp. 1330–1338, 2005.

[109] B. Geffroy, P. le Roy, and C. Prat, *Polym. Int.*, vol. 55, pp. 572–582, 2006.

[110] C. Dimitrakopoulos and P. Malenfant, *Adv. Mater.*, vol. 14, pp. 99–117, 2002.

[111] H. Klauk, *Chem. Soc. Rev.*, vol. 39, p. 2643, 2010.

[112] B. Kippelen and J.-L. Brédas, *Energy Environ. Sci.*, vol. 2, p. 251, 2009.

[113] D. S. Hecht, L. Hu, and G. Irvin, *Adv. Mater.*, vol. 23, pp. 1482–1513, 2011.

[114] C. J. Drury, C. M. J. Mutsaers, C. M. Hart, M. Matters, and D. M. de Leeuw, *Appl. Phys. Lett.*, vol. 73, p. 108, 1998.

[115] H. Sirringhaus, *Science*, vol. 290, pp. 2123–2126, 2000.

[116] D. Huang, F. Liao, S. Molesa, D. Redinger, and V. Subramanian, *J. Electrochem. Soc.*, vol. 150, p. G412, 2003.

[117] R. W. Murray, *Chem. Rev.*, vol. 108, pp. 2688–2720, 2008.

[118] M. A. Hamon, J. Chen, H. Hu, Y. Chen, M. E. Itkis *et al.*, *Adv. Mater.*, vol. 11, pp. 834–840, 1999.

[119] D. Zhang, K. Ryu, X. Liu, E. Polikarpov, J. Ly *et al.*, *Nano Lett.*, vol. 6, pp. 1880–1886, 2006.

[120] G. Eda, G. Fanchini, and M. Chhowalla, *Nature Nanotech.*, vol. 3, pp. 270–274, 2008.

[121] K. S. Subrahmanyam, S. R. C. Vivekchand, A. Govindaraj, and C. N. R. Rao, *J. Mater. Chem.*, vol. 18, p. 1517, 2008.

[122] M. J. Hostetler, J. E. Wingate, C.-J. Zhong, J. E. Harris, R. W. Vachet *et al.*, *Langmuir*, vol. 14, pp. 17–30, 1998.

[123] M.-C. Daniel and D. Astruc, *Chem. Rev.*, vol. 104, pp. 293–346, 2004.

[124] R. A. Serway, *Principles of Physics*, 2nd ed. Saunders College Pub., Fort Worth, 1998.

[125] Y. Wu, Y. Li, B. S. Ong, P. Liu, S. Gardner *et al.*, *Adv. Mater.*, vol. 17, pp. 184–187, 2005.

[126] S. H. Ko, I. Park, H. Pan, C. P. Grigoropoulos, A. P. Pisano *et al.*, *Nano Lett.*, vol. 7, pp. 1869–1877, 2007.

[127] M. R. Weinberger, S. Rentenberger, and W. Kern, *Monatsh. Chem.*, vol. 138, pp. 309–314, 2007.

[128] S. Gilles, C. Kaulen, M. Pabst, U. Simon, A. Offenhäusser *et al.*, *Nanotechnology*, vol. 22, p. 295301, 2011.

[129] A. Cerf and C. Vieu, *Colloid. Surface. A*, vol. 342, pp. 136–140, 2009.

[130] M. H. V. Werts, M. Lambert, J.-P. Bourgoin, and M. Brust, *Nano Lett.*, vol. 2, pp. 43–47, 2002.

[131] I. Park, S. H. Ko, H. Pan, C. P. Grigoropoulos, A. P. Pisano *et al.*, *Adv. Mater.*, vol. 20, pp. 489–496, 2008.

[132] S. Sun, P. Mendes, K. Critchley, S. Diegoli, M. Hanwell *et al.*, *Nano Lett.*, vol. 6, pp. 345–350, 2006.

[133] S. Huh and S. B. Kim, *J. Phys. Chem. C*, vol. 114, pp. 2880–2885, 2010.

[134] C. Subramani, X. Yu, S. S. Agasti, B. Duncan, S. Eymur *et al.*, *J. Mater. Chem.*, p. 14156, 2011.

[135] M. Brust, M. Walker, D. Bethell, D. J. Schiffrin, and R. Whyman, *J. Chem. Soc. Chem. Commun.*, p. 801, 1994.

[136] M. J. Coutts, M. B. Cortie, M. J. Ford, and A. M. McDonagh, *J. Phys. Chem. C*, vol. 113, pp. 1325–1328, 2009.

[137] Y. Wu, Y. Li, P. Liu, S. Gardner, and B. S. Ong, *Chem. Mater.*, vol. 18, pp. 4627–4632, 2006.

[138] A. Gupta, S. Mandal, M. Katiyar, and Y. N. Mohapatra, *Thin Solid Films*, vol. 520, pp. 5664–5670, 2012.

[139] W. A. MacDonald, *J. Mater. Chem.*, vol. 14, p. 4, 2004.